LHCb-ANA-2013-017
May 19, 2013
Version 5

Time integrated measurement of the semileptonic CP violating asymmetry a^s_{sl}

M. Artuso,[1,2] A. Borgia,[1] C. Hadjivasiliou,[1] S. Stone,[1,2] Z. Xing[1] L. Zhang[1] A. Webber,[3] and M. Vesterinen[2]

[1] *Syracuse University, Syracuse NY 13244, USA*
[2] *CERN, Geneva 23, Switzerland*
[3] *Manchester University*

Abstract

The CP violating asymmetry $a^s_{\rm sl}$ is studied using samples of $\overline{B}^0_s$ or B^0_s semi-muonic decays in proton-proton collisions at a centre-of-mass energy of 7 TeV with an integrated luminosity of 1 fb^{-1}. The final state studied is $D^\pm_s\mu^\mp$, with $D^\pm_s$ reconstructed in the final state $\phi\pi^\pm$. Data driven methods have been developed to measure all the efficiency ratios needed to determine $a^s_{\rm sl}$. We discuss the analysis technique, including methods to extract the signal, efficiency determination, and systematic studies. We obtain $a^s_{\rm sl}= (-0.06 \pm 0.50 \pm 0.36)\%$, where the first uncertainty is statistical and the second systematic.

Contents

1 Introduction

The goal of this study is the determination of CP asymmetry in $B_s^0\overline{B}_s^0$ mixing, which is a sensitive probe of new physics. In the neutral B system the time evolution of the two-state system describing flavor oscillation is governed by a 2x2 complex Hamiltonian matrix [1]

$$\begin{pmatrix} M_{11} - \frac{i}{2}\Gamma_{11} & M_{12} - \frac{i}{2}\Gamma_{12} \\ M_{12}^* - \frac{i}{2}\Gamma_{12}^* & M_{22} - \frac{i}{2}\Gamma_{22} \end{pmatrix}. \tag{1}$$

The mass eigenstates are linear combination of the flavor eigenstates and their eigenvalues are M_H and M_L. The mass of the flavor eigenstate is equal to diagonal elements $M_{11} = M_{22} = (M_H + M_L)/2$. Other measurable quantities are the mass difference $\Delta M = M_H - M_L$, the width difference $\Delta\Gamma = \Gamma_L - \Gamma_H$, and the semileptonic (or flavor-specific asymmetry) a_{sl}. These quantities are related to the off diagonal matrix elements as

$$\begin{aligned} \Delta M &= M_H - M_L = 2|M_{12}|\left(1 + \frac{1}{8}\frac{|\Gamma_{12}|^2}{|M_{12}|^2}\sin^2\phi_{12} + ...\right) \\ \Delta\Gamma &= \Gamma_L - \Gamma_H = 2|\Gamma_{12}|\cos\phi_{12}\left(1 - \frac{1}{8}\frac{|\Gamma_{12}|^2}{|M_{12}|^2}\sin^2\phi_{12} + ...\right) \\ a_{sl} &= \frac{|\Gamma_{12}|}{|M_{12}|}\sin\phi_{12} + \mathcal{O}\left(\frac{\Gamma_{12}}{M_{12}}\right)^2 = \frac{\Delta\Gamma}{\Delta M}\tan\phi_{12} \end{aligned} \tag{2}$$

The phase ϕ_{12} is tiny in the Standard Model (SM), $\approx 0.2^\circ$ [2].[1] New physics can enter into the phase ϕ_{12} [3, 4] and therefore affect a_{sl} . The D0 collaboration has published evidence for a decay asymmetry in semileptonic B decays of $-0.00787 \pm 0.00172 \pm 0.00093$, where the first uncertainty is statistical and the second systematic [5], which they ascribe largely to B_s^0 decays since the asymmetry in B^0 decays has been limited to be small by e^+e^- experiments operating on the $\Upsilon(4S)$ resonance [6]. This asymmetry is much larger than that predicted in the Standard Model, approximately 2×10^{-5} [1]. If true this measurement is the first demonstration of physics beyond the SM. LHCb has thus been challenged to confirm or refute it.

LHCb can perform a variety of semileptonic asymmetry measurements, in B^0 and B_s^0 decays. In principle, we have to be concerned with particle anti-particle production asymmetries, denoted as a_p as well as detector related asymmetries, a_d. In studies of time-integrated B_s^0 decays, a_p has negligible effects because of the fast $B_s^0 - \overline{B}_s^0$ oscillations. The detector asymmetry a_d requires careful treatment of several potential sources. Our goal is to measure the difference between $D_s^+ X\mu^-\overline{\nu}$ and $D_s^- X\mu^+\nu$, where the $D_s^\pm \to K^+K^-\pi^\pm$. We will first derive results considering only K pairs forming a ϕ meson, thus selecting

[1] This phase should not be confused with the one measured in $B_s^0 \to J/\psi\,\phi$ and $B_s^0 \to J/\psi\,\pi^+\pi^-$ decays, sometimes called ϕ_s.

decays where the two kaons have almost the same momentum spectrum, and thus are not affected by any detection asymmetry.

2 Formalism of the semileptonic CP asymmetry a_{sl}

This discussion is based on that by Nierste [1]. Neutral meson states are superpositions of $|M\rangle$ and $|\overline{M}\rangle$. The mass eigenstates $|M_H\rangle$ and $|M_L\rangle$ are linear combinations of $|M\rangle$ and $|\overline{M}\rangle$:

$$\begin{aligned} |M_L\rangle &= p|M\rangle + q|\overline{M}\rangle\,, \\ |M_H\rangle &= p|M\rangle - q|\overline{M}\rangle\,, \end{aligned} \tag{3}$$

with $|p|^2 + |q|^2 = 1$.

A commonly used shorthand notation for decay amplitudes is

$$A_f = A(M \to f) = \langle f|S|M\rangle, \qquad \overline{A}_f = A(\overline{M} \to f) = \langle f|S|\overline{M}\rangle. \tag{4}$$

A key quantity to study CP violation is the combination

$$\lambda_f = \frac{q}{p}\frac{\overline{A}_f}{A_f}. \tag{5}$$

λ_f encodes the essential feature of the interference of the $M \to f$ and $\overline{M} \to f$ decays, the relative phase between q/p (from meson anti-meson mixing) and $\overline{A}_f/A_f$ (stemming from the specific decay).

In addition we define a_{sl} as

$$a_{sl} = 1 - \left|\frac{q}{p}\right|^2. \tag{6}$$

The decay rates for neutral meson and anti-meson decay to the final state f are given by

$$\begin{aligned} \Gamma(M(t) \to f) &= \mathcal{N}_f\,|A_f|^2\,e^{-\Gamma t}\left\{\frac{1+|\lambda_f|^2}{2}\cosh\frac{\Delta\Gamma\, t}{2} + \frac{1-|\lambda_f|^2}{2}\cos(\Delta m\, t)\right. \\ &\qquad \left. -\mathrm{Re}\lambda_f\,\sinh\frac{\Delta\Gamma\, t}{2} - \mathrm{Im}\lambda_f\,\sin(\Delta m\, t)\right\}, \end{aligned} \tag{7}$$

$$\begin{aligned} \Gamma(\overline{M}(t) \to f) &= \mathcal{N}_f\,|A_f|^2\,\frac{1}{1-a_{sl}}\,e^{-\Gamma t}\left\{\frac{1+|\lambda_f|^2}{2}\cosh\frac{\Delta\Gamma\, t}{2} - \frac{1-|\lambda_f|^2}{2}\cos(\Delta m\, t)\right. \\ &\qquad \left. -\mathrm{Re}\lambda_f\,\sinh\frac{\Delta\Gamma\, t}{2} + \mathrm{Im}\lambda_f\,\sin(\Delta m\, t)\right\}. \end{aligned} \tag{8}$$

where $\mathcal{N}_f$ is a time-independent normalization factor.

Often we want to compare these decay modes with the corresponding decays into the final state which is CP-conjugate with respect to f. The $M(t) \to \overline{f}$ decay rates are

$$\begin{aligned}\Gamma(M(t) \to \overline{f}) &= \mathcal{N}_f \left|\overline{A}_{\overline{f}}\right|^2 e^{-\Gamma t} (1 - a_{sl}) \left\{ \frac{1 + |\lambda_{\overline{f}}|^{-2}}{2} \cosh\frac{\Delta\Gamma\, t}{2} - \frac{1 - |\lambda_{\overline{f}}|^{-2}}{2} \cos(\Delta m\, t) \right. \\ &\qquad \left. -\mathrm{Re}\frac{1}{\lambda_{\overline{f}}} \sinh\frac{\Delta\Gamma\, t}{2} + \mathrm{Im}\frac{1}{\lambda_{\overline{f}}} \sin(\Delta m\, t) \right\}, \qquad (9)\\ \Gamma(\overline{M}(t) \to \overline{f}) &= \mathcal{N}_f \left|\overline{A}_{\overline{f}}\right|^2 e^{-\Gamma t} \left\{ \frac{1 + |\lambda_{\overline{f}}|^{-2}}{2} \cosh\frac{\Delta\Gamma\, t}{2} + \frac{1 - |\lambda_{\overline{f}}|^{-2}}{2} \cos(\Delta m\, t) \right. \\ &\qquad \left. -\mathrm{Re}\frac{1}{\lambda_{\overline{f}}} \sinh\frac{\Delta\Gamma\, t}{2} - \mathrm{Im}\frac{1}{\lambda_{\overline{f}}} \sin(\Delta m\, t) \right\}. \qquad (10)\end{aligned}$$

The time dependence of a flavour-specific decay satisfies $\overline{A}_f = A_{\overline{f}} = \lambda_f = 1/\lambda_{\overline{f}} = 0$. In addition, we can consider decay modes with $|\overline{A}_{\overline{f}}| = |A_f|$, that is without direct CP violation. Semileptonic decays satisfy both conditions. The *CP asymmetry in flavour-specific decays* (often called the *semileptonic CP asymmetry*) is given by

$$\frac{\Gamma(\overline{M}(t) \to f) - \Gamma(M(t) \to \overline{f})}{\Gamma(\overline{M}(t) \to f) + \Gamma(M(t) \to \overline{f})} = \frac{1 - (1 - a_{sl})^2}{1 + (1 - a_{sl})^2} = a_{sl} + \mathcal{O}(a_{sl}^2). \qquad (11)$$

This measurement requires flavor tagging.

Here we use untagged decays. Defining the untagged decay rate as

$$\Gamma[f, t] = \Gamma(\overline{M}(t) \to f) + \Gamma(M(t) \to f), \qquad (12)$$

we find:

$$\frac{\Gamma[f, t] - \Gamma[\overline{f}, t]}{\Gamma[f, t] + \Gamma[\overline{f}, t]} = \frac{a_{sl}}{2} - \frac{a_{sl}}{2} \frac{\cos(\Delta m\, t)}{\cosh(\Delta\Gamma t/2)}. \qquad (13)$$

3 Including the production asymmetry

The above equations are only valid if we start out with equal production of B_s^0, labeled N, and $\overline{B}_s^0$, labeled $\overline{N}$. Let us now re-derive Eq. 13 allowing for $N \neq \overline{N}$. We have

$$\begin{aligned}\Gamma(M(t) \to f) &= N\, |A_f|^2\, e^{-\Gamma t} \left\{ \frac{1}{2} \cosh\frac{\Delta\Gamma\, t}{2} + \frac{1}{2} \cos(\Delta m\, t) \right\} \\ \Gamma(\overline{M}(t) \to f) &= \overline{N}\, |A_f|^2\, \frac{1}{1 - a_{sl}}\, e^{-\Gamma t} \left\{ \frac{1}{2} \cosh\frac{\Delta\Gamma\, t}{2} - \frac{1}{2} \cos(\Delta m\, t) \right\}. \qquad (14)\end{aligned}$$

Summing we have

$$\begin{aligned}\Gamma[\overline{f},t] &\equiv \Gamma(M(t)\to f)+\Gamma(\overline{M}(t)\to f)\\ &= \frac{|A_f|^2}{2}\left\{\left(N+\frac{\overline{N}}{1-a_{sl}}\right)\cosh\frac{\Delta\Gamma\, t}{2}+\left(N-\frac{\overline{N}}{1-a_{sl}}\right)\cos(\Delta m\, t)\right\}. \quad (15)\end{aligned}$$

Similarly

$$\begin{aligned}\Gamma(M(t)\to\overline{f}) &= N\,|A_f|^2\,(1-a_{sl})e^{-\Gamma t}\left\{\frac{1}{2}\cosh\frac{\Delta\Gamma\, t}{2}+\frac{1}{2}\cos(\Delta m\, t)\right\}\\ \Gamma(\overline{M}(t)\to\overline{f}) &= \overline{N}\,|A_f|^2\,e^{-\Gamma t}\left\{\frac{1}{2}\cosh\frac{\Delta\Gamma\, t}{2}-\frac{1}{2}\cos(\Delta m\, t)\right\} \quad (16)\end{aligned}$$

and the sum is given by

$$\begin{aligned}\Gamma[f,t] &\equiv \Gamma(M(t)\to\overline{f})+\Gamma(\overline{M}(t)\to\overline{f})\\ &= \frac{|A_f|^2}{2}\left\{\big(N(1-a_{sl})+\overline{N}\big)\cosh\frac{\Delta\Gamma\, t}{2}+\big(N(1-a_{sl}-\overline{N}\big)\cos(\Delta m\, t)\right\}. \quad (17)\end{aligned}$$

The production asymmetry, a_p, is defined as

$$a_p=\frac{N-\overline{N}}{N+\overline{N}}\ . \quad (18)$$

To first order in a_{sl} we have

$$\frac{\Gamma[f,t]-\Gamma[\overline{f},t]}{\Gamma[f,t]+\Gamma[\overline{f},t]}=\frac{a_{sl}}{2}+\left[a_p-\frac{a_{sl}}{2}\right]\frac{e^{-\Gamma t}\cos(\Delta m\, t)\epsilon(t)}{e^{-\Gamma t}\cosh\frac{\Delta\Gamma\, t}{2}\epsilon(t)}, \quad (19)$$

where $\epsilon(t)$ is the time-dependent acceptance function.

For a time-independent measurement we integrate the equations involving N and $\overline{N}$ over time finding [7]

$$\frac{\Gamma[f]-\Gamma[\overline{f}]}{\Gamma[f]+\Gamma[\overline{f}]}=\frac{\Gamma[D_s^-\mu^+]-\Gamma[D_s^+\mu^-]}{\Gamma[D_s^-\mu^+]+\Gamma[D_s^+\mu^-]}=\frac{a_{sl}}{2}+\left[a_p-\frac{a_{sl}}{2}\right]\frac{\int_{t=0}^{\infty}e^{-\Gamma t}\cos(\Delta m\, t)\epsilon(t)dt}{\int_{t=0}^{\infty}e^{-\Gamma t}\cosh\frac{\Delta\Gamma\, t}{2}\epsilon(t)dt}, \quad (20)$$

The decay time acceptance function for $B_s^0\to D_s^+X\mu^-\overline{\nu}$ is determined by Monte Carlo simulation. It is given by

$$\epsilon(t)=\frac{[1+\beta(t-t_0)][a(t-t_0)]^n}{1+[a(t-t_0)]^n}, \quad (21)$$

where $a=1.382$, $n=1.771$, $t_0=0.07742$ and $\beta=-0.0494$ for B_s^0 decays. The acceptance function is shown in Fig. 1.

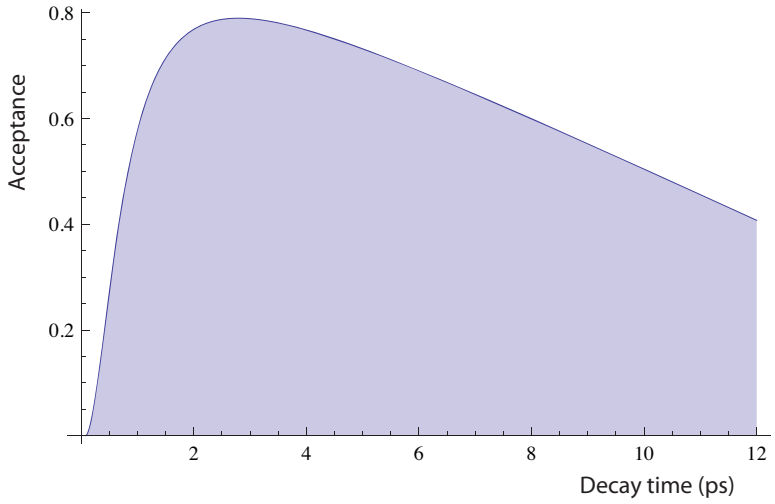

Figure 1: Decay time acceptance function $\epsilon(t)$.

We have evaluated the integral ratio in Eq. 20 for the case of $D_s^+ X\mu^-\overline{\nu}$ decays, and find 0.2% for B_s decays. A similar calculation for B^0 decays gives 46%. Since the production asymmetry is expected to at most a few percent [8, 9], this reduces the effect on a_p to the level of about 10^{-4} for B_s decays, well under our goal of an error on the order of 10^{-3}. For B^0 decays, however, the contribution from the production asymmetry can still be significant at the level of about 0.5%.

4 Analysis Method

Our goal is to measure the difference between $D_s^+ X\mu^-\overline{\nu}$ and $D_s^- X\mu^+\nu$, where the $D_s^\pm \to K^+K^-\pi^\pm$. In the first measurement we restrict ourselves to D_s^+ decaying into $\phi\pi^+$, in order to suppress D_s^+ background, and also to ensure that the K^+K^- momentum spectra difference has negligible effects on the systematic uncertainty. Actually, this kinematic asymmetry is not a large effect even if we consider the entire $K^+K^-\pi^+$ final state. In the following discussion, whenever we reference D_s^+ or $D_s^+\mu^-$ charge conjugation is implied.

4.1 Data sample

We use Reco12 Stripping17 2011 dataset ($\int \mathcal{L} = 1\,\text{fb}^{-1}$, listed in Table 1) and the official MC11a simulation, both processed using DaVinci v29r2(3). We require the muon in the semileptonic candidate to satisfy the L0 muon trigger requirements (L0 TOS). Similarly, we require it to be selected by at least one of the TrackAll, TrackMuon, or SingleMuonHighPT HLT1 algorithms. Finally, we accept candidates for which the muon satisfies any of the muon topological HLT2 trigger [10] or the candidate ϕ is selected by the HLT2 inclusive ϕ algorithm. We have studied also two mutually exclusive samples triggered either by the inclusive ϕ algorithm or by the muon topological HLT2 trigger excluding

events selected by the inclusive ϕ algorithm and found consistent results. The data sets taken with magnet polarity up and down are analyzed separately. Furthermore, we study individual subsets separated by a magnet polarity flip to assess time dependent effects upon the efficiency ratios.

Table 1: List of 2011 data samples used in this analysis

Stripping	Online Lumi(pb^{-1}) Magnet Up	Magnet Down
$Semileptonic/Strippingb2DsMuXPhiPi$	447	595
$Semileptonic/Strippingb2DsMuX$	447	595
$PID/MuIDCalib\_JpsiFromBNoPIDNoMip$	447	595
$CharmCompleteEvent/StrippingD0ForBXX$	447	595

We use several Monte Carlo (MC) samples developed specifically for this analysis, incorporating all our present knowledge on B semileptonic decays. These samples are listed in Table 2.

Table 2: List of MC samples used in this analysis

Event type	Physics Channel	Event Number
13774002	$B_s^0 \to D_s^- \mu^+ \nu_\mu X$	20M
13873201	$B_s^0 \to D_s^- D_s^+$	5M
12775001	$B^+ \to D_s^+ K \mu^- \nu_\mu$	5M
11774001	$B^0 \to D_s^+ K \mu^- \nu_\mu$	5M
12875601	$B^+ \to D^0 D_s^+ \mu^- \nu_\mu$	5M
11876001	$B^0 \to D^0$ or $D^- D_s^+$	5M
15894301	$\Lambda_b \to D_s^- \Lambda_c^+ X$	10 M

4.2 Stripping and Offline Selection criteria

Candidate events are filtered with a dedicated stripping line with the criteria summarized in Table 3, and are analyzed with the most stringent selection described in Table 4. The cuts are largely based on our previous studies of B_s^0 semileptonic decays [11].

Table 3: Stripping cuts on the B_s^0 signal

Item	Requirement
Muon selections	
	$p > 3\,\text{GeV}$; $p_\text{T} > 0.8\,\text{GeV}$
	IP $\chi^2 > 4$; isMuon
	Track $\chi^2/\text{NDF} < 5$; PIDMu> 0
D_s^+ daughter hadrons	
	$p > 2\,\text{GeV}$; $p_\text{T} > 300\,\text{MeV}$
	IP $\chi^2 > 4$; Kaon PIDK> -5
	Track $\chi^2/\text{NDF} < 4$
ϕ meson	
	m(K^+K^-) within 50 MeV of ϕ invariant mass
	Vertex fit $\chi^2/\text{NDF} < 25$
D_s^+ meson	
	m(D_s) within 200 MeV of D_s invariant mass
	$p(\phi\pi) > 800\,\text{MeV}$
	Vertex fit $\chi^2/\text{NDF} < 6$; $DIRA > 0.99$
	FD $\chi^2 > 100$; sum of IP $\chi^2 > 4$
$B_s^0(D_s^+\mu)$	
	$2.5\,\text{GeV} <$ m$(D_s^+\mu) < 6\,\text{GeV}$
	Vertex fit $\chi^2/\text{NDF} < 6$
	$DIRA > 0.999$; $z(D_s^+) - z(B_s^0) > 0$

Table 4: Offline selections on the B_s^0 signal. In addition, the "CLONEKILLER" filter is applied to all the tracks in the candidate B_s^0, cuts within square brackets are common to the stripping code selection criteria.

Muon selection criteria	
p	$> 6\,\text{GeV}$ and $< 100\,\text{GeV}$
p_{T}	$> 1.5\,\text{GeV}$
IP χ^2	> 4
muon identification	IsMuon=1&nShare= 0 & PIDmu> 0
Track χ^2/NDF	< 3
η	[2,5]
D_s^+ daughter hadrons	
Kaon identification	PIDK> 4
p	$> 2\,\text{GeV}$
p_{T}	$> 0.3\,\text{GeV}$
sum of p_{T}	$> 2.1\,\text{GeV}$
IP χ^2	> 9
	Track χ^2/NDF < 4
ϕ meson	
$\lvert m(K^+K^-) - m(\phi)\rvert$	≤ 20 MeV
D_s^+ meson selection criteria	
Vertex fit	χ^2/NDF < 6
$DIRA$	> 0.99
FD χ^2	> 100
IP	$< 7.4\,\text{mm}$
$B_s^0(D_s^+\mu)$ selection criteria	
Vertex fit	χ^2/NDF < 6
$DIRA$	> 0.999
$z(D_s^+) - z(B_s^0)$	> 0
η	[2,5]
$m(B_s^0)$	$[3.1,5.1]\,\text{GeV}$
global event cut	n(longTracks)< 250

4.3 The measured semileptonic asymmetry

We construct the asymmetry

$$A_{\rm meas} \equiv \frac{\Gamma(\overset{(-)}{B}_s \to D_s^- \mu^+ \nu_\mu) - \Gamma(\overset{(-)}{B}_s \to D_s^+ \mu^- \overline{\nu}_\mu)}{\Gamma(\overset{(-)}{B}_s \to D_s^- \mu^+ \nu_\mu) + \Gamma(\overset{(-)}{B}_s \to D_s^+ \mu^- \overline{\nu}_\mu)} = A_\mu^{\rm c} - A_{\rm track} - A_{\rm bkg}, \qquad (22)$$

where $A_\mu^{\rm c}$ is given by

$$A_\mu^{\rm c} = \frac{N(D_s^- \mu^+) - N(D_s^+ \mu^-) \times \frac{\epsilon(\mu^+)}{\epsilon(\mu^-)}}{N(D_s^- \mu^+) + N(D_s^+ \mu^-) \times \frac{\epsilon(\mu^+)}{\epsilon(\mu^-)}}, \qquad (23)$$

where $N(D_s^- \mu^+)$ and $N(D_s^+ \mu^-)$ are measured yields of $D_s \mu$ pairs, and $\epsilon(\mu^+)$ and $\epsilon(\mu^-)$ are the efficiency corrections including trigger and muon identification effects. As the D_s^+ production asymmetry term is highly suppressed in Eq. 20, $A_{\rm meas}$=0.5 $a_{\rm sl}^s$.

The detection asymmetry is largely induced by the dipole magnet, which bends particles of different charge in different detector halves (the so called A and C sides of LHCb). The magnet polarity is reversed periodically, thus allowing the measurement and understanding of the size of this effect. We analyze data taken with different magnet polarities separately, deriving charge asymmetry corrections for the two data sets independently. Finally, we average the two values in order to cancel any residual effects. This analysis relies on well identified muons for background suppression, thus the understanding of muon detection asymmetries is crucial. Such asymmetries may be introduced by the muon identification efficiency algorithm, as well as by L0, HLT1, and HLT2 triggers requiring the presence of a muon in the selected event. In order to ascertain these detection asymmetries, we have used an inclusive J/ψ sample, comprising events containing two charged tracks with an invariant mass consistent with the J/ψ mass, that is triggered independently of the J/ψ $\mu^+\mu^-$ tracks (TIS), mostly by hadronic B candidates. Its advantages are the reliance on purely kinematic selection criteria and the fact that the full DST information is available to us. This sample will be referred to as the kinematically selected (KS) calibration sample. In addition, we consider the J/ψ calibration sample used in other muon efficiency studies [12], and derive the relevant efficiencies with the so called "tag and probe" method, where one muon candidate (tag) is selected with stringent muon identification criteria, while the other muon (probe) is selected kinematically, by requiring it to form an invariant mass with the tag consistent with the known J/ψ mass. This sample will be referred to as the muon selected (MS) calibration sample.

The correction factor $A_{\rm track}$ in Eq. 22 accounts for detection asymmetries between particles with positive or negative charge. Let us first consider the pion case. Differences can arise due to the different interaction cross-sections in the detector material or to differences between tracking negative and positive particles. We have developed a tool based on partial reconstruction that has been used to measure the production asymmetry in D_s^+ versus D_s^- decays [13]. More details can be found in the $D_s^+ - D_s^-$ production asymmetry analysis note [14]. We found that the relative tracking efficiencies of π^+ versus π^- are independent of momentum p and transverse momentum $p_{\rm T}$. This, along

with the fact that π^+ and π^- interaction cross sections on isoscalar targets are equal, implies that the difference between π^+ and π^- tracking efficiencies depend only upon the magnetic field orientation and thus detector acceptance. In the $\phi\pi^+\mu^-$ final states, the pion and muon have opposite sign, and thus a possible residual charge asymmetry in the tracking reconstruction efficiency cancels. Similar considerations apply to the K^+ and K^- tracking efficiency.

Finally, the term $A_{\rm bkg}$ reflects possible asymmetries introduced by background events. These include backgrounds from prompt charm decays, events in which the D_s^+ is produced in a hadronic B_s^0 decay, where one of the hadrons produced in concomitance with the D_s^+ is misidentified as a muon, or physics backgrounds associated with other b-hadrons that are decaying into a $D_s^-\mu^+$ pair. Both terms have been accounted for and are found to be small.

4.4 Dipole magnet and acceptance effects

The dipole magnet produces a transverse momentum "kick" Δp_x in the LHCb x direction (orthogonal to the magnetic field direction and the beam axis) with opposite sign for positive and negative charges. This distorts the charged particle distribution in the downstream tracking planes, and shifts its centroid either towards the A or C half planes [15]. This distortion affects the asymmetry in two different ways. The acceptance boundaries, near the beam pipe and at the outer edge of the tracking stations and muon chambers, affect one charge state more than the other, as they are swept either in or out of the acceptance. As a result, there are regions in the detector where there is maximum charge asymmetry. These regions can be largely removed by applying fiducial cuts such as

$$\begin{aligned} |p_X| \ &| \leq \ 0.317 \times (p_z - p_0) \\ p_0(\pi) \ &= \ 2400\text{MeV} \\ p_0(\mu) \ &= \ 3100\text{MeV} \end{aligned} \tag{24}$$

complemented, for pions at low angle with respect to the z axis ($|p_y/p_z| < 0.02$), by the requirements

$$\begin{aligned} p_1 - \beta_1 p_z < |p_x| < p_2 + \beta_2 p_z \\ p_1 = 418\text{MeV} \\ p_2 = 497\text{MeV} \\ \beta_1 = 0.01397 \\ \beta_2 = 0.01605 \end{aligned} \tag{25}$$

With these cuts, we loose 9% of the signal, with a change in the central value of the raw asymmetry A_{raw} by 0.01%. We do not apply fiducial cuts to remove these regions, as they affect a very small fraction of the phase space of the signal events.

A given charge state will be detected preferentially in the A side or the C side depending upon the magnet polarity. Thus any difference in efficiency between the two LHCb detector halves will be reflected in the detection efficiency ratios. As the momentum of the B_s^0 decay products increases, they are focused more and more in the innermost detection planes, and thus the effect of the acceptance near the beam pipe becomes more important. This effect is illustrated in Figs. 2-6, which shows the signal muon projection on the M3 muon chamber plane. The structure seen (acceptance holes) is present also in the calibration sample and corresponds to region where the overlap between chambers is not perfect. For example, at x$\sim$ 2700 mm the overlap between chambers three and four is partial. Thus we split our samples into 5 muon momentum intervals, $6-20\,\mathrm{GeV}$, $20-30\,\mathrm{GeV}$, $30-40\,\mathrm{GeV}$, $40-50\,\mathrm{GeV}$ and $50-100\,\mathrm{GeV}$. One can see that the geometrical acceptance for positive muons is essentially the mirror image of the one for negative muons with respect to the $\vec{B}$ axis. As this is the dominant effect in producing the detection asymmetry, we study the muon kinematics using the variable $q \times p_x$.

We are using calibration samples that do not match the kinematic properties of the signal perfectly. Thus we further subdivide the signal and calibration sample in smaller samples with two choices: in the first method each μ momentum bin is split into 10 rectangular regions in $q \times p_x, p_y$, the latter uses 8 regions split in p_T, ϕ. In this case the first and third bins in ϕ are flipped for negative charges, to symmetrize the acceptance in a consistent manner with the $q \times p_x, p_y$ binning. We then evaluate a^s_{sl} in each bin and we derive our final result as a weighted average of these independent measurements. By comparing our results with two different sets of kinematic domains we ascertain biases induced by a particular kinematic binning. The two different sets of binning are shown in Fig. 7.

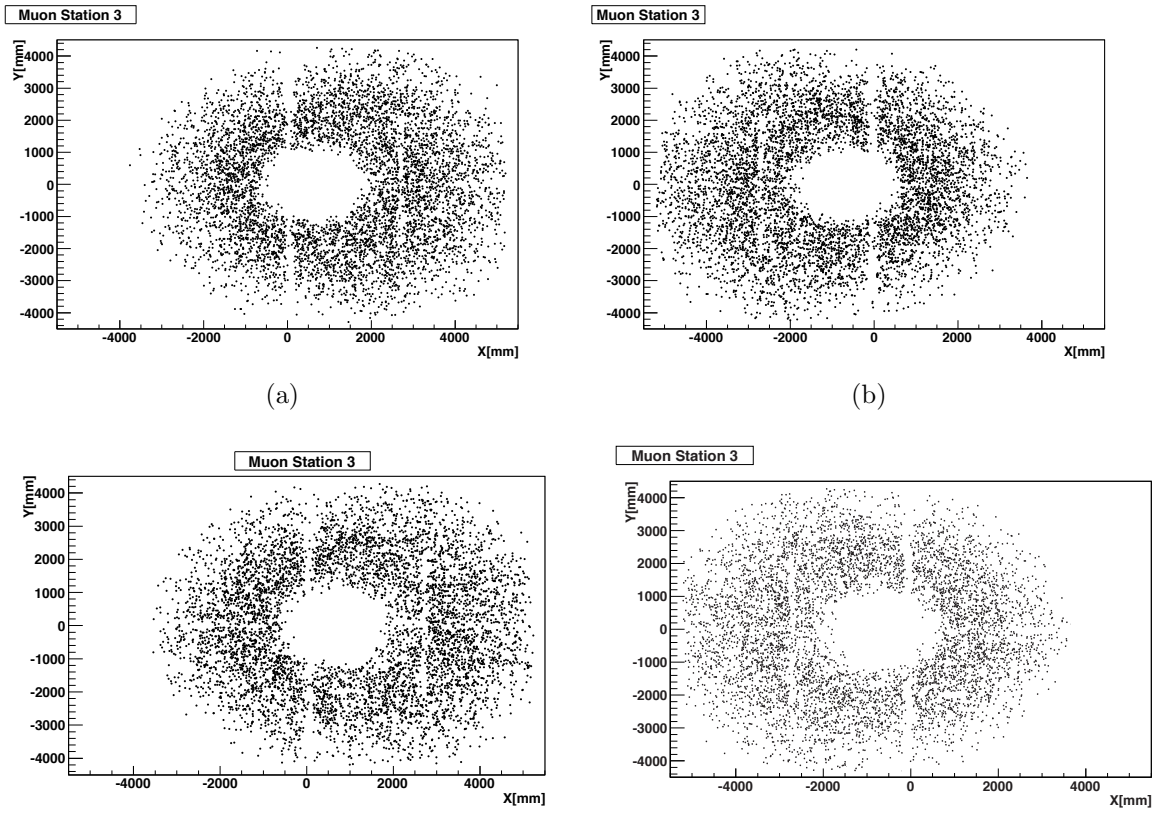

Figure 2: Two-dimensional projection of the signal sample on the muon chamber plane M3 for muons with momentum $6\,\mathrm{GeV} \leq p < 20\,\mathrm{GeV}$: a) μ^+ and magnet polarity DOWN, b) μ^- and magnet polarity DOWN, c) μ^- and magnet polarity UP, d) μ^+ and magnet polarity UP.

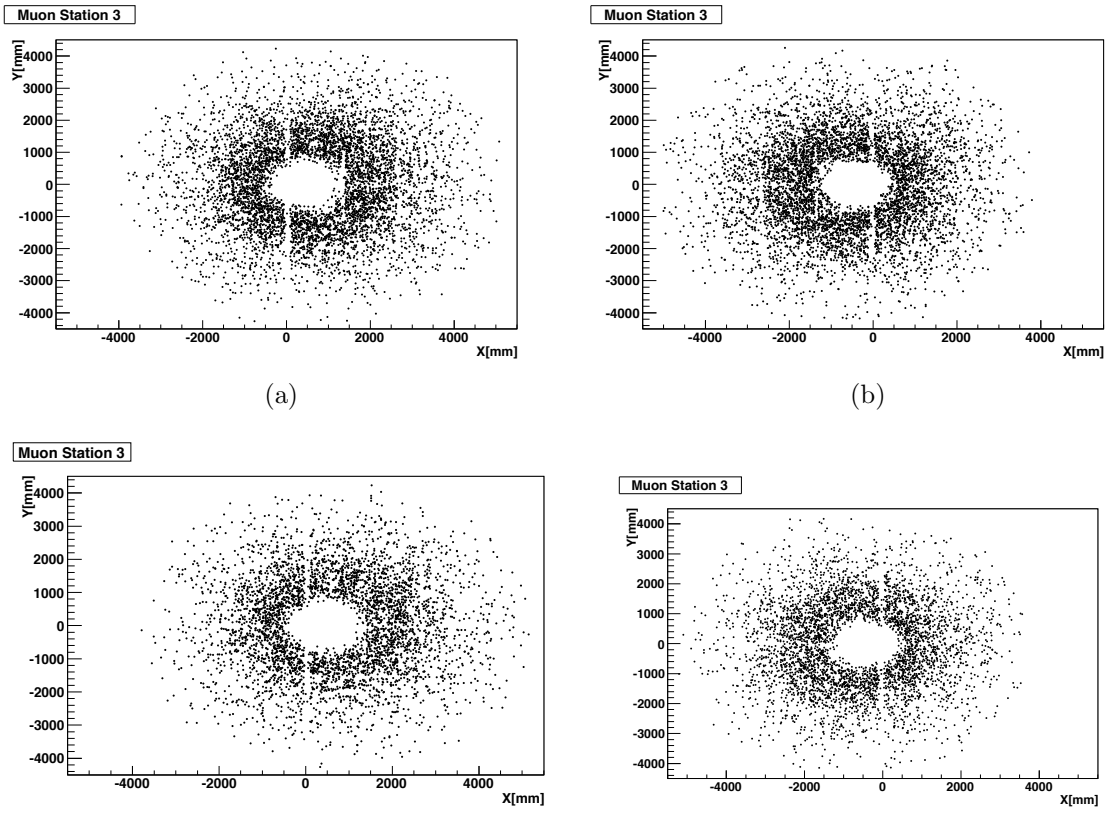

Figure 3: Two-dimensional projection of the signal sample on the muon chamber plane M3 for muons with momentum $20\,\text{GeV} \leq p < 30\,\text{GeV}$: a) μ^+ and magnet polarity DOWN, b) μ^- and magnet polarity DOWN, c) μ^- and magnet polarity UP, d) μ^+ and magnet polarity UP.

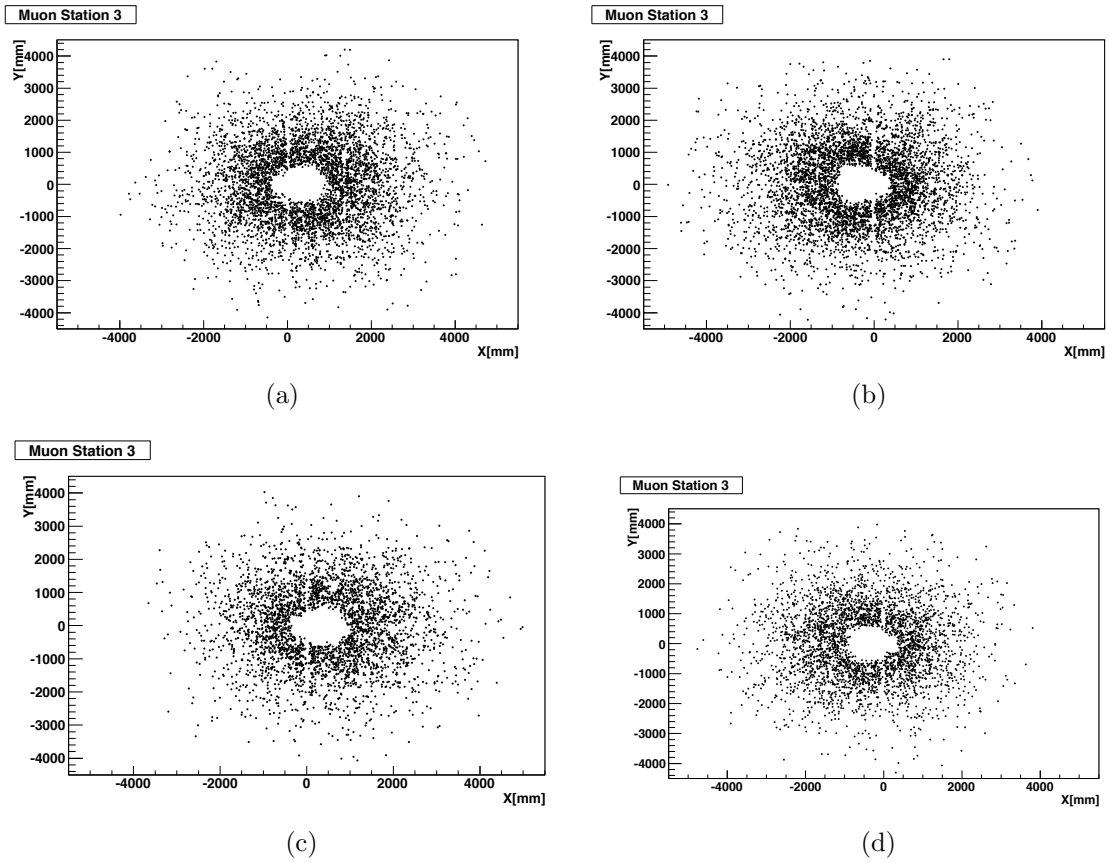

Figure 4: Two-dimensional projection of the signal sample on the muon chamber plane M3 for muons with momentum $30\,\text{GeV} \leq p < 40\,\text{GeV}$: a) μ^+ and magnet polarity DOWN, b) μ^- and magnet polarity DOWN, c) μ^- and magnet polarity UP, d) μ^+ and magnet polarity UP.

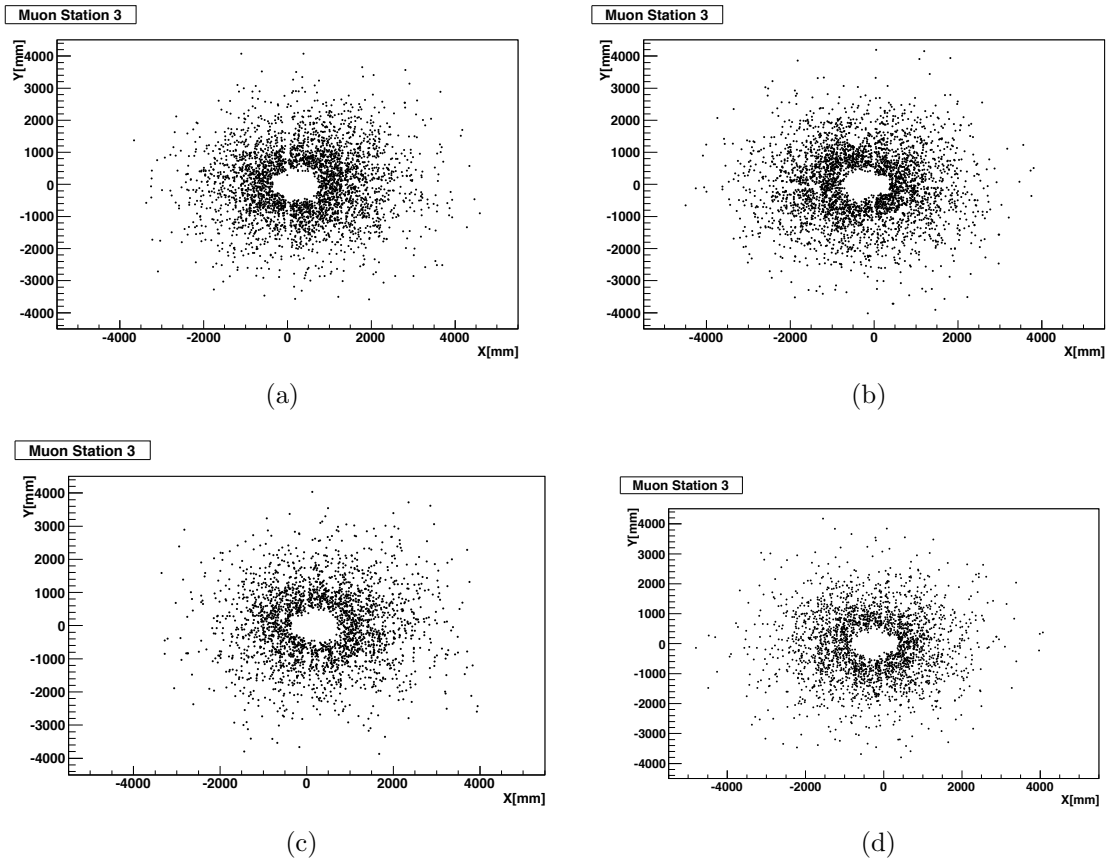

Figure 5: Two-dimensional projection of the signal sample on the muon chamber plane M3 for muons with momentum $40\,\text{GeV} \leq p < 50\,\text{GeV}$: a) μ^+ and magnet polarity DOWN, b) μ^- and magnet polarity DOWN, c) μ^- and magnet polarity UP, d) μ^+ and magnet polarity UP.

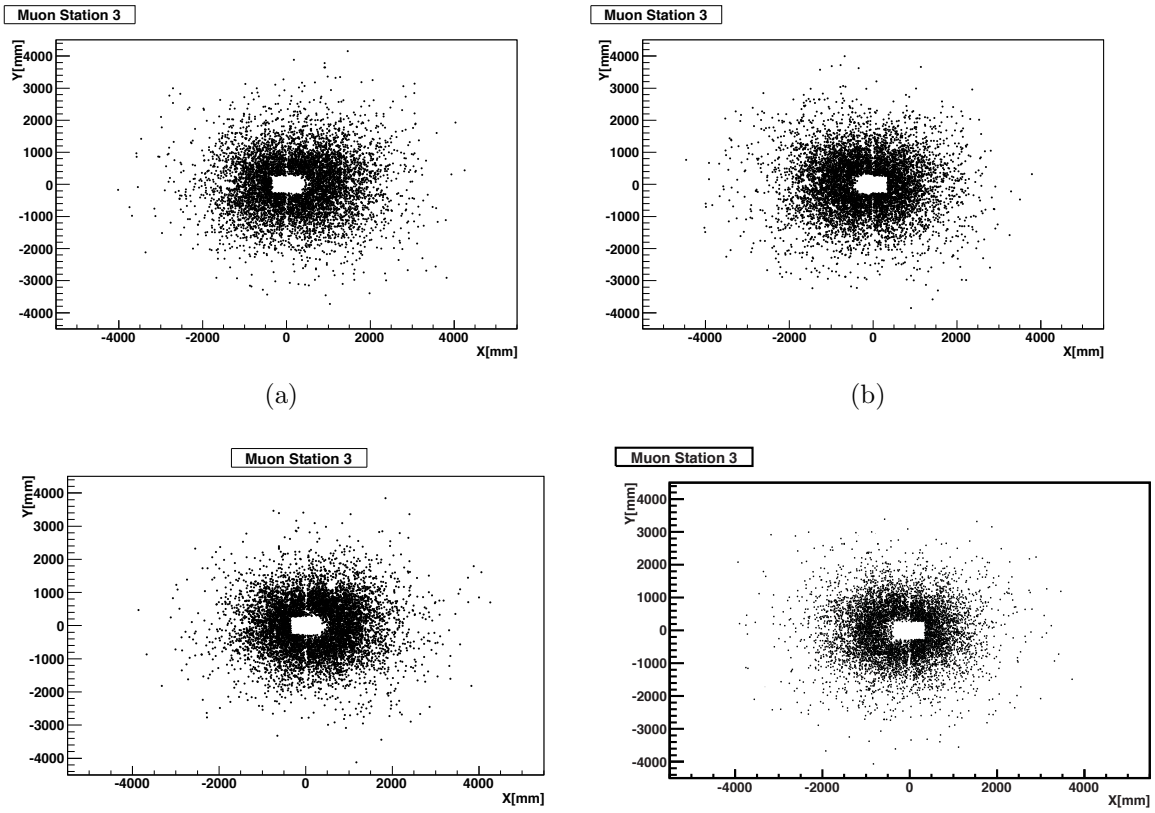

Figure 6: Two-dimensional projection of the signal sample on the muon chamber plane M3 for muons with momentum $50\,\text{GeV} \leq p < 100\,\text{GeV}$: a) μ^+ and magnet polarity DOWN, b) μ^- and magnet polarity DOWN, c) μ^- and magnet polarity UP, d) μ^+ and magnet polarity UP.

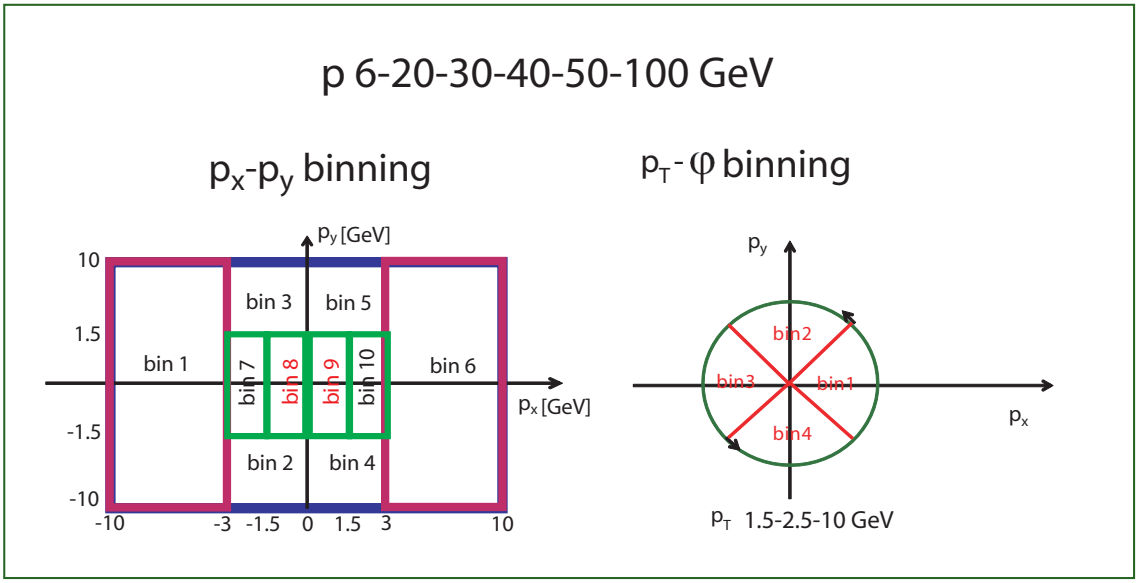

Figure 7: Definition of kinematic binning for: p_x and p_y; and φ angle, where $\varphi = \tan^{-1}(p_y/p_x)$

5 Signal Extraction

$D_s\mu$ pairs coming from B_s decays, identified as "Dfb" constitute the signal. Most charm hadrons are produced directly via $pp \to c\bar{c}X$ interactions, where the X indicates the sum over all other possible final state particles. We denote these particular charm decays as "prompt". The "prompt" background is highly suppressed by the requirement of a well identified muon forming a good vertex with the candidate D_s^+. The residual prompt background can be measured by examining the impact parameter (IP) with respect to the primary vertex, where IP is defined as the smallest distance between the D_s direction and primary vertex position. In addition, there is a D_s combinatoric background. This component is constrained by using a mass window sufficiently wide to encompass regions where the signal has negligible yields. The signal is isolated from prompt and false D_s backgrounds using a binned two dimensional fit to the mass and ln(IP/mm) of the candidate combinations of $\phi\pi^{\mp}$, where the $\phi\pi^-$ and the $\phi\pi^+$ are fitted simultaneously. In order to optimize the precision with which the fit can determine the signal and background yields, the PDF shapes for the prompt and Dfb ln(IP/mm) PDF shapes are constrained using control samples. The prompt shape is derived from a special stripped sample comprising a D_s and a charged hadron satisfying the kinematic constraints used in selecting the signal sample. The wrong sign (WS) decays, defined as π from the D_s and μ combinations having the same sign, are also fitted, and have yields at the level of 1% or below. As an example of this procedure, Fig. 8 the results of a two-dimensional fit to the magnet up $D_s^+\mu^-$ candidate sample, while Fig. 9 shows the corresponding fits for the magnet down sample. The D_s^+ background is also fitted with bifurcated Gaussian with all shape parameters floating. For the mass fit, both Dfb and prompt D_s^+ are fitted as a single component with a double Gaussian function with a common mean. The background is then modeled by a second order polynomial function. The prompt background is of the order of 1% of the total number of D_s^+ $(1.8 \pm 0.2)\%$ in the first momentum bin, $(1.4 \pm 0.1)\%$ in the second, and $(1.1 \pm 0.1)\%$ in the last three bins. Since the measured production asymmetry of $D_s^+ - D_s^-$ is $(-0.33 \pm 0.22 \pm 0.10)\%$ [16], the total effect on $a_{\rm sl}^s$ is of the order of 3×10^{-5}, and is negligible. Thus we determine the signal yields only by fitting the $K^+K^-\pi^{\pm}$ invariant mass distributions.

The signal PDF of $D_s^{\pm}$ is defined as:

$$f(m) = f \times Gauss(\mu_1, \sigma_1, m) + (1 - f) \times Gauss(\mu_2, \sigma_2, m) \ , \tag{26}$$

where m indicates the observable, invariant mass $m(KK\pi)$, and $Gauss(\mu, \sigma, m)$ is the Gaussian function of m with mean as μ and width as σ. We show the results for the overall $K^+K^-\pi^+$ mass spectra for the magnet up and the magnet down samples. We fit both the signal D_s^+ (yellow shaded area) and D^+ (red shaded area) with double Gaussian functions with a common mean. The background is modeled with a second order Chebychev polynomial. Fits with linear background shape have been performed as well. Fig. 10 shows the invariant mass for the $K^+K^-\pi^+$ and $K^+K^-\pi^-$ candidates for magnet up data, and Fig. 11 the corresponding spectra for magnet down data. Table 5 summarizes the corresponding fit parameters. The signal yields from the fits are listed in Table 6. As a

check the event yields are determined by counting the yields in the range indicated by the vertical red-dashed lines above the background level, which was determined in the fits discussed above. The signal yields are large and consistent using the two methods. The fit parameters for the $D_s^{\pm}$ signal component are shown in Table 5, the average mass resolution is about 7.1 MeV.

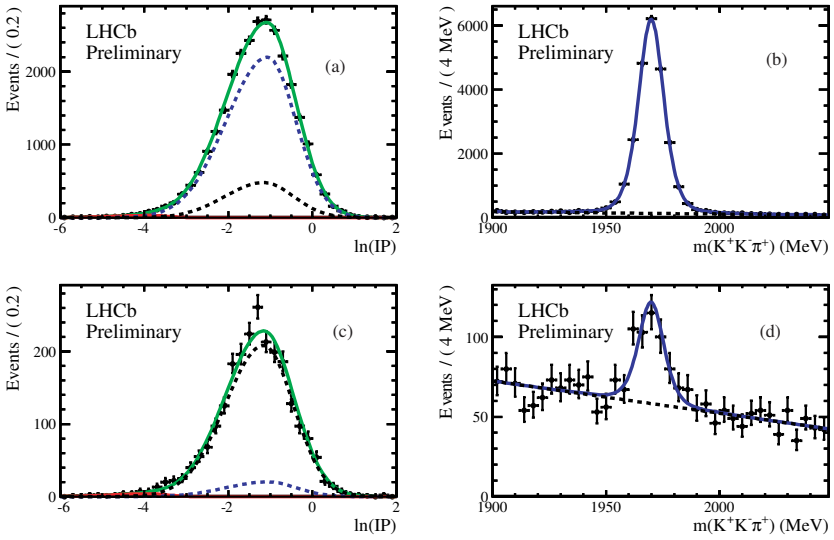

Figure 8: The logarithm of the IP distributions and invariant mass distributions for $K^+K^-\pi^+$ events in magnet up data with m(K^+K^-) within 20 MeV of ϕ meson mass. (a) and (b) show RS, while (c) and (d) show WS. The fitting functions are described in the text. The small solid (red) curves near ln(IP) equal to -4 in (a) and (c) show the prompt component, the dotted (blue) curves show the signal from B decays, the dashed (black) curves show the total yield.

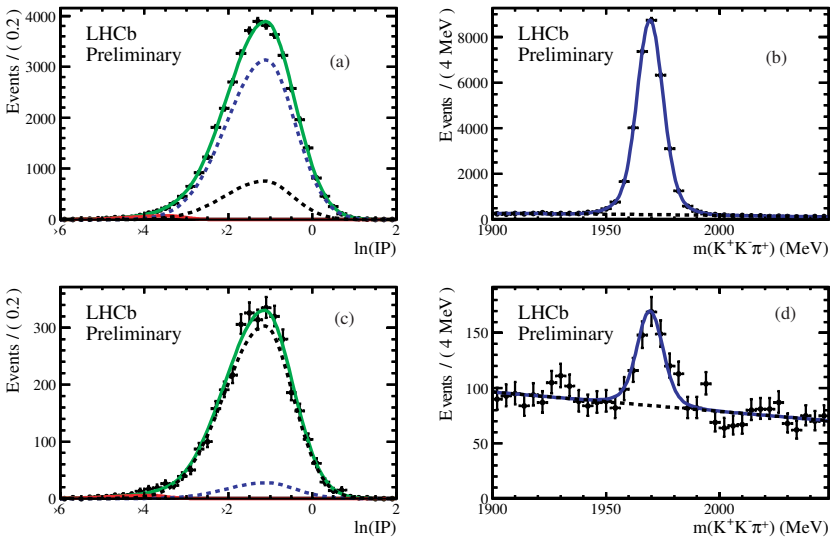

Figure 9: The logarithm of the IP distributions and invariant mass distributions for $K^+K^-\pi^+$ events in magnet down data with m(K^+K^-) within 20 MeV of ϕ meson mass. (a) and (b) show RS, while (c) and (d) show WS. The fitting functions are described in the text.

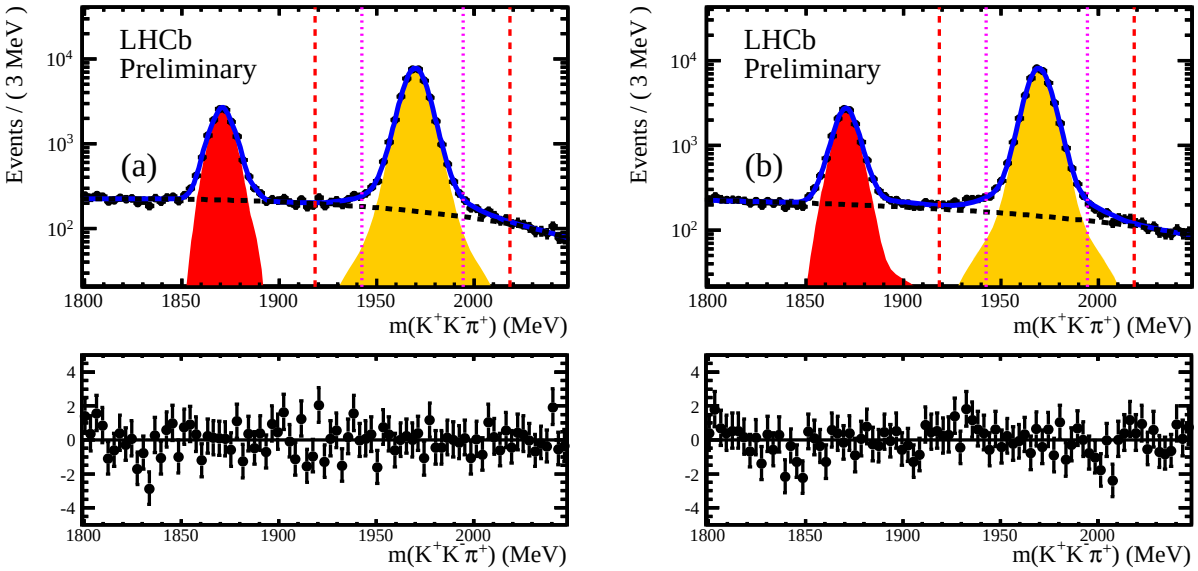

Figure 10: The invariant mass distributions for: (a) $K^+K^-\pi^+$ candidates and (b) $K^+K^-\pi^-$ candidates for magnet up with m(K^+K^-) within 20 MeV of ϕ meson mass. The fitting functions are described in the text. The pull distributions are shown below.

Table 5: A listing of the parameters for the one dimensional fits in overall muon momentum region for both magnet down and magnet up.

Magnet Down	D_s^+	D_s^-
$\mu_1 = \mu_2$	1969.41 ± 0.03	1969.82 ± 0.03
σ_1	5.56 ± 0.08	4.96 ± 0.43
σ_2	10.90 ± 0.42	11.89 ± 0.60
f	0.76 ± 0.03	0.81 ± 0.02
σ_{mean}	6.86 ± 0.18	6.27 ± 0.39
Magnet Up	D_s^+	D_s^-
$\mu_1 = \mu_2$	1969.90 ± 0.04	1969.57 ± 0.04
σ_1	5.47 ± 0.12	9.84 ± 0.52
σ_2	10.66 ± 0.62	6.78 ± 0.42
f	0.75 ± 0.04	0.31 ± 0.05
σ_{mean}	6.79 ± 0.27	7.72 ± 0.36

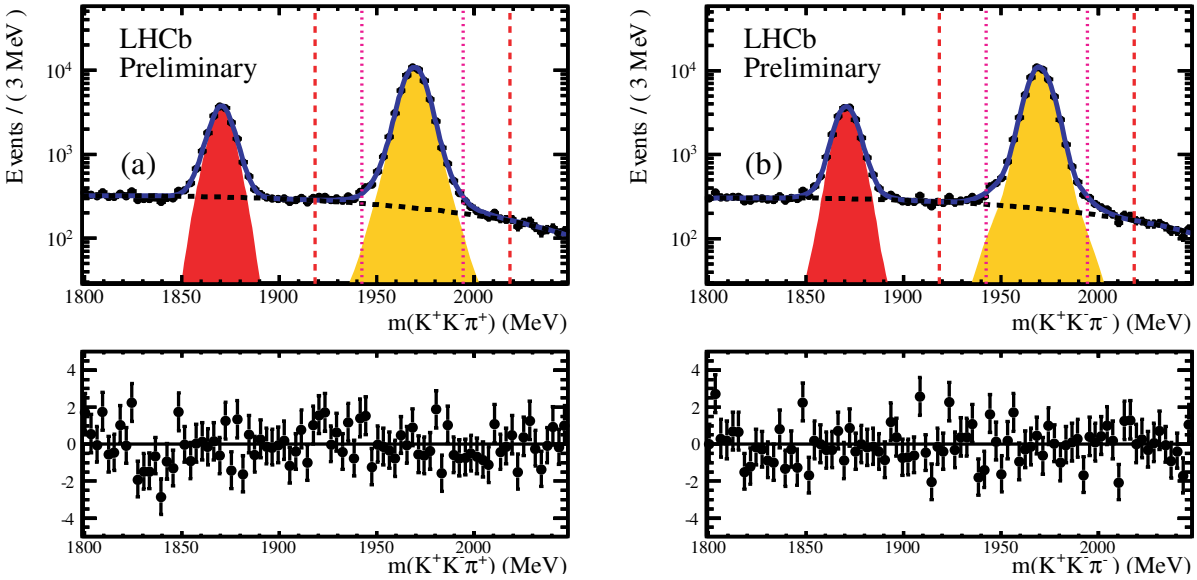

Figure 11: The invariant mass distributions for: (a) $K^+K^-\pi^+$ candidates and (b) $K^+K^-\pi$f candidates for magnet down with m(K^+K^-) within 20 MeV of ϕ meson mass. The fitting functions are described in the text. The pull distributions are shown below.

Table 6: Summary of signal B_s^0 yields (after L0 $p_{\rm T} > 1640\,$MeV cut) for $D_s^+\mu^-$ and $D_s^-\mu^+$ events separately for magnet up and down data. The counting method (mass window $\pm 50\,$MeV) is used as a cross check to the mass fitting method.

	Magnet Up	Magnet Down
mass fitting		
$D_s^-\mu^+$	38742 ± 218	53768 ± 264
$D_s^+\mu^-$	38055 ± 223	54252 ± 259
counting		
$D_s^-\mu^+$	38852 ± 211	53845 ± 262
$D_s^+\mu^-$	38137 ± 220	54354 ± 261

5.1 Signal extraction with kinematic binning

As μ efficiencies are momentum dependent, we study them in 5 different momentum intervals, $6-20\,\text{GeV}$, $20-30\,\text{GeV}$, $30-40\,\text{GeV}$, $40-50\,\text{GeV}$ and $50-100\,\text{GeV}$. In order to improve the accuracy of the efficiency correction, we further divide each of these five momentum bins into a two-dimensional grid consisting of 10 rectangular $p_x(\mu), p_y(\mu)$ regions. To check for systematic effects we also use 8 $p_T(\mu), \phi(\mu)$ domains, where the angle $\phi(\mu)$ is the azimuthal angle defined with respect to the positive x axis, pointing towards the LHCb A side, where "magnet up" defines positive y. These grids have been introduced previously in the section discussing the effects of the dipole magnet on the detector acceptance for charged tracks. We determine the measured asymmetry in each bin, correcting the yields $n_i(D_s^+\mu^-)$, namely the signal yields extracted from mass fits, for the muon ID and L0 and HLT1 trigger efficiency ratios as a function of both p, $p_{\rm T}$ and φ angle and p, p_x and p_y. We then calculate $A_\mu^c(p)$ for magnet up and magnet down as weighted averages of $(A_\mu^c)_i$ in the magnet up and magnet down samples for the two different calibration schemes (4 weighted averages). Our final result is the arithmetic average of the four determinations with magnet UP and magnet DOWN data.

6 Muon Related Detection Asymmetries

6.1 Introduction

The muon efficiencies, $\varepsilon_{\rm ID}(\mu^\pm)$, account for the muon related L0 and HLT1 trigger efficiencies. In a previous study (LHCb-ANA-2012-054) we have investigated the asymmetries in these three different aspect of the muon detection separately. One of the findings was a strong L0 charge asymmetry at low muon transverse momentum, to the different offsets of the A and C sides of the muon stations, which caused the L0 $p_{\rm T}$ distributions of μ^+ and μ^- samples to be asymmetric, there is $p_{\rm T}$-dependent charge asymmetry in the muon selection implemented with the online L0 trigger [2]. In the analysis using the KS calibration scheme, we use the same approach described in this talk to reduce this asymmetry, namely we substitute the "old" L0 $p_{\rm T}$ with new ones generated in a new Look Up Table (LUT) derived by associating each possible M1-M2 combination for L0 Muon candidates with $p_{\rm T}$ derived from the corresponding measured track parameter in the inclusive J/ψ calibration sample. This highly suppressed the old asymmetry. Since the LUT does not contain all possible combinations, there is about $0.3-0.4\%$ loss of events due to this incompleteness as shown in Table 7. The same "fix" is applied to both signal B_s^0 sample and control samples which are then used to determine muon ID and trigger efficiencies. On the other hand, the MS calibration scheme relies on a calibration line stored in a microDST format that does not permit this reprocessing. In this case we use the non-reprocessed data and we account for the additional asymmetry with the MS derived correction factor.

[2] More information can be found in J. Cogan's talk "http://marwww.in2p3.fr/∼cogan/muongeom/20120312_l0muonasym.pdf"

Table 7: Statistics of the efficiency loss due to the table incompleteness in different data samples

		L0Muon TOS candidates	"lost" candidates
MinBias J/ψ			
Magnet Up	μ^+	1011603	3339
Magnet Up	μ^-	980803	3571
Magnet Down	μ^+	1404060	5186
Magnet Down	μ^-	1458986	4754
Signal B_s^0			
Magnet Up	μ^+	586760	2296
Magnet Up	μ^-	557314	2374
Magnet Down	μ^+	800016	3362
Magnet Down	μ^-	849881	3345
PID J/ψ			
Magnet Up	μ^+	8877257	32370
Magnet Up	μ^-	8508042	33895
Magnet Down	μ^+	11839395	47060
Magnet Down	μ^-	12630073	46187

6.2 Efficiencies determined with the muon selected calibration sample

The muons used in this study have been selected from the full 2011 dataset using the MuIDCalib_JpsiFromBNoPIDNoMip stripping line. Candidates are chosen such that one muon, the *tag*, is identified using the muon chambers, such that IsMuon(tag) is equal to 1. Thus we refer to this sample as muon selected (MS). In some figures this sample is identified as PID. The *probe* muon is identified as a long track that forms a good vertex with the tag muon and which forms an invariant mass with the tag muon within a 200 MeV mass window of the PDG J/ψ mass. No muon identification (PID) information requirement is applied to the probe track. The full set of tag and probe cuts are listed in Table 8.

The calibration J/ψ sample can be divided into two groups depending upon the outcome of specific muon selection criteria, identified as *pass* events or *fail* events depending upon the outcome of the selection algorithm studied. Yields are extracted with a one dimensional binned fit, where binned fit is executed using RooFit (vX.Y, etc). The J/ψ resonance is fit with a double *crystal ball* function where the two Crystal Ball PDFs can have different widths but are constrained to have the same mean, alpha and n. The background is modeled with a linear function. The total, *pass* and *fail* data are fitted simultaneously to extract the efficiency of a specific selection. Figure 12 shows an example of these fits. The ratio between J/ψ signal yields for probe tracks passing the

Table 8: Selections on the tag muon and the probe muon candidate

Item	Requirement
Common cuts on both tag and probe	
Kinematics	long track χ^2/NDF < 3 $p > 3$ GeV; $p_{\rm T} > 0.8$ GeV IP $\chi^2 > 10$; η [2,5] Clone Killer
Tag specific selection criteria	
Kinematics	PIDMu> 0&nShare=0 isMuon; $p > 6$ GeV $p_{\rm T} > 1.5$ GeV& IP$\chi^2 > 25$
Trigger requirements	(L0 + Hlt1 + HLT2) TIS
J/ψ selection	within $\pm$ 200 MeV of PDG mass vertex χ^2/dof < 8 separation from primary vertex $\chi^2 > 225$

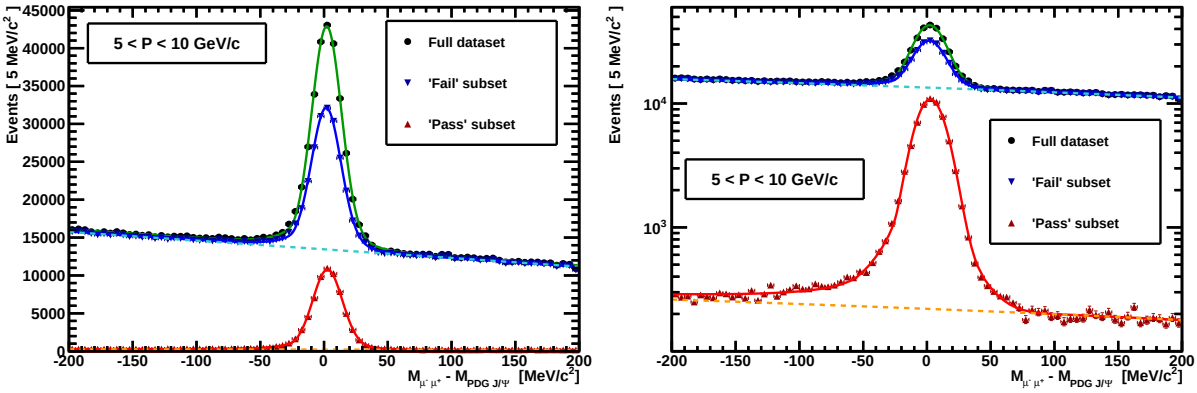

Figure 12: **Left:** The fit to the invariant mass of the combined tag and probe muon system for a particular range of probe momentum. The data fit to the full data sample, the subset that pass the $a^s_{\rm sl}$ muon selection and the subset that fail are all shown. **Right:** The same fit with on a logarithmic scale. The lower mass side radiative tail can be seen to extend almost to the end of the edge of the low mass sideband.

muon selection criteria, and the corresponding yields in the original tag and probe sample determines the muon identification efficiency. A similar method is applied to derive the other efficiency corrections.

In order to quantify the uncertainty in the efficiency ratios introduced by the fitting procedure, two different methods have been used to separate the resonant J/ψ events from the background. In the first the $\mu^+\mu^-$ invariant mass spectrum is fit to a double-

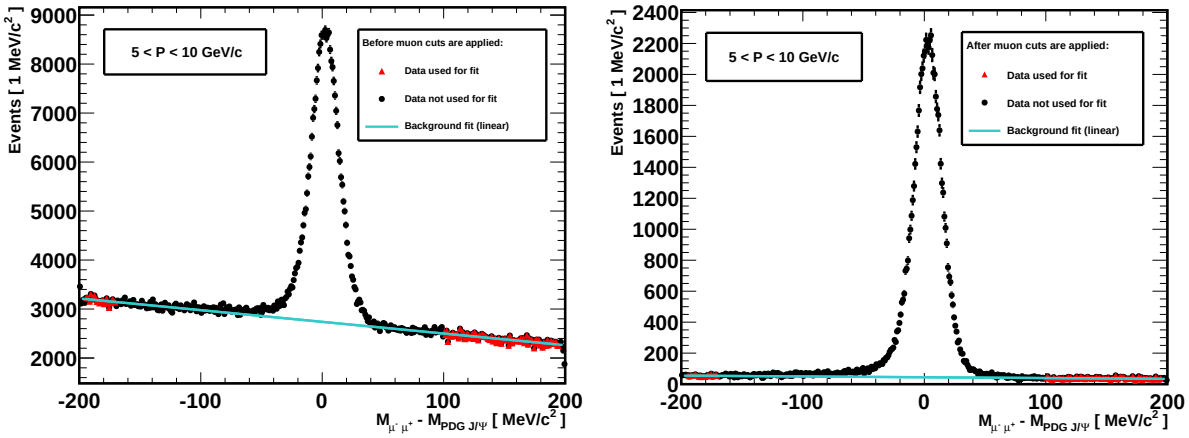

Figure 13: **Left:** Before the $a^s_{\rm sl}$ muon selection is applied. The number of background events is evaluated using the linear fit to only the data represented with red triangles. The number of J/ψ events is calculated by subtracting the expected number of background events from the total number of data points represented by black circles. **Right:** The same for the candidates that pass the $a^s_{\rm sl}$ muon selection.

Table 9: Summary of the overall calibration J/ψ signal yields, the first row shows number of signals when probe μ^+ is within the kinematic region p [6,100] GeV and $p_{\rm T}$ [1.5,10] GeV, while the second row is for probe μ^- to be within the region.

Muon charge	Magnet Up	Magnet Down
μ^+	756310 ± 1420	1080560 ± 1671
μ^-	773125 ± 1377	1061030 ± 1421

Crystal Ball signal function plus a linear background function. The second uses the mass spectrum sidebands to extrapolate the number of background events present under the J/ψ mass resonance. Both methods assume a linear background shape. In addition, a different PDF, constructed with three Gaussians, two of which share the same mean, has been used as well. An example of this method is shown by Figure 13.

The fitting method has smaller errors and is used as the nominal method to extract the desired yields. The background extrapolation method is used as a cross check of the fitting method and is used to quantify the systematic error associated with the assumed shape of the fit model.

Table 9 shows a summary of the overall statistics in the PID J/ψ calibration sample when the probe TIS muons are within the kinematic region p [6,100] GeV and $p_{\rm T}$ [1.5,10] GeV. There are about 1.8 M J/ψ signals to start with for the efficiency measurements.

Table 10: Kinematic selections applied on the two muon candidate tracks to select a minimum bias J/ψ.

Item	Requirement
Kinematics	$p > 3\,\text{GeV}$
	$p_{\text{T}} > 1.5\,\text{GeV}$
Track quality	$\chi^2 < 3$
IP	IP $\chi^2 > 4$
Misc.	η [2,5]; CloneKiller
$m(\mu^+\mu^-)$	Within 150 MeV of J/ψ mass
Vertex fit	$\chi^2/\text{NDF} < 11$
Event Multiplicity	longTracks< 250

6.3 Kinematically selected J/ψ calibration sample

From all *BeautyToCharm* hadronic events, we select the J/ψ combination in events including trigger selected hadronic B decays, ("TOS" L0 and Hlt is required on the "Beauty" particle). The kinematic cuts applied on the two muon candidate tracks to select a J/ψ are listed in Table 10. We refer to this sample as kinematically selected (KS) . While no TIS requirement is applied in the initial kinematic selection, the "probe" muon candidate, used to measure the muon identification efficiency is explicitly required to be TIS. In order to measure the muon identification efficiency, we select a "tag muon," applying the same muon identification criteria used in the signal analysis, and use the other track candidate as "probe muon."

The overall signal yields for magnet up and down are shown in Table 11, there are about 1.5 M J/ψ candidates selected in total for efficiency studies, which is comparable to the statistics in the MS calibration J/ψ sample. While no TIS requirement is applied in the initial kinematic selection, the "probe" muon candidate, used to measure the muon identification efficiency is explicitly required to be TIS. In order to measure the muon identification efficiency, we select a "tag muon," applying the same muon identification criteria used in the signal analysis, and use the other track candidate as "probe muon." Fig. 14 shows the J/ψ candidate invariant mass distribution with these criteria.

Table 11 shows a summary of the overall statistics in the MS J/ψ calibration sample when the probe TIS muons are within the kinematic region p [6,100] GeV and p_{T} [1.5,10] GeV. There are about 1.8 M J/ψ signals to start with for the efficiency measurements.

We have studied kinematic properties of the muons in the signal sample and in the two J/ψ calibration sample to assess the similarities between them. Fig. 15 shows a comparison between the momentum spectra. Fig. 16 shows the long track spectra, Fig. 18 shows the φ angle spectra, and Fig. 17 shows p_{T} spectra. The p_{T} and φ angle distribution in each momentum interval studied separately are shown in Fig. 19 and Fig. 20. In general there is a good match between the muon spectra in the three samples studied. The p_{T} spectrum of the muons from the signal sample is harder than the ones in the two calibration samples,

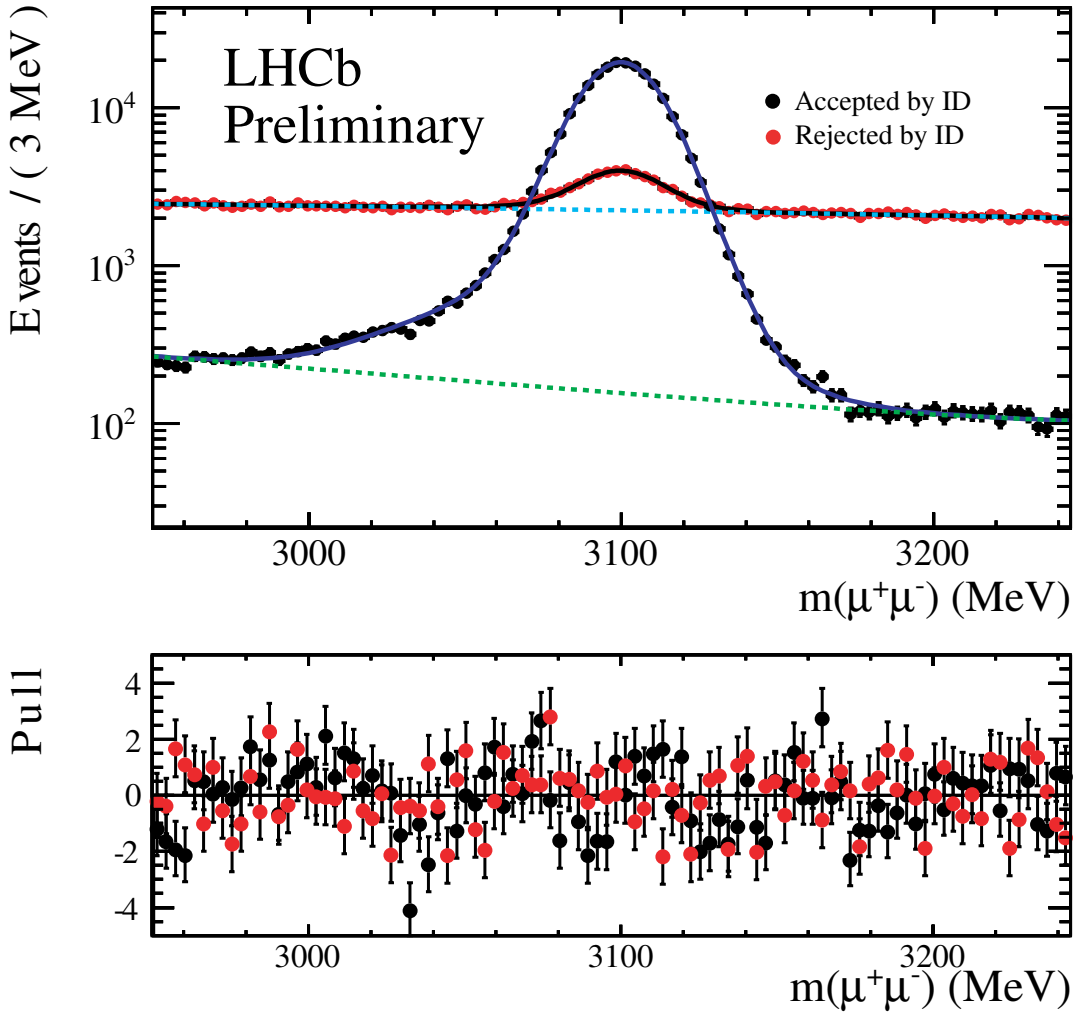

Figure 14: The invariant mass distributions of $\mu^+\mu^-$ for the kinematically selected J/ψ events with TIS required on the probe muon track and ID required on the other muon track, where the red points are the events rejected by Muon ID requirements and black points are the ones accepted by Muon ID. The fitting functions are described in the text.

where the standard LHCb calibration sample includes a higher fraction of muons with very low $p_{\rm T}$.

Table 11: Overall signal yields of minimum biased kinematically selected J/ψ candidates, muons are required to have p [6,100] GeV and $p_{\rm T}$ [1.5,10] GeV. The third and fourth rows show number of signal tracks when TIS is further required on the probe muon track. The last two rows show number of signals after ID requirements are applied sequentially on the other muon track.

Muon charge	Magnet Up	Magnet Down
Kinematically selected J/ψ		
μ^+	633931 ± 2314	906517 ± 2766
μ^-	632411 ± 2377	903825 ± 2687
after TIS is required on the probe muon		
μ^+	256840 ± 1502	372268 ± 2124
μ^-	261667 ± 1454	363036 ± 1809
after ID is required on the other muon ("tag leg")		
μ^+	246770 ± 826	357448 ± 987
μ^-	252282 ± 844	350892 ± 952

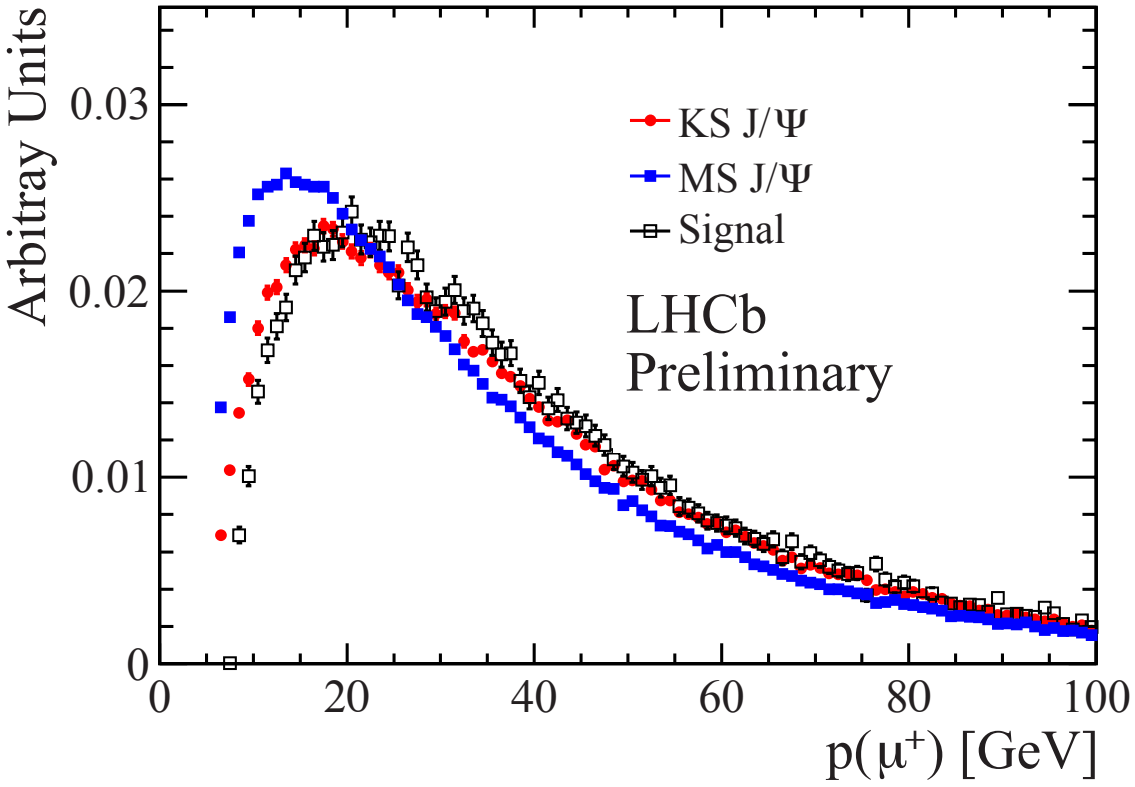

Figure 15: The muon momentum distributions from the MS calibration sample (probe TIS muons), KS calibration sample and signal muons, all spectra are normalized to unit area. Only magnet up data for μ^+ are shown here. Background events are subtracted in the two J/ψ samples by using J/ψ mass sidebands and in the signal sample by using D_s^+ mass sidebands.

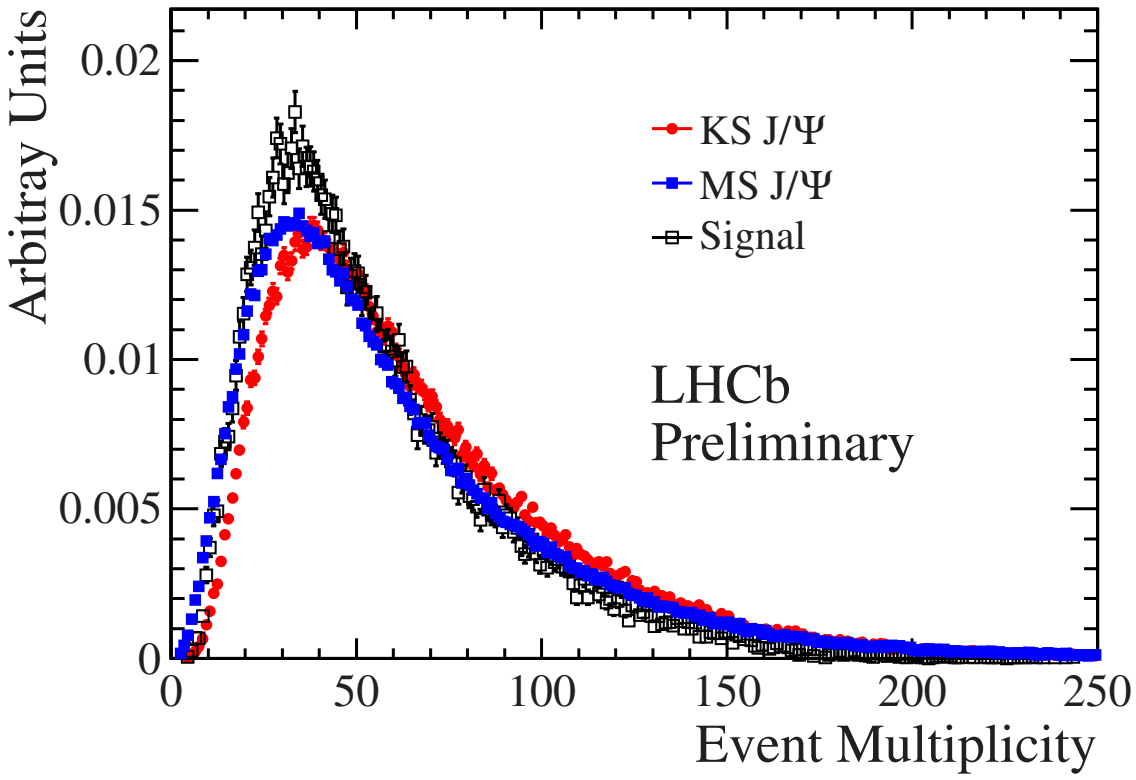

Figure 16: The long track multiplicity distributions for the MS calibration sample, KS sample and signal sample, all spectra are normalized to unit area. Only magnet up data for μ^+ are shown here. Background events are subtracted in the two J/ψ samples by using J/ψ mass sidebands and in the signal sample by using D_s^+ mass sidebands.

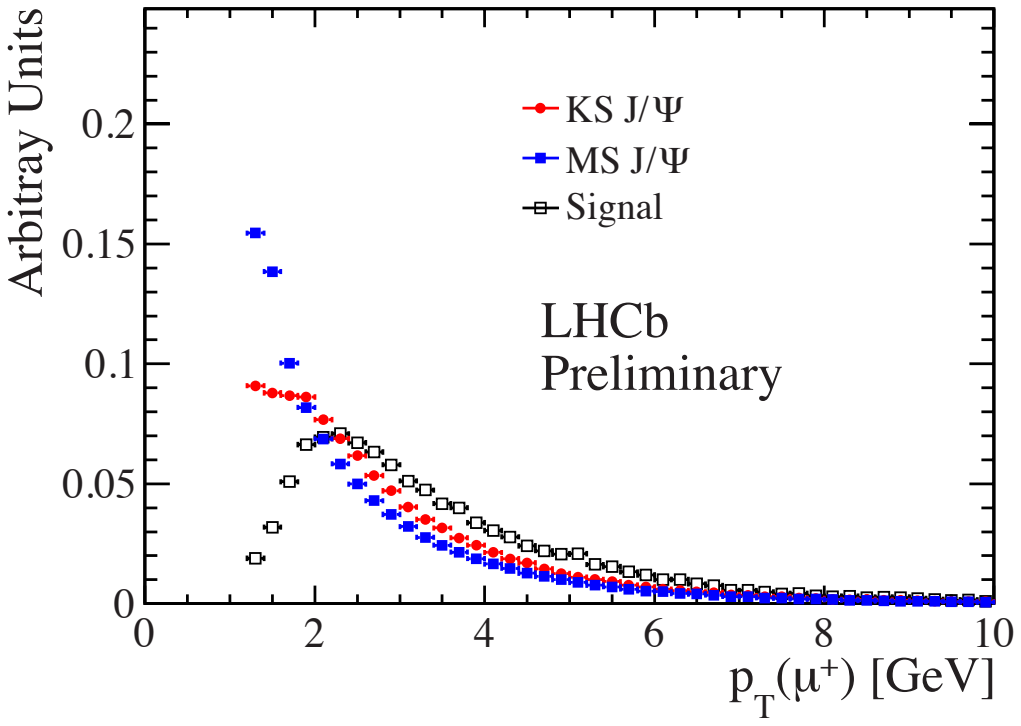

Figure 17: The muon $p_{\rm T}$ distributions for the PID calibration sample, KS sample and signal sample, all spectra are normalized to unit area. Only magnet up data for μ^+ are shown here. Background events are subtracted in the two J/ψ samples by using J/ψ mass sidebands and in the signal sample by using D_s^+ mass sidebands.

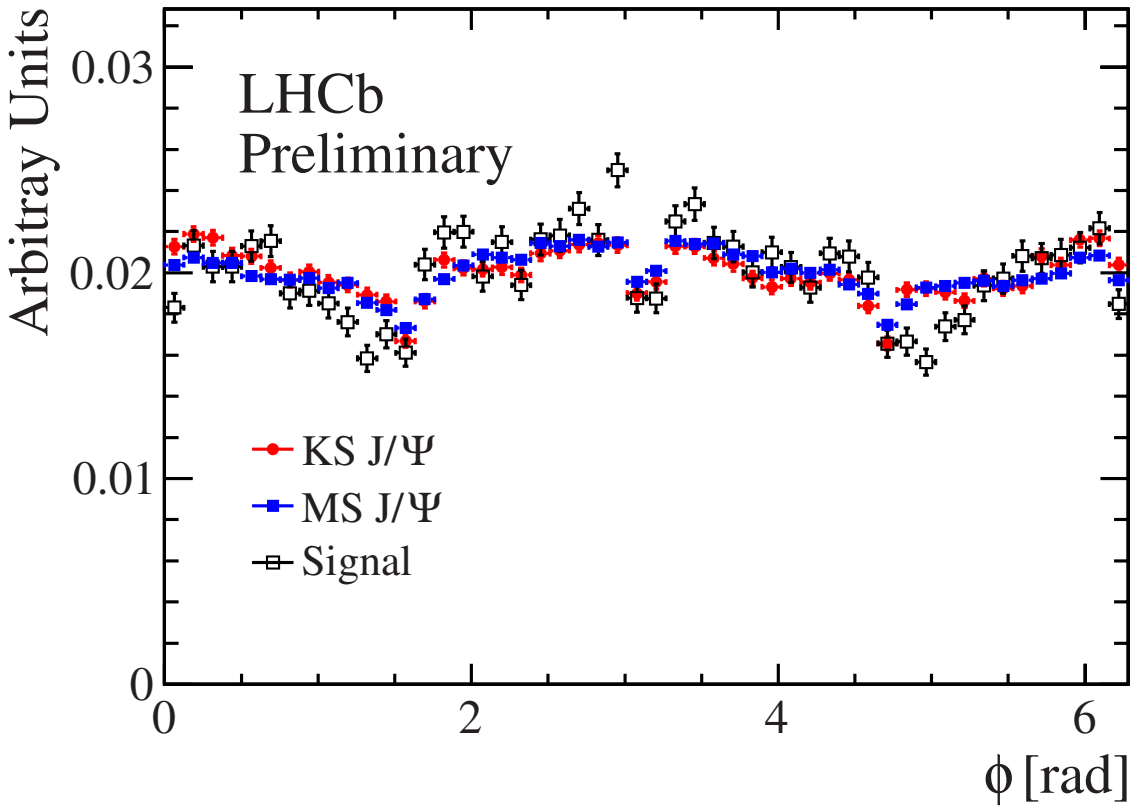

Figure 18: The muon φ angle distributions for the MS calibration sample, KS sample and signal sample, all spectra are normalized to unit area. Only magnet up data for μ^+ are shown here. Background events are subtracted in the two J/ψ samples by using J/ψ mass sidebands and in the signal sample by using D_s^+ mass sidebands.

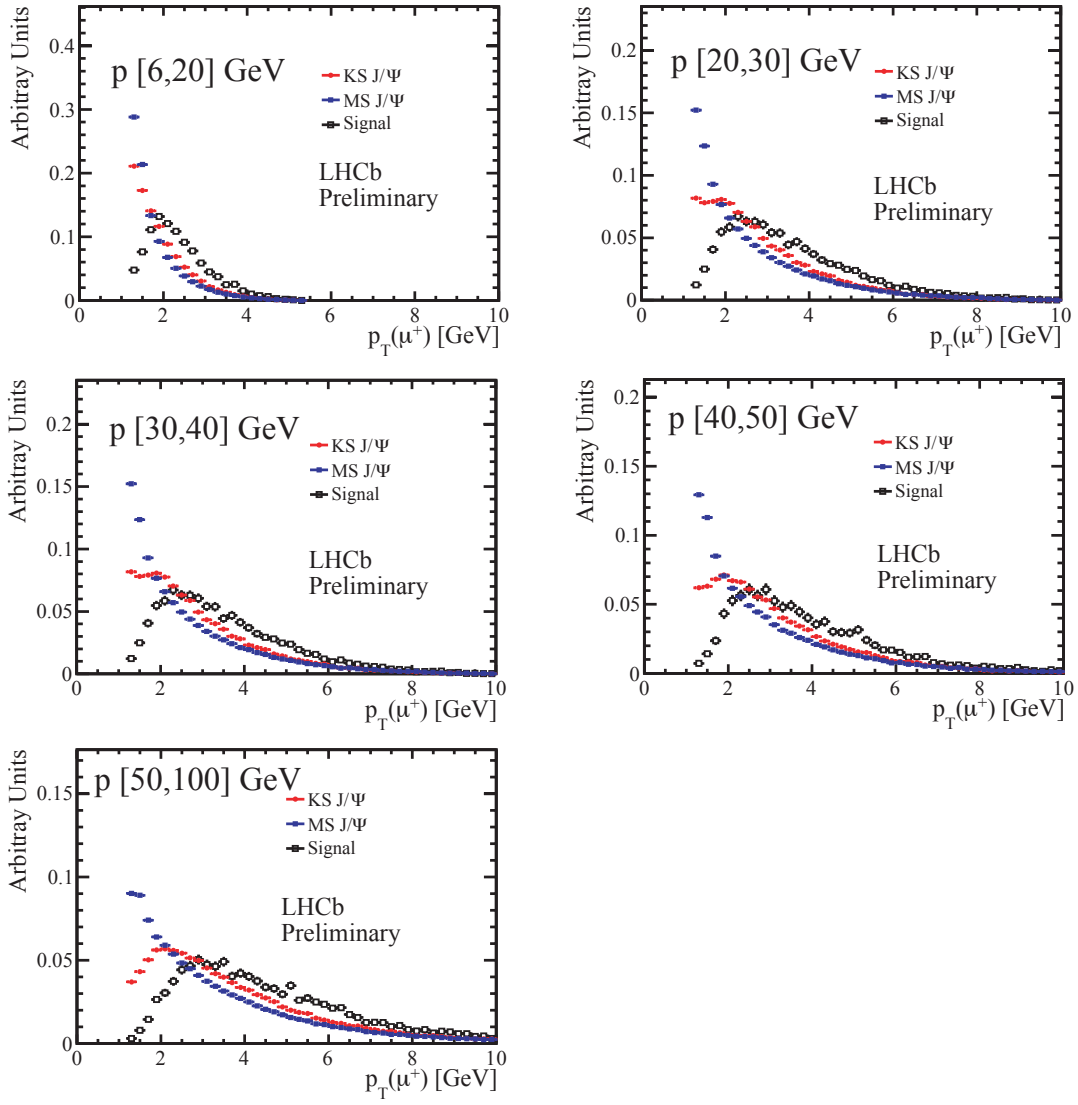

Figure 19: The muon p_{T} distributions for the MS calibration sample, KS sample and signal sample in each momentum slice, all spectra are normalized to unit area. Only magnet up data for μ^+ are shown here. Background events are subtracted in the two J/ψ samples by using J/ψ mass sidebands and in the signal sample by using D_s^+ mass sidebands.

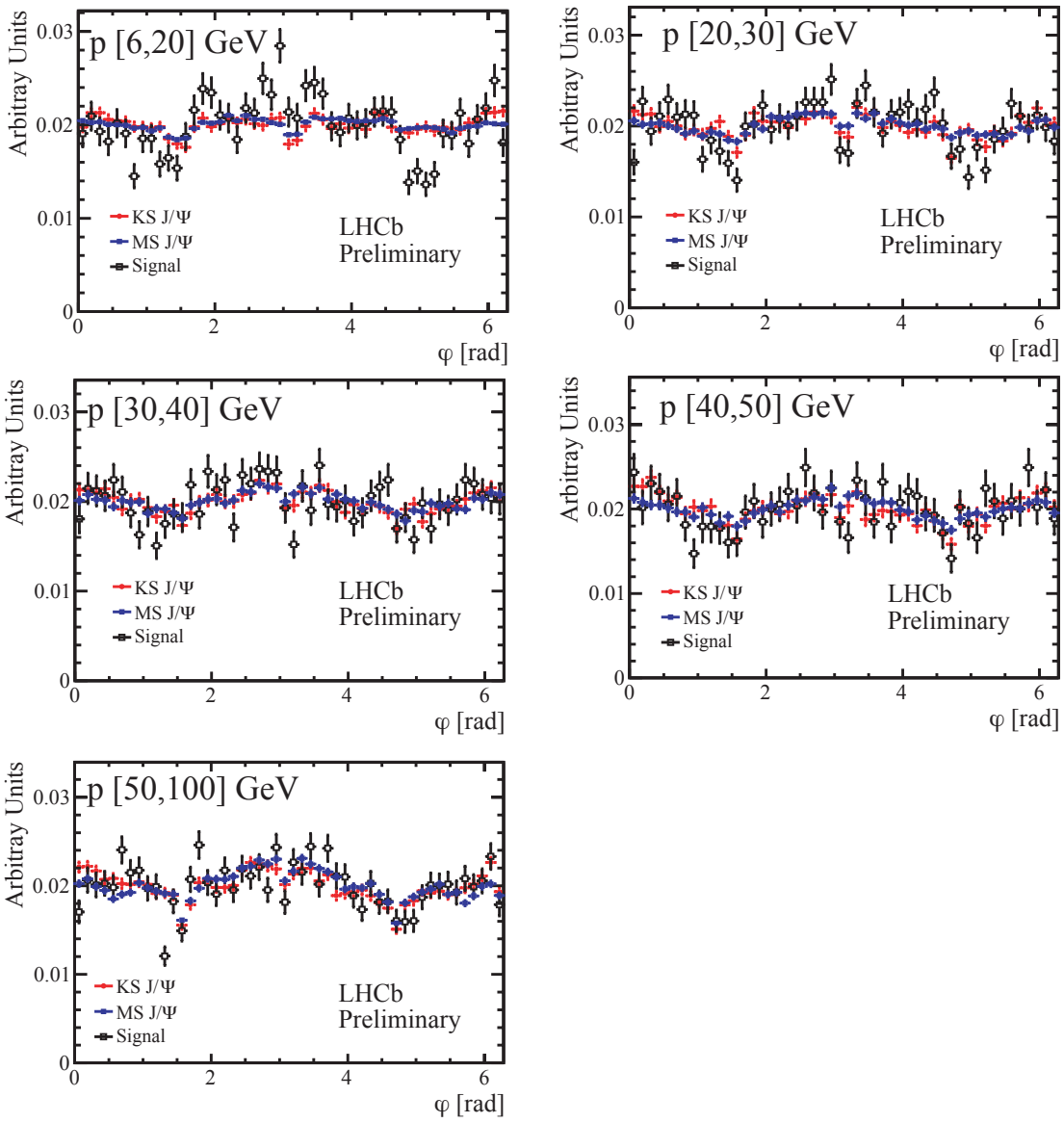

Figure 20: The muon φ angle distributions for the MS calibration sample, KS sample and signal sample in each momentum slice, all spectra are normalized to unit area. Only magnet up data for μ^+ are shown here. Background events are subtracted in the two J/ψ samples by using J/ψ mass sidebands and in the signal sample by using D_s^+ mass sidebands.

6.4 Muon efficiency ratios

When using the MS calibration sample, the LUT correction is not applied as there were some technical difficulties in reprocessing the muon related information due to the fact that this calibration sample is available only as a micro-DST. Thus we need to rely on the muon efficiency ratio to account for this effect. In order to accomplish this goal with sufficient accuracy, the MS sample is further divided into fine kinematic bins at low muon candidate $p_{\rm T}$, as it is in this region that the L0 trigger bias is most prevalent. With the $pp_t\phi$binning scheme this is simply achieved by measuring the signal yields and muon selection efficiencies with fine bins of $p_{\rm T}$, resulting in 100 sub-bins per magnetic field polarity. For the pp_xp_yscheme a fourth dimension is required. In addition to the bins of p, p_x and p_y, the muon selection efficiencies are measured in bins of $p_{\rm T}$, where the binning thresholds are shown in Figure 21(a). The statistical accuracy of the MS calibration sample allows this finer kinematic segmentation. We do not have comparable statistical accuracy in the signal sample, thus we determine a weighted average of the muon efficiencies determined in this additional $p_{\rm T}$ dependent grid. We use use the signal muon $p_{\rm T}$ spectrum in each kinematic bin. Figure 22 shows the efficiency ratios obtained with the KS and MS calibration samples as a function of the muon momentum, and Figure 23 shows the efficiency ratios as a function of the muon transverse momentum. The correction is higher with the latter method because of the higher L0 asymmetry.

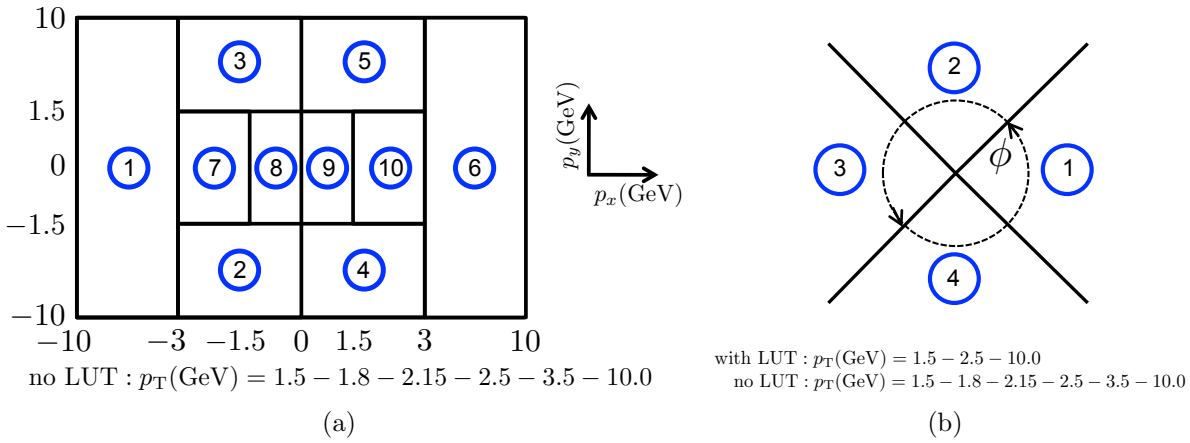

Figure 21: The revised binning schemes. In **a)** the pp_xp_yscheme is shown. The muon efficiencies are determined in the additional $p_{\rm T}$ bins when the LUT correction is not applied. In **b)** the $pp_t\phi$scheme is shown. There are two $p_{\rm T}$ binning definitions, the finer of which is used when the LUT correction is not applied.

Table 12 and Table 13 show the ID efficiencies of μ^+ only in 60 $p-p_{\rm T}-\varphi$ bins obtained from the standard muon identification calibration sample for magnet up and down data, respectively.

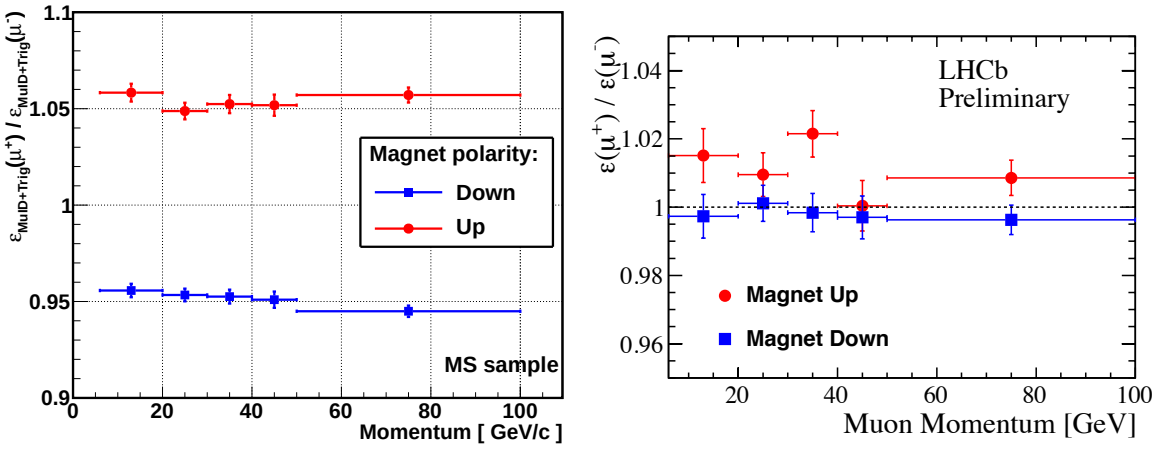

Figure 22: The relative muon efficiency as a function of muon momentum using: (a) the MS J/ψ sample and (b) the KS J/ψ sample (TIS required on the probe muon).

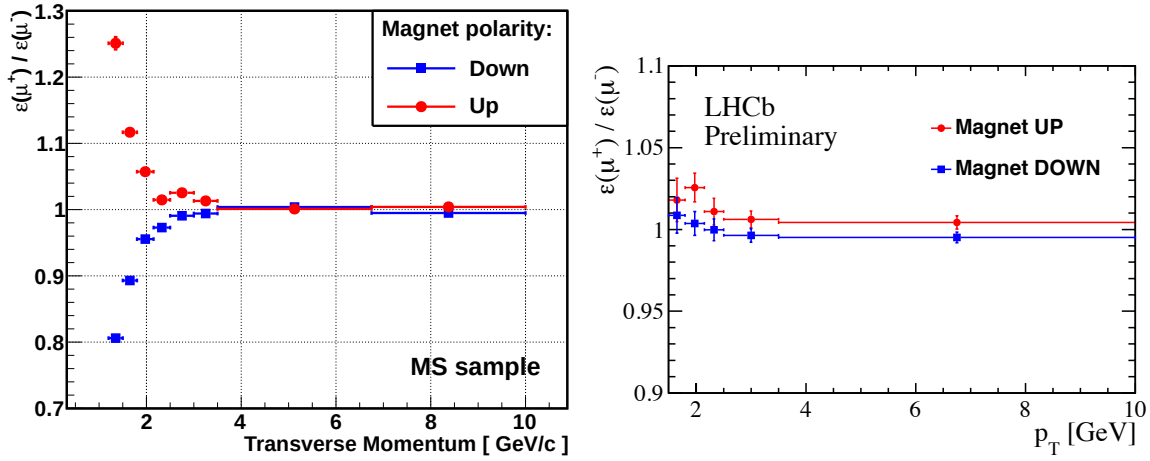

Figure 23: The relative muon efficiency as a function of muon momentum using: (a) the MS J/ψ sample and (b) the KS J/ψ sample (TIS required on the probe muon).

Table 12: Muon ID efficiency table using MS muon calibration J/ψ sample, only magnet up data is shown.

$\varepsilon_{ID}(\mu^+)$ [%]		φ bin 1	φ bin 2	φ bin 3	φ bin 4
p [GeV]	p_{T} [GeV]				
6-20	1.5-2.5	88.1 ± 0.3	93.5 ± 0.3	85.7 ± 0.3	93.2 ± 0.3
6-20	2.5-10.0	94.7 ± 0.4	95.4 ± 0.5	89.8 ± 0.5	92.5 ± 0.5
20-30	1.5-2.5	88.5 ± 0.5	94.3 ± 0.5	95.7 ± 0.4	93.7 ± 0.5
20-30	2.5-10.0	97.1 ± 0.3	96.8 ± 0.4	96.9 ± 0.3	96.0 ± 0.4
30-40	1.5-2.5	83.6 ± 0.6	93.2 ± 0.6	94.4 ± 0.6	93.8 ± 0.6
30-40	2.5-10.0	96.8 ± 0.4	96.4 ± 0.4	97.3 ± 0.4	96.4 ± 0.4
40-50	1.5-2.5	69.5 ± 0.8	93.1 ± 0.8	95.7 ± 0.7	93.9 ± 0.7
40-50	2.5-10.0	96.1 ± 0.4	95.7 ± 0.5	96.9 ± 0.4	96.1 ± 0.5
50-100	1.5-2.5	33.0 ± 0.5	89.9 ± 0.6	95.1 ± 0.5	89.1 ± 0.6
50-100	2.5-10.0	94.4 ± 0.3	95.3 ± 0.3	96.3 ± 0.3	95.8 ± 0.3

Table 13: Muon ID efficiency table using MS muon calibration J/ψ sample, only magnet down data is shown.

$\varepsilon_{ID}(\mu^+)$ [%]		φ bin 1	φ bin 2	φ bin 3	φ bin 4
p [GeV]	p_{T} [GeV]				
6-20	1.5-2.5	85.5 ± 0.3	94.8 ± 0.3	87.8 ± 0.3	93.5 ± 0.3
6-20	2.5-10.0	90.4 ± 0.4	96.0 ± 0.5	93.1 ± 0.3	92.8 ± 0.4
20-30	1.5-2.5	95.4 ± 0.4	94.0 ± 0.4	87.5 ± 0.4	94.6 ± 0.4
20-30	2.5-10.0	97.6 ± 0.3	96.7 ± 0.3	96.5 ± 0.3	96.5 ± 0.3
30-40	1.5-2.5	95.0 ± 0.5	93.6 ± 0.5	81.6 ± 0.5	95.3 ± 0.5
30-40	2.5-10.0	97.1 ± 0.3	96.2 ± 0.3	97.3 ± 0.3	96.4 ± 0.3
40-50	1.5-2.5	96.1 ± 0.6	94.0 ± 0.6	69.6 ± 0.6	95.4 ± 0.6
40-50	2.5-10.0	96.3 ± 0.4	96.8 ± 0.4	96.3 ± 0.4	96.4 ± 0.4
50-100	1.5-2.5	96.0 ± 0.4	89.0 ± 0.5	32.1 ± 0.4	89.0 ± 0.5
50-100	2.5-10.0	96.6 ± 0.2	95.3 ± 0.3	93.9 ± 0.2	95.4 ± 0.3

Table 14: Overall muon efficiency table using KS J/ψ sample after the operation $q \times p_x$ (p 6-20 GeV).

p 6-20 GeV				
	Mag UP		Mag DOWN	
$q \times p_x - p_y$ bin index	$\varepsilon(\mu^+)$	$\varepsilon(\mu^-)$	$\varepsilon(\mu^+)$	$\varepsilon(\mu^-)$
1	65.6 ± 1.7	62.4 ± 1.7	66.9 ± 1.4	67.7 ± 1.4
2	55.6 ± 0.8	53.3 ± 0.8	49.0 ± 0.7	47.2 ± 0.7
3	56.3 ± 0.8	52.3 ± 0.8	50.1 ± 0.7	50.0 ± 0.7
4	47.7 ± 0.8	49.4 ± 0.8	54.0 ± 0.7	54.8 ± 0.7
5	48.7 ± 0.8	50.2 ± 0.8	55.5 ± 0.7	53.4 ± 0.7
6	69.8 ± 1.7	69.1 ± 1.7	65.7 ± 1.4	65.4 ± 1.5
7	48.5 ± 0.7	47.9 ± 0.6	50.1 ± 0.5	52.3 ± 0.5
8	33.1 ± 0.9	31.9 ± 0.8	28.4 ± 0.6	27.7 ± 0.6
9	28.3 ± 0.8	27.2 ± 0.8	32.5 ± 0.7	32.4 ± 0.7
10	51.8 ± 0.6	50.3 ± 0.6	49.1 ± 0.5	50.0 ± 0.5

Tables 14-18 summarize the efficiency corrections accounting for muon identification, and muon related L0 and HLT1 signal losses. These efficiencies are constructed by selecting "probe muons" that satisfy the muon identification criteria applied in the stripping in a given kinematic bin, are TIS with respect to all the trigger selection algorithms (N_μ). We then determine the corresponding number that also satisfy the muon selection criteria used in this analysis, as well as being TOS with respect to the L0 and HLT1 muon triggers, and having "ptL0">1.6 GeV. This last requirement is necessary to be able to reprocess the muon L0 algorithm with the new look-up-table that suppresses the charge asymmetry discussed before ($N_\mu^{\rm sel}$). The μ selection efficiencies are determined in each kinematic bin as

$$\varepsilon_i = \frac{N_{\mu i}^{\rm sel}}{N_{\mu i}}. \tag{27}$$

Table 15: Overall muon efficiency table using KS J/ψ sample after the operation $q \times p_x$ (p 20-30 GeV).

p 20-30 GeV				
	Mag UP		Mag DOWN	
$q \times p_x - p_y$ bin index	$\varepsilon(\mu^+)$	$\varepsilon(\mu^-)$	$\varepsilon(\mu^+)$	$\varepsilon(\mu^-)$
1	76.9 ± 0.9	75.7 ± 0.9	75.0 ± 0.8	77.1 ± 0.7
2	66.6 ± 0.8	64.2 ± 0.8	61.7 ± 0.7	61.2 ± 0.7
3	64.7 ± 0.8	64.0 ± 0.8	61.1 ± 0.7	60.0 ± 0.7
4	59.0 ± 0.8	60.4 ± 0.8	65.5 ± 0.7	66.2 ± 0.7
5	59.4 ± 0.8	63.1 ± 0.8	66.6 ± 0.6	64.9 ± 0.6
6	77.4 ± 0.9	76.2 ± 0.9	74.6 ± 0.8	76.0 ± 0.8
7	59.6 ± 0.8	57.9 ± 0.8	58.8 ± 0.6	62.1 ± 0.6
8	36.9 ± 1.2	35.6 ± 1.1	35.4 ± 1.0	34.9 ± 1.0
9	35.4 ± 1.2	34.7 ± 1.2	37.4 ± 1.0	36.1 ± 1.0
10	60.8 ± 0.7	59.1 ± 0.7	59.1 ± 0.6	56.9 ± 0.6

Table 16: Overall muon efficiency table using KS J/ψ sample after the operation $q \times p_x$ (p 30-40 GeV).

p 30-40 GeV				
	Mag UP		Mag DOWN	
$q \times p_x - p_y$ bin index	$\varepsilon(\mu^+)$	$\varepsilon(\mu^-)$	$\varepsilon(\mu^+)$	$\varepsilon(\mu^-)$
1	78.4 ± 0.8	75.7 ± 0.9	77.1 ± 0.7	79.7 ± 0.7
2	67.4 ± 0.9	67.1 ± 0.9	65.0 ± 0.8	65.3 ± 0.8
3	69.0 ± 0.9	66.5 ± 0.9	64.8 ± 0.7	62.2 ± 0.7
4	65.3 ± 0.9	65.8 ± 0.9	67.8 ± 0.7	68.9 ± 0.7
5	63.7 ± 0.9	64.1 ± 0.9	67.3 ± 0.7	68.3 ± 0.7
6	77.5 ± 0.8	78.2 ± 0.8	77.0 ± 0.7	76.9 ± 0.7
7	56.6 ± 0.9	53.4 ± 0.9	60.0 ± 0.7	60.6 ± 0.8
8	42.0 ± 1.6	38.8 ± 1.5	35.6 ± 1.2	36.7 ± 1.3
9	36.1 ± 1.5	36.2 ± 1.6	41.2 ± 1.3	40.1 ± 1.3
10	61.5 ± 0.9	59.1 ± 0.9	56.3 ± 0.8	54.7 ± 0.8

Table 17: Overall muon efficiency table using KS J/ψ sample after the operation $q \times p_x$ (p 40-50 GeV).

p 40-50 GeV				
	Mag UP		Mag DOWN	
$q \times p_x - p_y$ bin index	$\varepsilon(\mu^+)$	$\varepsilon(\mu^-)$	$\varepsilon(\mu^+)$	$\varepsilon(\mu^-)$
1	75.4 ± 0.9	77.6 ± 0.9	79.0 ± 0.7	79.3 ± 0.7
2	69.1 ± 1.0	69.0 ± 1.0	66.3 ± 0.9	66.2 ± 0.9
3	70.5 ± 1.0	67.8 ± 1.0	66.0 ± 0.9	66.5 ± 0.9
4	64.8 ± 1.0	65.8 ± 1.1	68.5 ± 0.9	69.5 ± 0.9
5	63.9 ± 1.0	62.9 ± 1.0	68.9 ± 0.9	68.8 ± 0.8
6	80.2 ± 0.8	78.9 ± 0.8	76.5 ± 0.7	76.3 ± 0.7
7	57.8 ± 1.1	60.2 ± 1.1	55.4 ± 0.9	57.8 ± 0.9
8	36.3 ± 2.0	39.7 ± 2.0	31.6 ± 1.5	36.4 ± 1.6
9	38.0 ± 2.0	39.3 ± 2.0	41.8 ± 1.7	36.0 ± 1.7
10	55.6 ± 1.1	55.2 ± 1.1	59.7 ± 1.0	57.0 ± 1.0

Table 18: Overall muon efficiency table using KS J/ψ sample after the operation $q \times p_x$ (p 50-100 GeV).

p 50-100 GeV				
	Mag UP		Mag DOWN	
$q \times p_x - p_y$ bin index	$\varepsilon(\mu^+)$	$\varepsilon(\mu^-)$	$\varepsilon(\mu^+)$	$\varepsilon(\mu^-)$
1	76.2 ± 0.5	76.7 ± 0.5	78.1 ± 0.4	79.7 ± 0.4
2	65.6 ± 0.7	67.3 ± 0.7	63.0 ± 0.6	65.4 ± 0.6
3	68.5 ± 0.7	68.0 ± 0.7	62.5 ± 0.6	62.7 ± 0.6
4	63.7 ± 0.7	63.1 ± 0.7	67.9 ± 0.6	65.9 ± 0.6
5	63.9 ± 0.7	61.4 ± 0.7	67.8 ± 0.6	67.3 ± 0.6
6	78.7 ± 0.5	78.2 ± 0.5	77.5 ± 0.5	77.3 ± 0.5
7	54.2 ± 0.8	55.4 ± 0.8	37.6 ± 0.6	39.4 ± 0.7
8	31.9 ± 1.4	30.8 ± 1.3	26.7 ± 1.2	26.9 ± 1.2
9	27.0 ± 1.5	25.4 ± 1.3	34.3 ± 1.3	29.7 ± 1.2
10	39.1 ± 0.8	36.4 ± 0.7	57.2 ± 0.7	54.8 ± 0.7

P_μ range	Efficiency ratio, $\epsilon_{\mu^+}/\epsilon_{\mu^-}$	
(GeV)	(magnet-up)	(magnet-down)
3–20	0.9968 ± 0.0076	1.0004 ± 0.0060
20–30	1.0033 ± 0.0060	1.0168 ± 0.0055
30–40	1.0034 ± 0.0061	0.9969 ± 0.0054
40–50	1.0007 ± 0.0068	0.9985 ± 0.0062
50–100	0.9936 ± 0.0042	1.0023 ± 0.0038

Table 19: Correction factors to be applied to the HLT2 MuTopo (not ϕ) sample.

7 Studies on HLT2 trigger biases

In order to assess potential biases introduced by the HLT2 algorithms including a muon selection, we use the process $B \to D\mu\nu$, with $D \to K\pi\pi$, which has a similar topology as the signal studied, but has roughly a factor of 16 higher rate. In this section, we will refer to the kaon as "H1", the lower(higher) p_T pions as "H2(H3)".

The $K\pi\pi$ selection includes the same requirements as for the $\phi\pi$ sample except for those that are specific to the $\phi \to KK$ decay (mass, vertex and kaon PID requirements). The muon is required to be TOS on the same L0 and Hlt1 lines.

Instead of requiring that the *entire* B candidate is TIS at HLT2, we break the problem down into different components. To a good approximation, the efficiency for the HLT2 to reconstruct a muon, and for these lines to select that muon, can be determined as follows: the denominator includes events in which the $D \to K\pi\pi$ is TOS on the HLT2Topo3BodyBBDT. Events are included in the numerator if they further satisty the requirement that the B is TOS on the HLT2TopoMu4BodyBBDT line. Figure 24 shows the resulting efficiency (for magnet down) and the ratio of efficiencies for μ^+ vs μ^- for both magnet polarities. Since the TOS efficiency for the D is significantly higher than the TIS efficiency for the B, this method achieves a statistical precision that is almost three times better.

Similarly, we determine the efficiencies for the HLT2 to reconstruct the D daughters. For example for H1 (the kaon), we can define the denominator as the number of events in which the muon, H2 and H3 are TOS on the HLT2TopoMu3BodyBBDT line. The numerator is then defined as the number of events in which the B is TOS on the HLT2TopoMu4BodyBBDT line. Figure 25 shows, overlaying the three hadrons; the absolute efficiencies (for positively charged hadrons and magnet-down), the ratios of efficiencies for h^+ vs h^-. Figure 26 shows the efficiency ratios after combining results for the three hadrons We conclude that any bias in this HLT2 trigger is less than 10^{-3} at the 68% C.L. Any bias (and its statistical upper limit) will be further suppressed by the fact that we have an OR of 2, 3 and 4 track lines. As this trigger sample is about 1/2 of the whole data set, we assign 5×10^{-4} systematic uncertainty to possible HLT2 charge asymmetries.

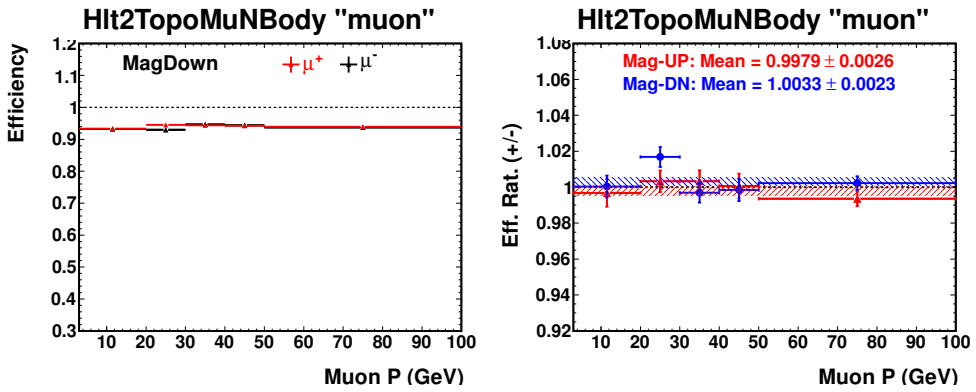

Figure 24: Left: The efficiency for the muon part of the HLT2 topological lines (magnet-down only). Right: the ratio of efficiencies for μ^+ versus μ^-, separately for magnet-up and magnet-down.

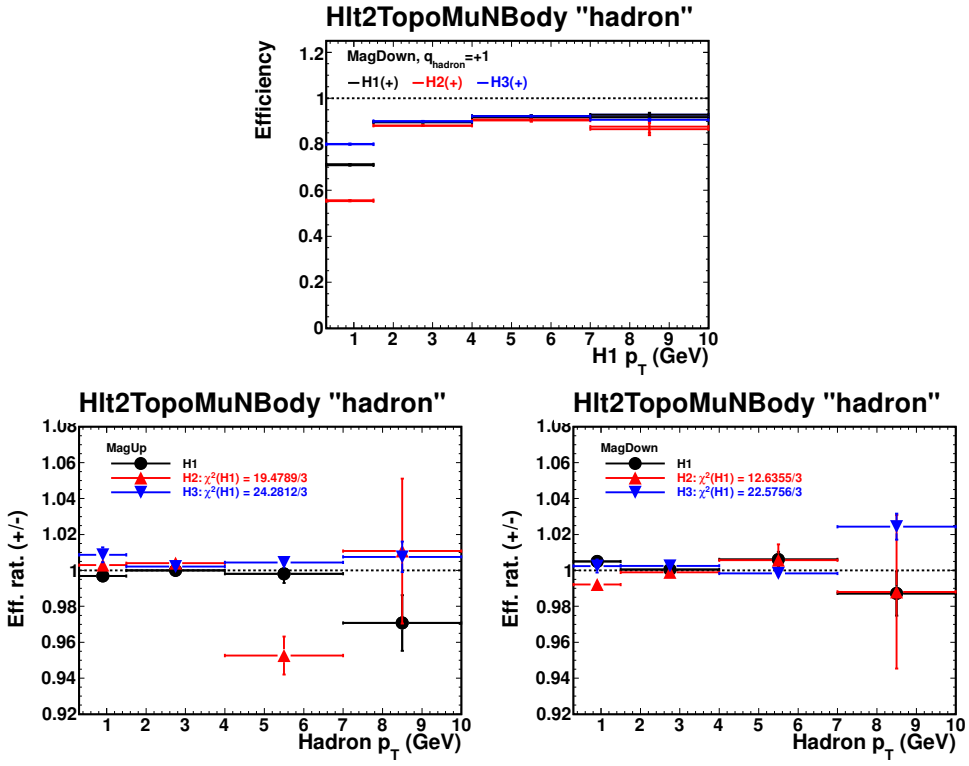

Figure 25: Top row: The approximate efficiency for the HLT2 to reconstruct the D daughters, with a quality that satisfies the topological lines. Bottom row: The ratios of efficiencies for h^+ versus h^- for (left) magnet-up and (right) magnet-down.

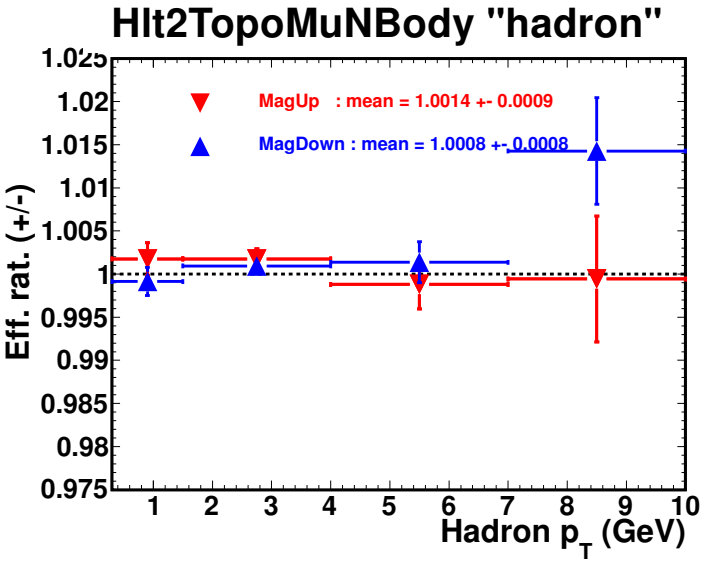

Figure 26: The ratio of HLT2 topological efficiencies (D daughter part) for h^+ versus h^-, after combining the results for the three daughters.

8 Tracking efficiency asymmetry

The final state that we are studying is charge symmetric, thus there is a large cancellation between potential charge dependent detection asymmetry. In fact, if the two pair of tracks were exactly matched in momentum, there would be a perfect cancellation, and thus no correction $A_{\rm track}$ would be necessary. To a large extent, this is true for the K^+K^- pairs, whose momentum spectra are only slightly different, while the π is softer than the μ. Thus we determine $A_{\rm track}$ by adding the two contributions from the K^+K^- and the $\mu^-\pi^+$ pairs.

The charge asymmetry in tracking efficiency is determined using the method described in LHCb-ANA-2012-011(LHCb-PAPER-2012-009) extensively. In summary, the tracking efficiency is determined with a sample of $D^{*+} \to D^0\pi^+$ with $D^0 \to K^-\pi^+\pi^-\pi^+$ candidates, where the D^0 is reconstructed requiring only 3 pions and inferring the momentum of the missing pion from kinematic constraints. We then look for a fully reconstructed $D^0 \to K^-\pi^+\pi^-\pi^+$. The ratio between the number of fully reconstructed and partially reconstructed events for different π kinematic conditions gives the corresponding reconstruction efficiency. There are many subtleties involved, described in LHCb-ANA-2012-011. The signal yields of the fully reconstructed D^{*+} decays are listed in Table 20 and Table 21, where the selections applied on the probe pion in full reconstructions are: $p > 2$ GeV, $p_{\rm T} > 300$ MeV, track $\chi^2/NDF < 4$ and track Clone Killer, to match the selection criteria for the signal sample.

Table 20: Number of signals in full reconstruction versus detected pion momentum for magnet up data

Pion momentum	D^{*+} events	D^{*-} events
2-6 GeV	39595 ± 213	41717 ± 218
6-20 GeV	154363 ± 423	164022 ± 437
20-30 GeV	46649 ± 229	48928 ± 233
30-40 GeV	21551 ± 156	22595 ± 160
40-50 GeV	10794 ± 110	11226 ± 112
50-100 GeV	10980 ± 111	11500 ± 114

The kinematic fitting is used to infer the missing track's momentum in the partially reconstructed sample. The momentum smearing introduced by this procedure is corrected for with a momentum unfolding matrix derived from data by comparing the detected π^+ momentum to its inferred momentum using fully reconstructed events. The unfolded tracking efficiency ratio is shown in Fig. 27 for magnet up and down data separately.

After averaging magnet up and down data, the tracking asymmetry is shown as a function of pion momentum in Fig. 28.

The first approach to extract momentum dependent tracking efficiencies follows the method used for the study of D_s^+ production asymmetry [13], described in detail in LHCb-

Table 21: Number of signals in full reconstruction versus detected pion momentum for magnet down data

Pion momentum	D^{*+} events	D^{*-} events
2-6 GeV	57886 ± 266	59847 ± 271
6-20 GeV	230179 ± 518	236280 ± 525
20-30 GeV	68251 ± 274	70575 ± 279
30-40 GeV	31301 ± 187	32403 ± 191
40-50 GeV	15395 ± 131	16125 ± 134
50-100 GeV	15412 ± 132	16560 ± 137

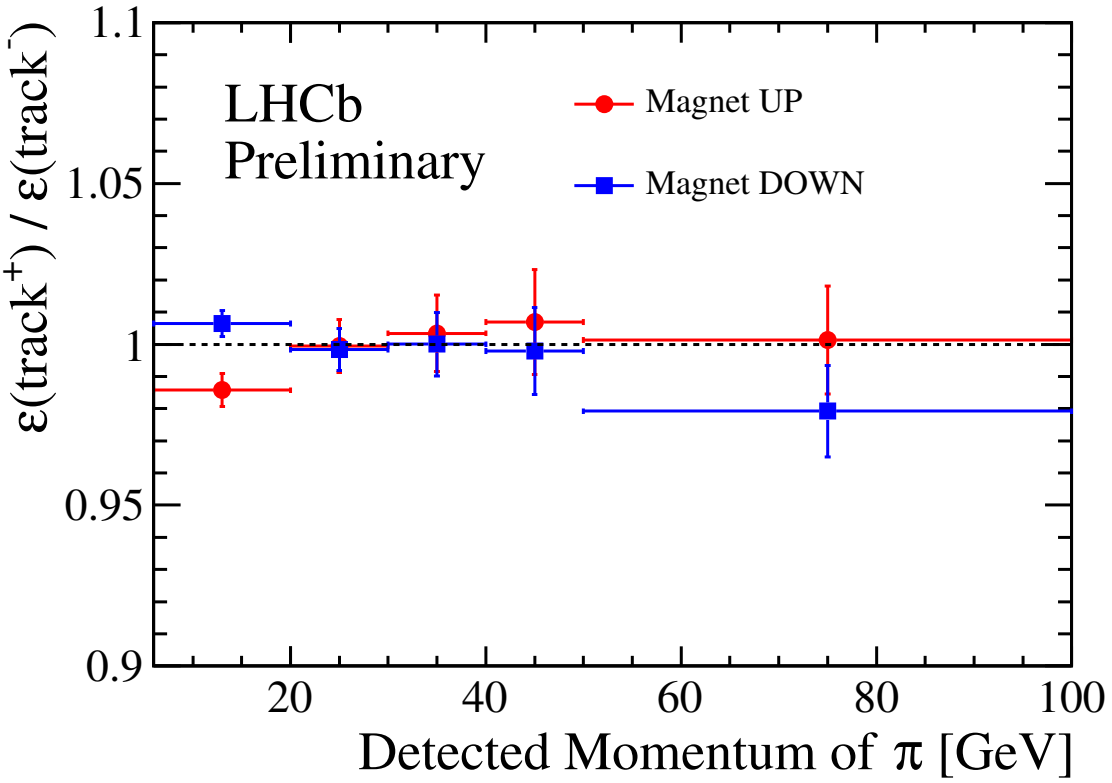

Figure 27: The tracking efficiency ratio as a function of track momentum, which is determined from "partial and full" method using D^{*+} control sample.

ANA-2012-011. In that study we focused on the ϕ dependence of the tracking asymmetry, illustrated in Fig. 29 and summarized in Table 22. The pattern of the oscillation of tracking asymmetries across azimuthal angle ϕ is induced by detector acceptance effects. This geometrical asymmetry can be removed after integrating over φ angle, or averaging

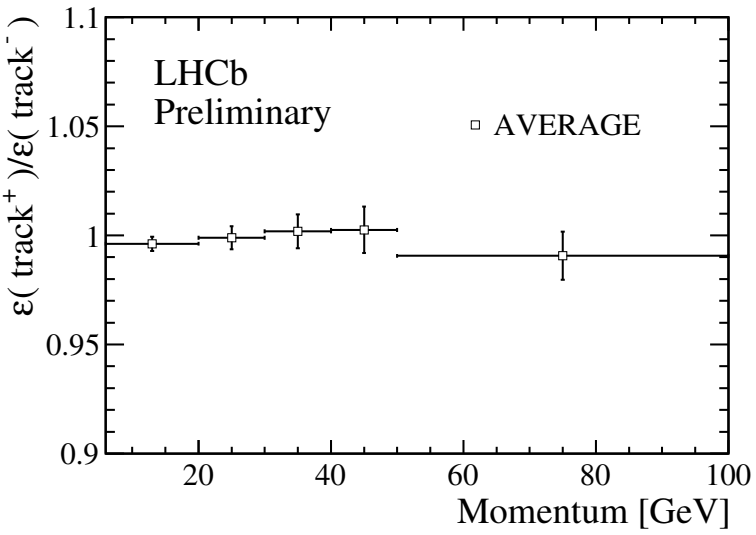

Figure 28: π tracking efficiency ratio determined with the method described in the text averaged over magnet up and magnet down data.

magnet up and down data. Note that the ϕ distribution of the pion and muon tracks are quite similar. The φ angle correlation between pion track and muon track in signal sample is also checked. Fig. 30 and Fig. 31 show these correlations (only magnet up data for $\mu^+\pi^-$ combination). In order to determine the tracking induced asymmetry, we define the average efficiencies for $D_s^-\mu^+$ and $D_s^+\mu^-$ final states as

$$\varepsilon(\pi^-\mu^+) = \frac{\sum_{i,j} N_{ij}(D_s^-\mu^+)}{\sum_{i,j} N_{ij}(D_s^-\mu^+)/\varepsilon_{ij}} \tag{28}$$

where i and j, from 1 to 6, stand for the six momentum intervals, 2–6–20–30–40–50–100 GeV, for μ^+ and π^-, respectively. $N_{ij}(D_s^-\mu^+)$ is the signal yield in each of the 2D correlated bins, shown in Fig. 32 for $D_s^-\mu^+$, $D_s^+\mu^-$, magnet up and down data, respectively, and $\varepsilon_{ij} = \varepsilon_i(\text{track}^+) \times \varepsilon_j(\text{track}^-)$ where $\varepsilon_i(\text{track}^+)$ and $\varepsilon_j(\text{track}^-)$ are measured using the "partial and full" approach from D^* sample and are shown in Table 23. Only the diagonal elements of the covariance matrix are shown as the errors. An analogous definition holds for charge conjugate states

$$\varepsilon(\pi^+\mu^-) = \frac{\sum_{i,j} N_{ij}(D_s^+\mu^-)}{\sum_{i,j} N_{ij}(D_s^+\mu^-)/\varepsilon^*_{ij}} \tag{29}$$

where in this case $\varepsilon^*_{ij} = \varepsilon_i(\text{track}^-) \times \varepsilon_j(\text{track}^+)$. The systematic uncertainty due to the non-perfect cancellation between muon and pion tracking efficiency asymmetry on the $a^{\rm s}_{\rm sl}$ can then be inferred from the difference between $\varepsilon(\pi^-\mu^+)$ and $\varepsilon(\pi^+\mu^-)$. It is estimated to be $A_{\rm track}(\mu^\pm - \pi^\mp) = (0.01 \pm 0.13)\%$. The error is determined with a toy MC that

takes into account the ε_{ij} and ε^*_{ij} correlations introduced by $\varepsilon(\pi^-\mu^+)$ and $\varepsilon(\pi^+\mu^-)$. All bin-by-bin $\varepsilon_i(\text{track}^+)$ and $\varepsilon_j(\text{track}^-)$ are allowed to vary by a Gaussian function with the measured covariance matrix. The mean and the sigma parameters of the Gaussian function that is used to fit the resulting $\varepsilon(\pi^-\mu^+)/\varepsilon(\pi^+\mu^-)$ distribution are taken as the central value and error of the correction factor $A_{\text{track}}(\mu^\pm - \pi^\mp)$.

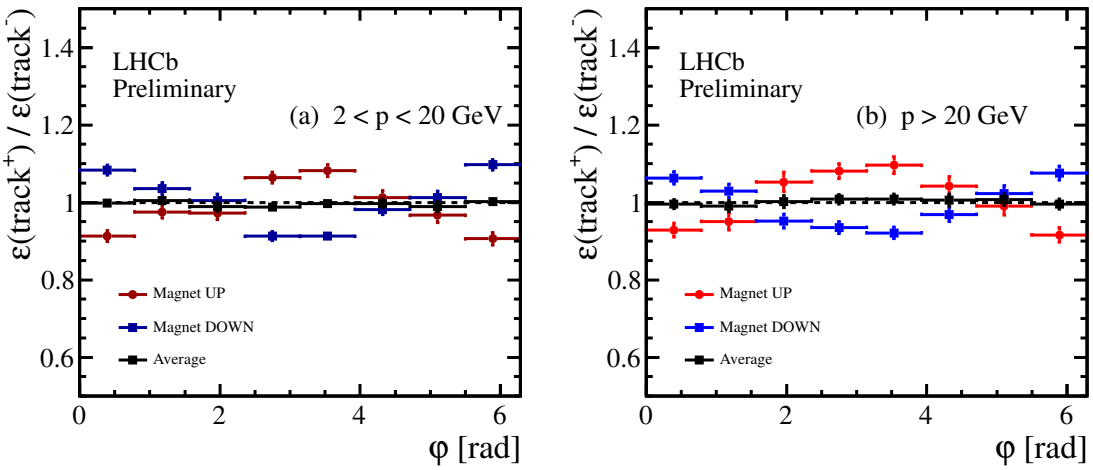

Figure 29: π tracking efficiency ratio as a function of track φ angle in two momentum regions.

Table 22: Summary table of the relative tracking efficiency versus track φ angle in two momentum intervals

φ angle	$p[2, 20]$ GeV		$p > 20$ GeV	
	UP	DOWN	UP	DOWN
$[0, \frac{1}{4}\pi]$	0.913 ± 0.014	1.083 ± 0.013	0.928 ± 0.018	1.063 ± 0.016
$[\frac{1}{4}\pi, \frac{1}{2}\pi]$	0.975 ± 0.015	1.035 ± 0.016	0.951 ± 0.022	1.029 ± 0.018
$[\frac{1}{2}\pi, \frac{3}{4}\pi]$	0.973 ± 0.017	1.005 ± 0.016	1.053 ± 0.025	0.952 ± 0.018
$[\frac{3}{4}\pi, \pi]$	1.064 ± 0.014	0.913 ± 0.012	1.081 ± 0.019	0.935 ± 0.016
$[\pi, \frac{5}{4}\pi]$	1.082 ± 0.016	0.913 ± 0.011	1.096 ± 0.022	0.921 ± 0.015
$[\frac{5}{4}\pi, \frac{3}{2}\pi]$	1.013 ± 0.018	0.982 ± 0.014	1.042 ± 0.024	0.969 ± 0.019
$[\frac{3}{2}\pi, \frac{7}{4}\pi]$	0.967 ± 0.019	1.012 ± 0.017	0.991 ± 0.024	1.023 ± 0.020
$[\frac{7}{4}\pi, 2\pi]$	0.906 ± 0.016	1.097 ± 0.014	0.916 ± 0.019	1.076 ± 0.018

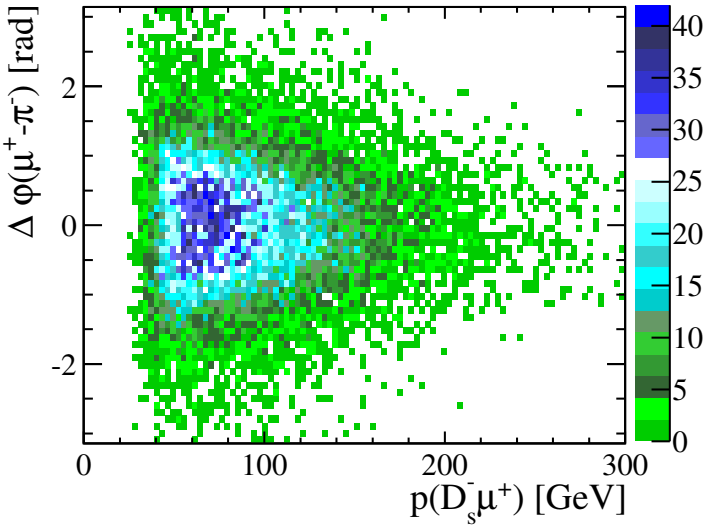

Figure 30: The φ angle correlation between pion track and muon track as a function of B($D_s^- \mu^+$) momentum (only magnet up data for $\mu^+\pi^-$ combination shown here).

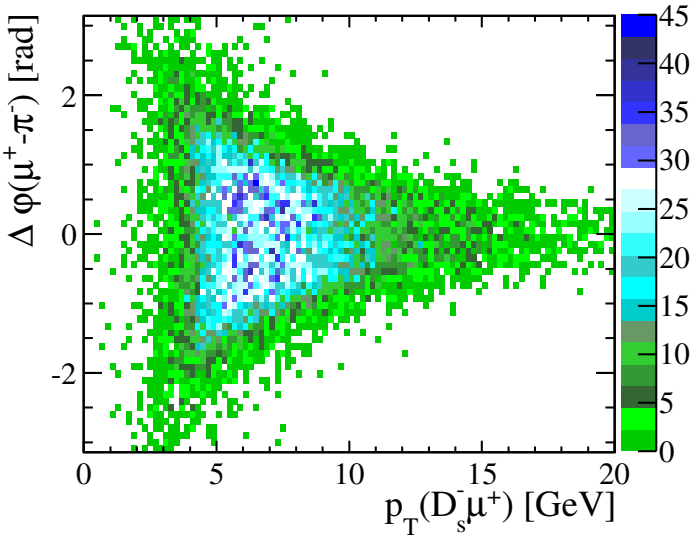

Figure 31: The φ angle correlation between pion track and muon track as a function of B($D_s^- \mu^+$) transverse momentum (only magnet up data for $\mu^+\pi^-$ combination shown here).

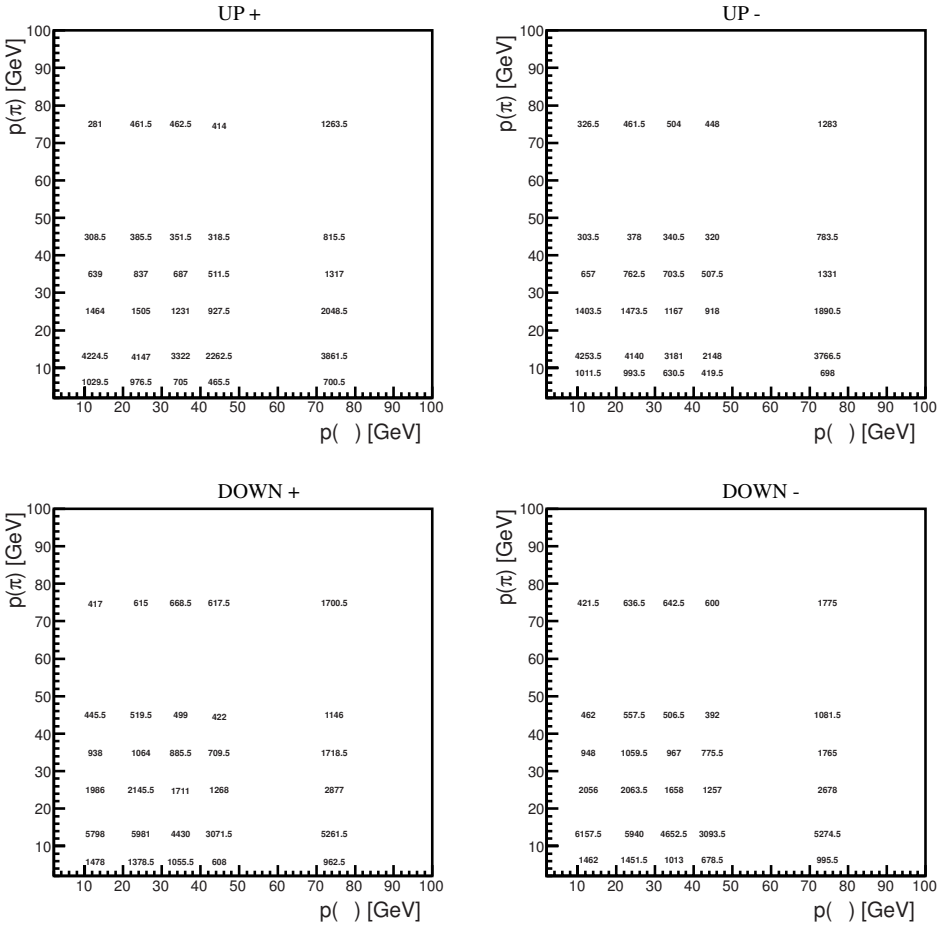

Figure 32: The signal yield, $N_{ij}(D_s^-\mu^+)$ and $N_{ij}(D_s^+\mu^-)$, in each of the 2D correlated bins.

In the second approach, we estimate the correction factor, $A_{\rm track}(\mu^\pm - \pi^\mp)$, by using the tracking efficiency asymmetry, $A_{\rm track} = (\varepsilon({\rm track}^+)/\varepsilon({\rm track}^-) - 1)/2$, and coupling to the difference between momentum distributions of pion and muon [17]

$$A_{\rm track}(\mu^\pm - \pi^\mp) = \int (P_\mu(x) - P_\pi(x)) \times A_{\rm track}(x)\, {\rm d}x. \tag{30}$$

Here $P_\mu(x)$ is the P.D.F for muon momentum spectra while $P_\pi(x)$ is the P.D.F for pion momentum spectra. They are shown in Fig. 33 for a fine binning in magnet up data only and Fig. 34 for a coarse binning where magnet up and down data, $D_s^+\mu^-$ and $D_s^-\mu^+$ final states are combined. The tracking efficiency asymmetry $A_{\rm track}$ used here is determined from the tracking efficiency ratio that is shown in Fig. 28. Two different hypotheses are used to parametrize this curve in Fig. 28, one is a constant parameter while the other one a linear line. The estimated values for the correction factor $A_{\rm track}$ are shown in Table 24.

The second method is slightly more sensitive to correlations, thus we use the first one as our default correction. Note that the uncertainty of 0.13% is very conservative and is

Table 23: Summary table of the tracking efficiencies (in %) in the six momentum intervals, only diagonal elements of the covariance matrix are shown as the errors.

Momentum	UP track$^+$	UP track$^-$	DOWN track$^+$	DOWN track$^-$
$2-6$ GeV	48.68 ± 0.31	49.30 ± 0.31	47.88 ± 0.26	47.95 ± 0.26
$6-20$ GeV	59.11 ± 0.22	59.96 ± 0.22	60.24 ± 0.17	59.85 ± 0.17
$20-30$ GeV	59.07 ± 0.35	59.10 ± 0.34	59.85 ± 0.28	59.95 ± 0.27
$30-40$ GeV	57.17 ± 0.49	56.97 ± 0.47	57.66 ± 0.41	57.65 ± 0.40
$40-50$ GeV	54.89 ± 0.64	54.51 ± 0.62	55.65 ± 0.54	55.76 ± 0.53
$50-100$ GeV	51.52 ± 0.62	51.45 ± 0.61	53.70 ± 0.55	54.80 ± 0.55

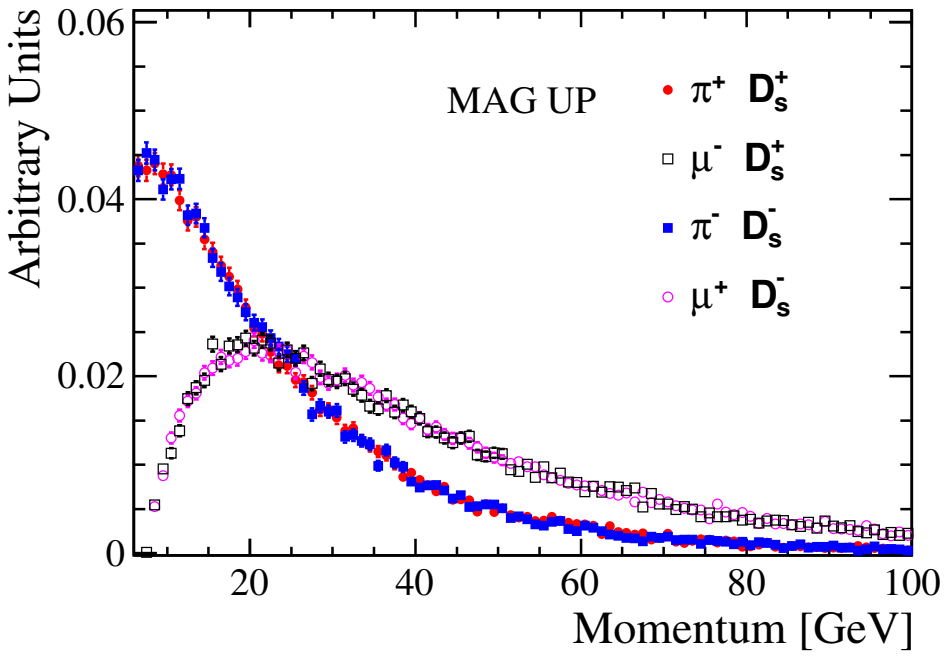

Figure 33: $P_\mu(x)$ is the P.D.F for muon momentum spectra while $P_\pi(x)$ is the P.D.F for pion momentum spectra for magnet up data only.

due only to the limited statistical accuracy of this calibration sample. The central value of the correction obtained with different methods is totally negligible. A small residual sensitivity to K track reconstruction asymmetry is present due to a slight momentum mismatch between the two Ks due to the interference with the S-wave component. Using the second method, we obtain $A^{\rm KK}_{\rm track} = (0.012 \pm 0.004)\%$, thus the total tracking asymmetry is $A_{\rm track} = (0.02 \pm 0.13)\%$.

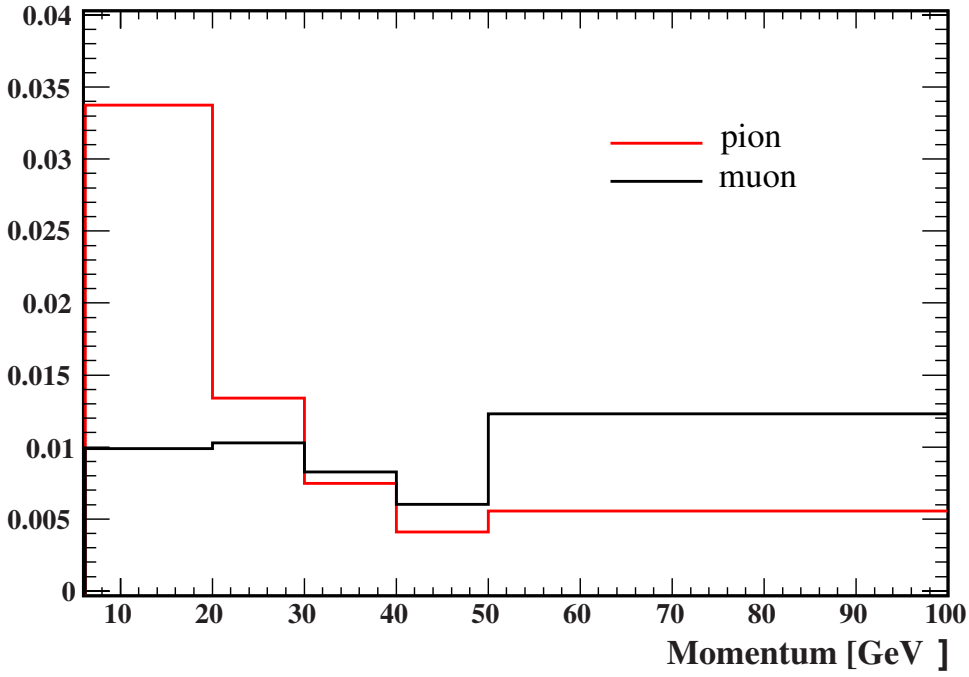

Figure 34: $P_\mu(x)$ for muon momentum spectra is shown in a coarse binning while $P_\pi(x)$ for pion momentum spectra. Here magnet up and down data, $D_s^+\mu^-$ and $D_s^-\mu^+$ final states are combined.

Table 24: Summary table of the correction factor for tracking efficiency asymmetries, $A_{\text{track}}(\mu^\pm - \pi^\mp)$.

Method I	
	$A_{\text{track}}(\mu^\pm - \pi^\mp)$
Measured bin-by-bin tracking efficiencies	(0.01±0.13)%
Method II	
	$A_{\text{track}}(\mu^\pm - \pi^\mp)$
Measured bin-by-bin tracking efficiencies	$(-0.08 \pm 0.19)\%$
Constant fit	0 ± 0
Linear fit	$(-0.0008 \pm 0.17)\%$

9 Background Studies

In order to determine the shape of the prompt background precisely, we have developed a dedicated stripping stream where we utilize the signal selection criteria, except from the muon related ones. The track forming the $D_s^+ h^-$ candidate is required to be within the acceptance of the muon system. This sample has an enhanced prompt population, as the presence of a real muon strongly suppresses the prompt component in the logIP spectrum and thus it makes it easier to derive the parameters of the associated PDF. This sample is split into pion and kaon subsets depending upon whether PID(K-π) is less or greater than 0. Fig. 35 shows the two-dimensional fits to the RS sample of pions and kaons in the whole momentum range studied for magnet down data. The K sample has essentially the same logIP profile. Using the PDF derived in this manner, we have derived the prompt background with the two dimensional fits discussed in the introduction. From the asymmetry in the prompt yield normalized to the overall signal sample in the 5 momentum bins chosen, we obtain an asymmetry due to prompt background equal to +(0.14±0.07)% for magnet up, (-0.05±0.05)% for magnet down, with an average value of (0.04±0.04)%.

We have studied the probabilities that a pion or a kaon are mistaken for a muon if we apply the selection criteria used in our analysis, as well as their charge asymmetry. We perform the study in the five momentum bins chosen for our analysis, using a sample of $D^{*+} \to \pi^+ D^0$, with D^0 decaying into $K^-\pi^+$. Using these samples we determine the momentum dependent fakes rates. We show the results in Fig. 36. Pion induced fakes are even smaller. The net effect from this contribution is below our sensitivity (¡0.01%) and thus can safely be neglected.

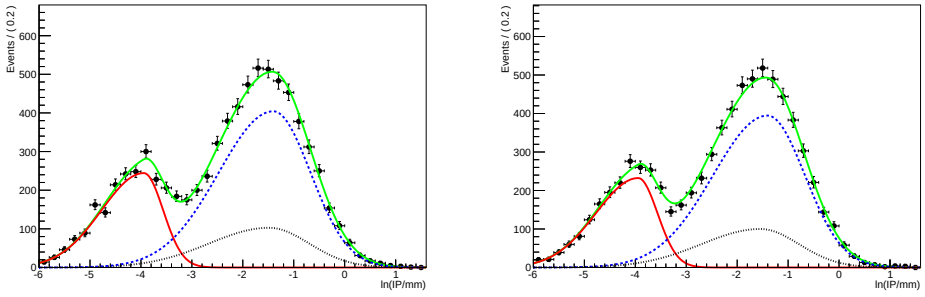

Figure 35: Fit results from two-dimensional fits to the RS $K^+K^-\pi^+$ invariant mass and ln(IP/mm) distribution for magnet up data for pion momentum in the range 6-20 GeV. The blue dotted line shows B_s^0 decays, the red solid line prompt, and the black-dashed line background. (a) and (b) show the spectra for hadrons that are identified as pions, while (c) and (d) show kaons.

We also consider the background induced by combinations of D_s^+ and μ^- events deriving from $b \to c\bar{c}s$ decays where the D_s^+ originates from the upper vertex and the muon

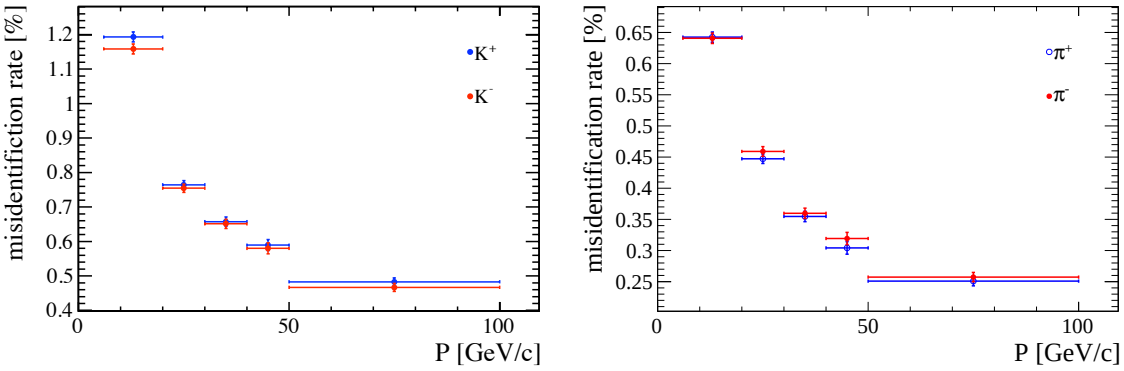

Figure 36: (a) Momentum dependent muon misidentification probabilities for (a) kaons and (b) pions. The open circles represent positive tracks and the filled (red) circles negative tracks.

originates from the charmed meson semileptonic decay, or where the muon and the D_s^+ originate from different b parents. In previous studies of b fractions [11] we found this background to be (5.1±1.7)%. We now use a more refined model, based on the LHCb measurement of the b-hadron production fraction, as well as the measured branching fractions for $B \to D_s^+ DX$ and charm semileptonic decays. In addition, we consider backgrounds coming from $B^0 B^+ \to D_s^- K \mu^+$, that provide a background asymmetry with opposite sign.

The $b \to c\bar{c}s$ background term is estimated using the relationship:

$$A_{bkg} = \frac{-a_p N_{bkg}}{N_{sig}} \tag{31}$$

$$= \frac{-a_p \mathcal{B}(B \to DD_s X)\mathcal{B}(D \to \mu X)}{\mathcal{B}(B_s^0 \to D_s^+ \mu\nu X)} \times \frac{\varepsilon_{bkg}}{\varepsilon_s} \times \frac{f_i}{f_s}, \tag{32}$$

where the relevant branching fractions are shown in Table 25 and D denotes the relevant charm hadron. All the contributions listed in Table 25 are added with this formalism to obtain the total background estimate.

The $B^0(B^+) \to D_s^- K \mu^+$ background is estimated using the relationship:

$$A_{bkg} = \frac{a_p N_{bkg}}{N_{sig}} \tag{33}$$

$$= \frac{a_p \mathcal{B}(B^0 B^+ \to D_s^- K \mu^+)}{\mathcal{B}(B_s^0 \to D_s^+ \mu\nu X)} \times \frac{\varepsilon_{bkg}}{\varepsilon_s} \times \frac{f_i}{f_s}. \tag{34}$$

Table 25 summarizes the $\bar{B} \to D_s^+ DX$ branching fractions assumed, and the ratios between the efficiencies for these backgrounds and the efficiency for the signal $B_s \to D_s \mu\nu$ with dedicated MC samples. We have then used the measured branching fractions for the hadrons to upper charm to derive an estimate of this background fraction and

its potential asymmetry. The $\overline{B}^0$ decays have been split into final states including a $\overline{D}^0$ and a D^- according to the D^{*+}/D^+ ratio in the measured exclusive final states. An uncertainty of 20% has been assigned to this model, by varying this fraction and reevaluating this background component. Taking into account the 46% weight factor for the $\overline{B}^0$ component due to mixing, we obtain an overall background asymmetry equal to (0.01±0.04)%. The systematic error includes the uncertainty in the inclusive branching fraction of the b-hadrons, uncertainties in the b-fractions, and in the charm semileptonic branching fractions., but is dominated by the uncertainty in the production asymmetry. Fig. 37 shows that the ratio $\varepsilon_{bkg}/\varepsilon_s$ as is independent of the muon candidate momentum,

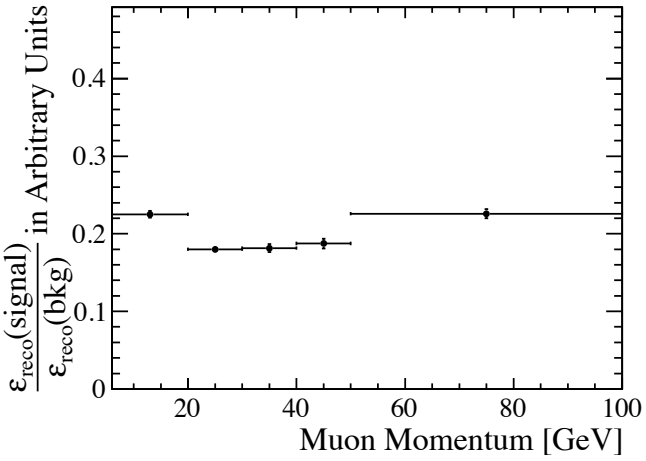

Figure 37: Study of the momentum dependence of the signal to background ratio, for backgrounds produced by $B \to DD_s$ events. The vertical axis is the ratio between reconstructed events in the signal MC sample and in the background MC sample for a given momentum bin.

Table 25: Branching fractions and efficiency ratios for $B \to D_s D$ backgrounds. The b-hadron fractions are defined respectively as f_u/f_s, f_d/f_s, or $f_{\Lambda b}/f_s$, where f_i represents the probability that a b quark hadronizes into the corresponding b-hadron.

Mode	$\mathcal{B}(\%)$	$\varepsilon_s/\varepsilon_{\rm bkg}$	a_p	b-hadron fraction
$B^+ \to D_s^+ X$	(7.9±1.4)	11	(+0.3±0.9)% [18]	3.75±0.29[19]
$B^0 \to D_s^+ D^0 X$	(5.7±1.2)	11	(−0.1±1.0)% [20]	3.75±0.29[19]
$B^0 \to D_s^+ D^- X$	(4.6±1.0)	18	(−0.1±1.0)%[20]	3.75±0.29[19]
$\Lambda_b \to D_s^+ \Lambda_c X$	(10.0±2.0)	14	(−1.0±4.0)% [21]	2.32±0.63[19]
$B^+ \to D_s^- K\mu^+$	$(\ 6.1 \pm 1.2) \times 10^{-2}$	2	(+0.3±0.9)%[22]	3.75±0.29[19]
$B^0 \to D_s^- K\mu^+$	$(\ 6.1 \pm 1.2) \times 10^{-2}$	2	(−0.1±1.0)%[20]	3.75±0.29[19]

Table 26: Branching fractions for the semileptonic branching fractions used in the background estimate. The results are based on Ref. [23]. The B_s^0 and Λ_c semileptonic branching fractions have been derived from the lifetime, assuming equality of Γ_{sl}.

Mode	$\mathcal{B}(\%)$
$B_s^0 \to D_s^- \mu^+ \overline{\nu}_\mu X$	8.9±0.4
$B^0(B^+) \to D_s^{-(\star)} \mu^+ \overline{\nu}_\mu K$	(6.1±1.2)×10^{-2}
$D^0 \to X \mu^+ \nu_\mu$	6.5±0.1
$D^+ \to X \mu^+ \nu_\mu$	16.1±0.3
$\Lambda_c \to X \mu^+ \nu_\mu$	3.1±0.3

Using these data, we obtain an overall asymmetry due to the b-hadron background equal to (0.01±0.04)%.

If we combine the asymmetries due to the three sources of background considered we obtain $A_{bkg} = (0.05 \pm 0.06\%$.

10 Results

We calculate corrected asymmetries A_μ^c in all the kinematic grids described before, and then we derive an average A_μ^c obtained as a weighted average with weights given by the statistical errors in the signal and calibration sample in the two binning schemes chosen for this analysis. We have obtained A_μ^c using muon identification corrections both in the KS and MS sample. Table 27 summarizes the results obtained with MS ad KS corrections with the two different kinematic binning schemes.

The corrected asymmetries in each muon momentum bins, A_μ^c, using different binning strategy and different calibration procedures are shown in Fig. 38 . We have also performed fits splitting the first momentum bin into two equal sized bins; the results are shown in Fig. 39, suggesting that the lower value observed in the first bin is the result of a statistical fluctuation.

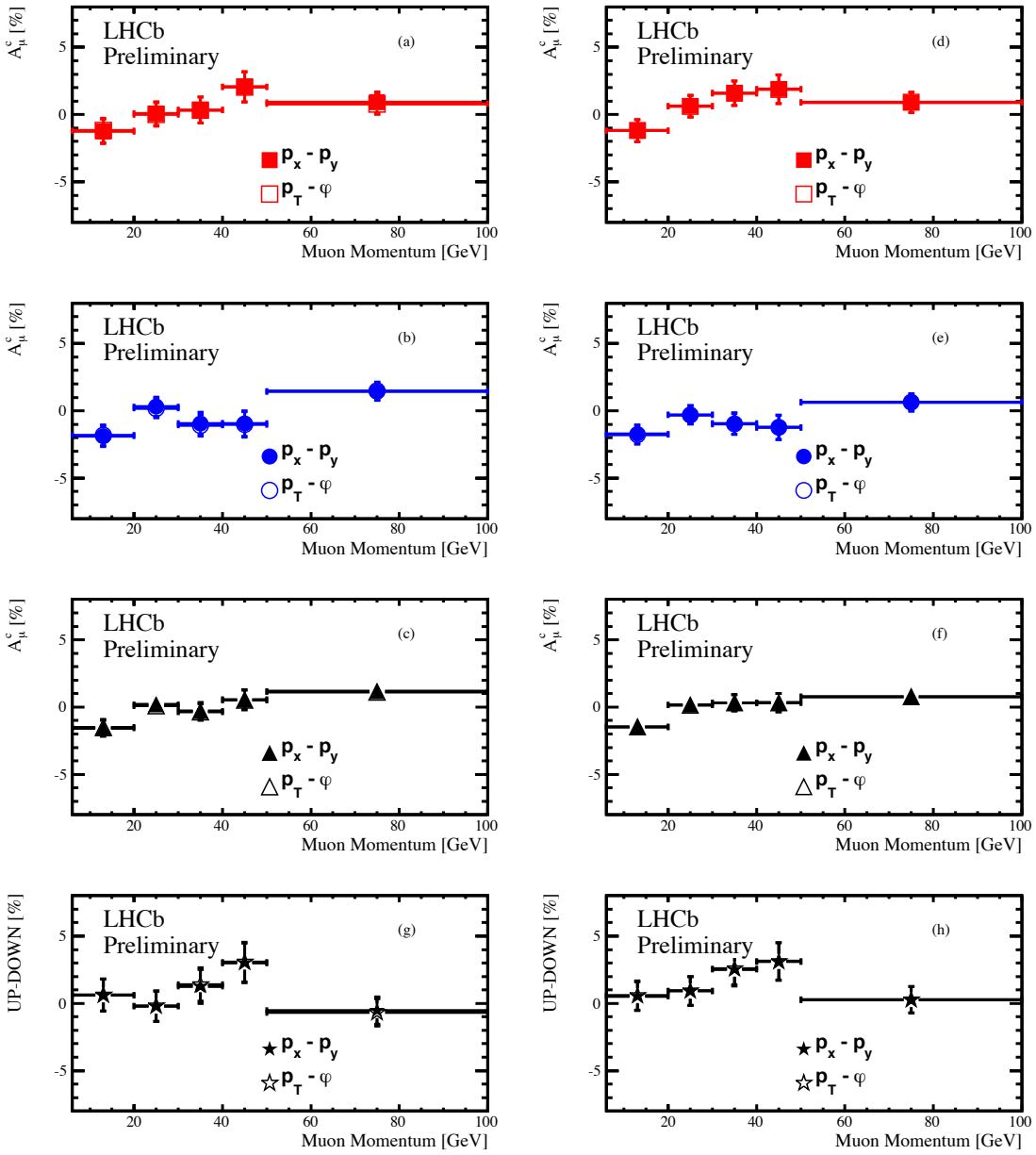

Figure 38: The muon efficiency ratio corrected asymmetries, A_μ^c, is examined in the five muon momentum intervals for: (a) magnet up data (b) magnet down data and (c) average using the KS muon calibration method in the two different binning scheme, (d) magnet up data (e) magnet down data and (f) average using the MS muon calibration method in the two different binning scheme. The χ^2 for a fit to a constant is 12.0 for the KS calibration method and 10.8 for the MS calibration method, both with 4 degrees of freedom. The corresponding probabilities of fits to a constant function are 1.7% and 2.9%. The differences in asymmetry between magnet up and magnet down data are shown in (g) for the KS and (h) for the MS calibration scheme respectively.

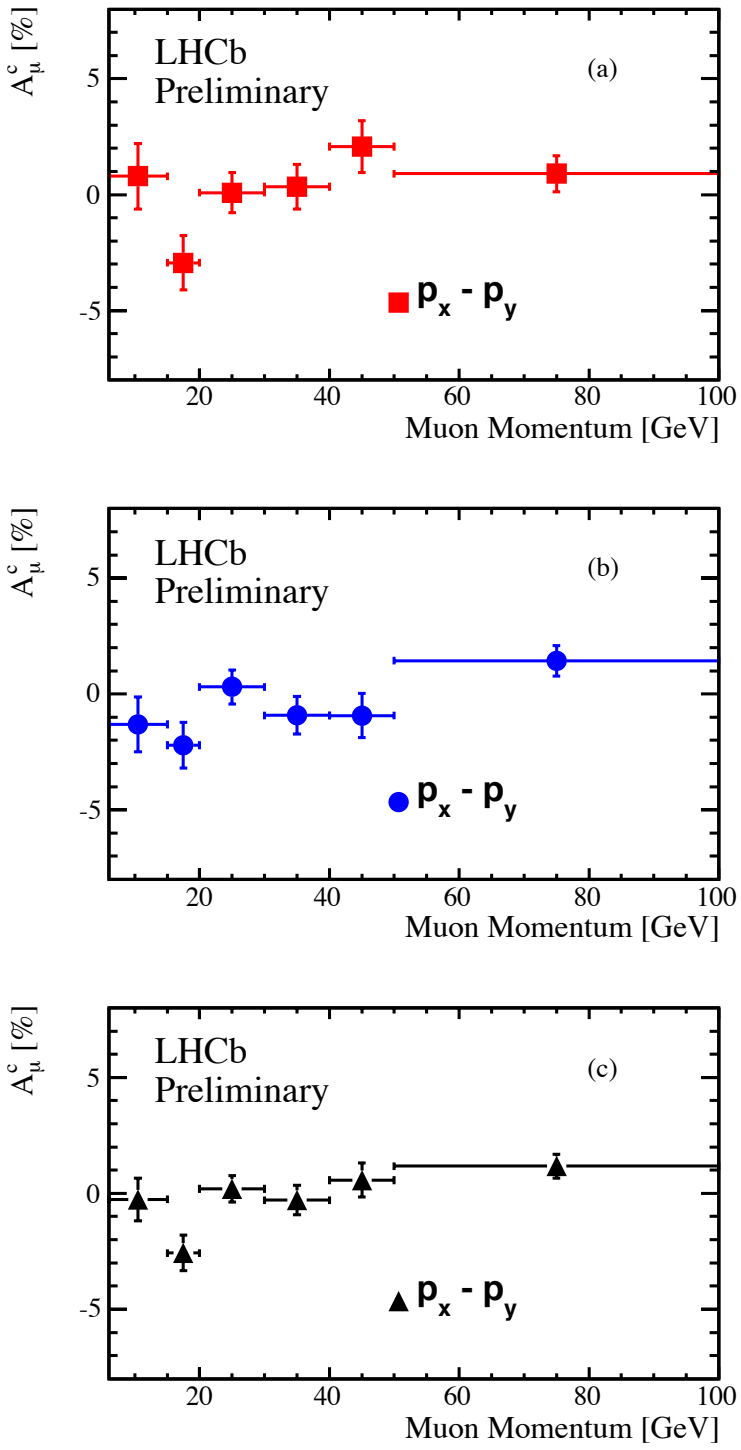

Figure 39: Corrected A_μ^c as a function of muon momentum: (a) magnet up, (b) magnet down, and (c) average in 6 bins of muon momentum. The χ^2 for a fit to a constant is 13.3 with five degrees of freedom, corresponding to a probability of 2.1%.

The results obtained without using the LUT correction in the MS sample are shown in Figure 40. The corresponding plot for the KS correction approach is shown in Fig. 41. For each binning scheme, muon correction method, and magnet polarity, the sub-bin measurements are statistically compatible with the weighted mean.

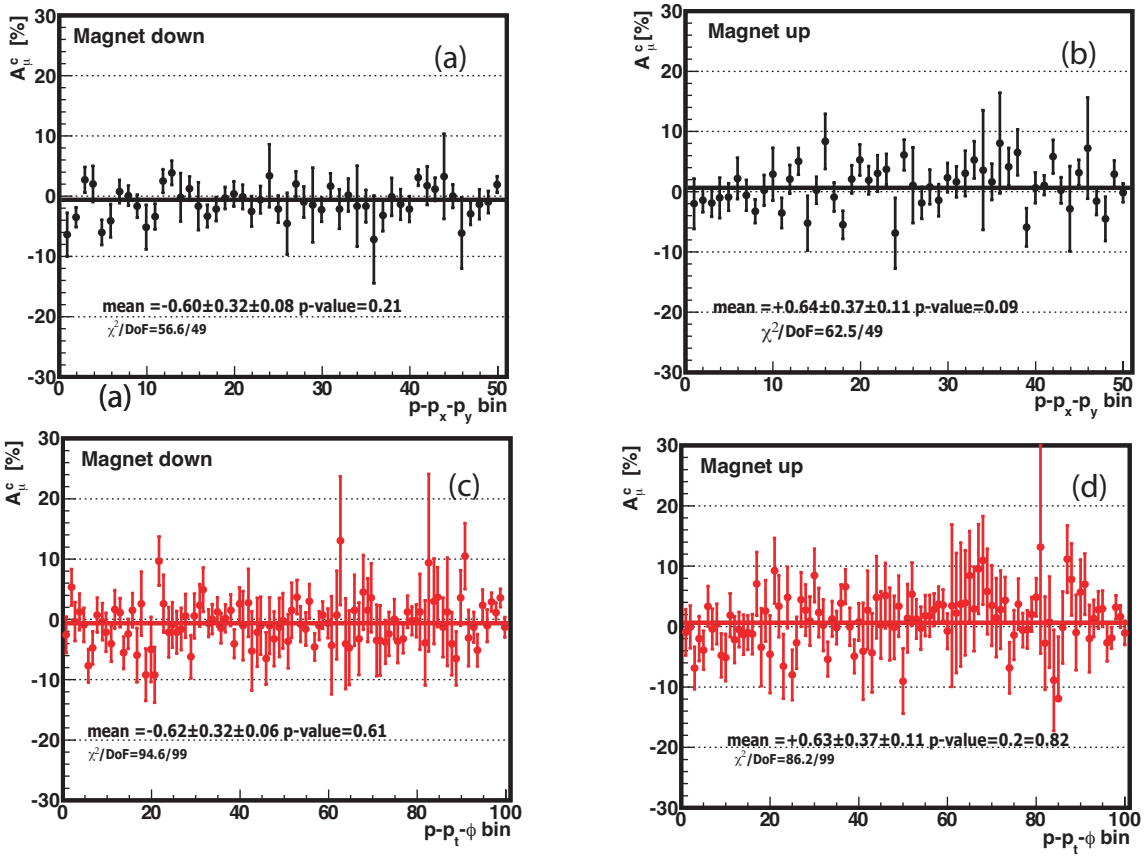

Figure 40: The muon efficiency ratio corrected asymmetries, A_μ^c, in each sub-bin of the p, p_x, p_y binning scheme is shown for **a)** magnet down and **b)** magnet up polarity data. These data utilize the MS calibration sample for muon correction. The $p_t\phi$ binning scheme results are shown for **c)** magnet down and **d)** magnet up polarity data. A horizontal fit (the weighted average) to the sub-bins is shown by the solid lines. The quality-of-fit parameters and fitted results are displayed on each figure.

In order to obtain the final results, we perform an arithmetic average of the four values of A_μ^c obtained with the two binning schemes chosen and with the two muon correction methods, assuming the results fully statistically correlated, and we obtain $A_\mu^c = +0.04 \pm 0.25$. We then correct for tracking efficiency asymmetries and background asymmetries, and we obtain

$$A_{\text{meas}} = (-0.03 \pm 0.25 \pm 0.18)\% \tag{35}$$

where the first error reflects statistical uncertainties in the signal extraction and the second

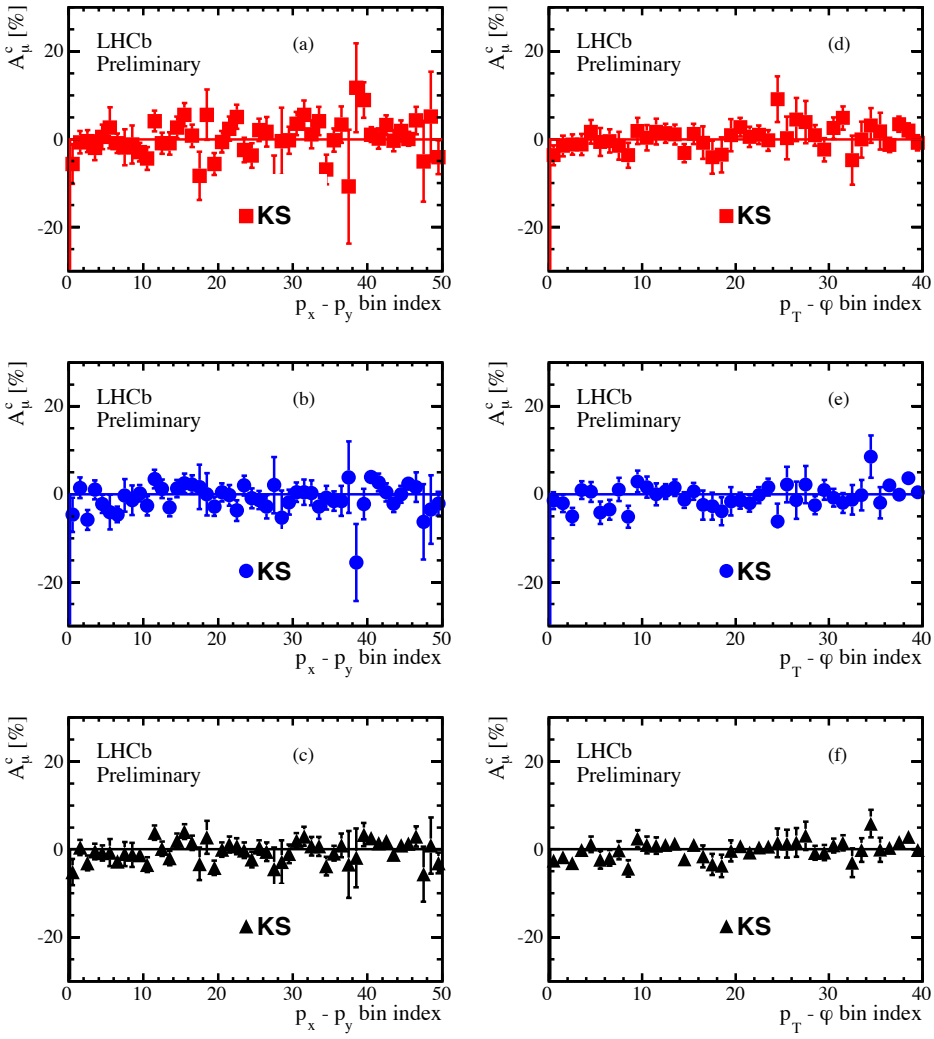

Figure 41: The muon efficiency ratio corrected asymmetry, A_μ^c, for (a) magnet up (b) magnet down data and (c) average in the 50 $p_x - p_y$ bins, (d) magnet up (e) magnet down data and (f) average in the 40 $p_T - \varphi$ bins, when using muon efficiency ratio corrections from the KS J/ψ sample.

error reflects the systematic uncertainties summarized in Table 28. This implies

$$a_{sl}^s = (-0.06 \pm 0.50 \pm 0.36)\%. \tag{36}$$

Table 27: Muon efficiency ratio corrected asymmetry A_μ^c with yields and corrections determined before the L0 fix, the errors account for the statistical uncertainties in the B_s^0 signal yields and in the muon efficiencies ($\pm B_s^0$ stat. $\pm$ J/ψ stat.).

A_μ^c [%]	KS muon correction		MS muon correction		Average
	pp_xp_y	$pp_t\phi$	pp_xp_y	$pp_t\phi$	
Magnet Up	$+0.38 \pm 0.41$	$+0.30 \pm 0.41$	$+0.64 \pm 0.38$	$+0.63 \pm 0.38$	$+0.49 \pm 0.38$
Magnet Down	-0.17 ± 0.34	-0.25 ± 0.34	-0.60 ± 0.38	-0.62 ± 0.32	-0.41 ± 0.32
Average	$+0.11 \pm 0.27$	$+0.02 \pm 0.27$	$+0.02 \pm 0.25$	$+0.01 \pm 0.25$	$+0.04 \pm 0.25$

11 Systematic uncertainties

We consider several sources of systematic uncertainties that are summarized in Table 28.

We study the effect of the fitting procedure, by comparing results obtained with different models. The signal is fitted with 2 Gaussians PDF, either independent or equal for the two muon charges. We have also determined the yields with the counting method, where we fit for a smooth background, and determine the yields in a mass window centered around the PDG value of the D_s^+ mass and $\pm$ 50 MeV wide. We have also used 1st or 2nd order Chebychev functions to model the background. In addition, we use two different approaches to correct for muon efficiency. By examining the variations on the average A_μ^c obtained with different procedures, we assign a (0.07%) uncertainty to this quantity. This uncertainty includes three almost equal components, accounting for fitting procedure, kinematic binning and residual systematic uncertainty related to muon efficiency ratio calculation. In addition, we consider the effects of the statistical uncertainties the efficiency ratios (0.08%), accounted for by propagating these errors in the weighted averages performed to derive A_μ^c.

The uncertainties associated with $A_{\rm track}$ has been discussed in Section 8. The uncertainty in $A_{\rm track}$ is dominated by the statistical accuracy of this sample, and the consequent uncertainty in the momentum dependence of the pion detection charge asymmetry.

The uncertainty in $A_{\rm bkg}$ has been discussed in Section 9. This quantity includes three terms, evaluated separately. The first component is in the prompt background asymmetry, driven by the uncertainty in the prompt background yield estimate returned by the fit algorithm. The second one is the term related to backgrounds coming from $D_s - h$ combinations, where h represents a generic hadron mistaken for a muon. Once we include the very small probability for a kaon and pion to be incorrectly identified as a muon, this term can be neglected. Lastly there is the b-hadron background component, that is dominated by the uncertainties in the measured production asymmetries.

Varying run conditions makes the field-up and field-down datasets not fully compatible and the cancellation may not be perfect. We first take the difference between the up and down $A_{\rm meas}$ and then multiply it by a scale factor that we obtain by comparing the up and down signal yields with luminosity difference between the two samples. This follows the method discussed in [13], and the uncertainty obtained is 0.01%.

The systematic uncertainty associated with the HLT2 bias in muon topological trigger is obtained by taking the statistical error in the assessment of this quantity, weighted by a factor of 0.5, roughly correspondent to the fraction of the number of events triggered solely by this algorithm.

Table 28: List of sources of systematic uncertainty

Sources	$\sigma(A_{\text{meas}})[\%]$
Signal modeling and muon correction	0.07
Statistical uncertainty on the efficiency ratios	0.08
Background subtraction	0.05
Asymmetry in track reconstruction	0.13
Varying run conditions between field-up and field-down	0.01
HLT2 bias in muon topological trigger	0.05
Total	0.18

12 Systematic checks

In order to establish the robustness of our results, we study different kinematic dependencies in $A_{\rm Raw}$. The first concern is the stability of performance of the detector in different run periods, important for the cancellation of biases in the magnet up and magnet down samples. Thus, we examine the raw signal asymmetries, $A_{\rm Raw} = \frac{n(D_s^- \mu^+) - n(D_s^+ \mu^-)}{n(D_s^- \mu^+) + n(D_s^+ \mu^-)}$, in different run periods for magnet up and down data separately using all triggered events as shown in Fig. 43, the ten different run blocks are highlighted in Fig. 42 by the vertical black dashed lines. In addition, we study the sensitivity of $A_{\rm Raw}$ to the muon $p_{\rm T}$, and to number of long tracks per event. The results are shown in Figs. 45, 44. Finally, we study the dependencies upon the B_s^0 kinematics (η and $p_{\rm T}$), to make sure that there is no anomalous region of the b-hadron phase space where the corrections discussed before have a larger effect. No kinematic dependence is found, as shown in Figs. 46 and 47 . All these studies are consistent with a very stable behavior of the data analyzed.

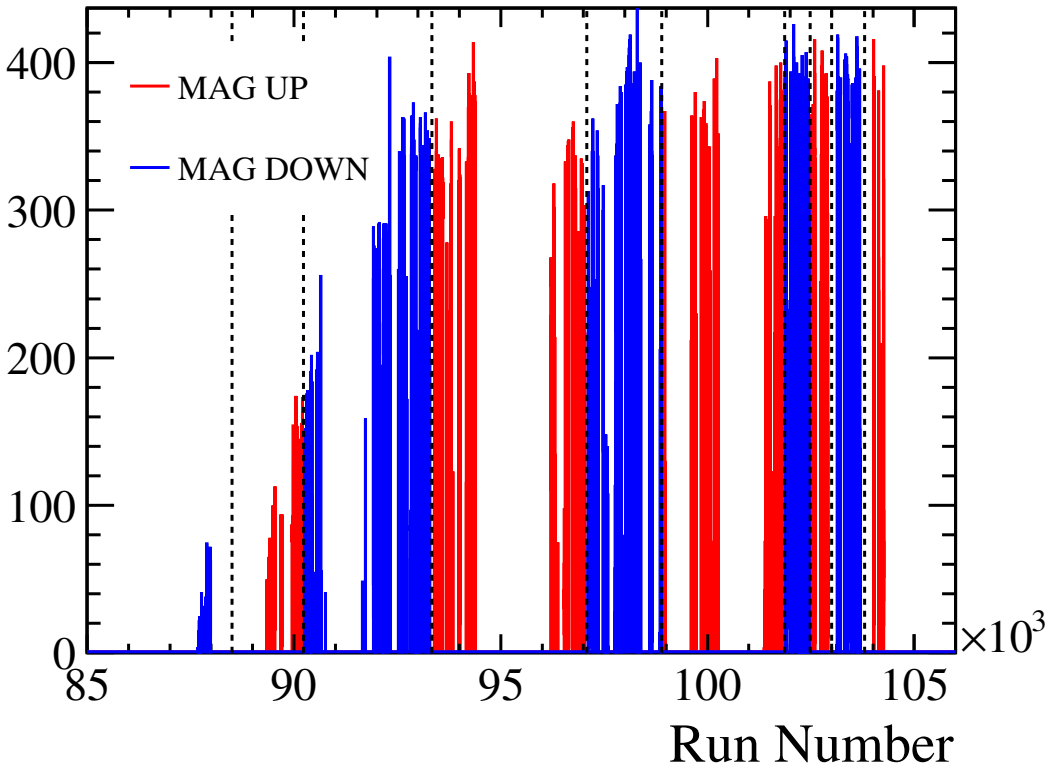

Figure 42: The ten run blocks that are used to check the stability of the asymmetry, the magnet field changes polarity between different run blocks.

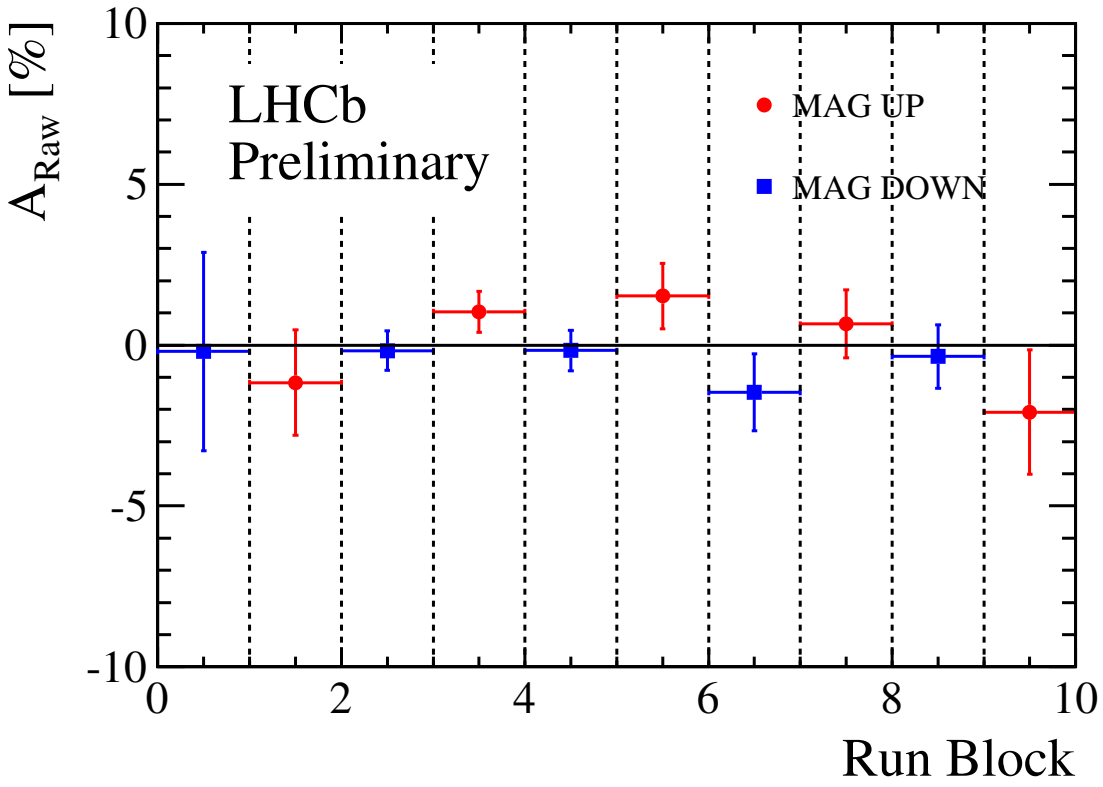

Figure 43: The raw B_s^0 signal asymmetry, $A_{\rm Raw} = \frac{n(D_s^-\mu^+) - n(D_s^+\mu^-)}{n(D_s^-\mu^+) + n(D_s^+\mu^-)}$, in the ten run blocks.

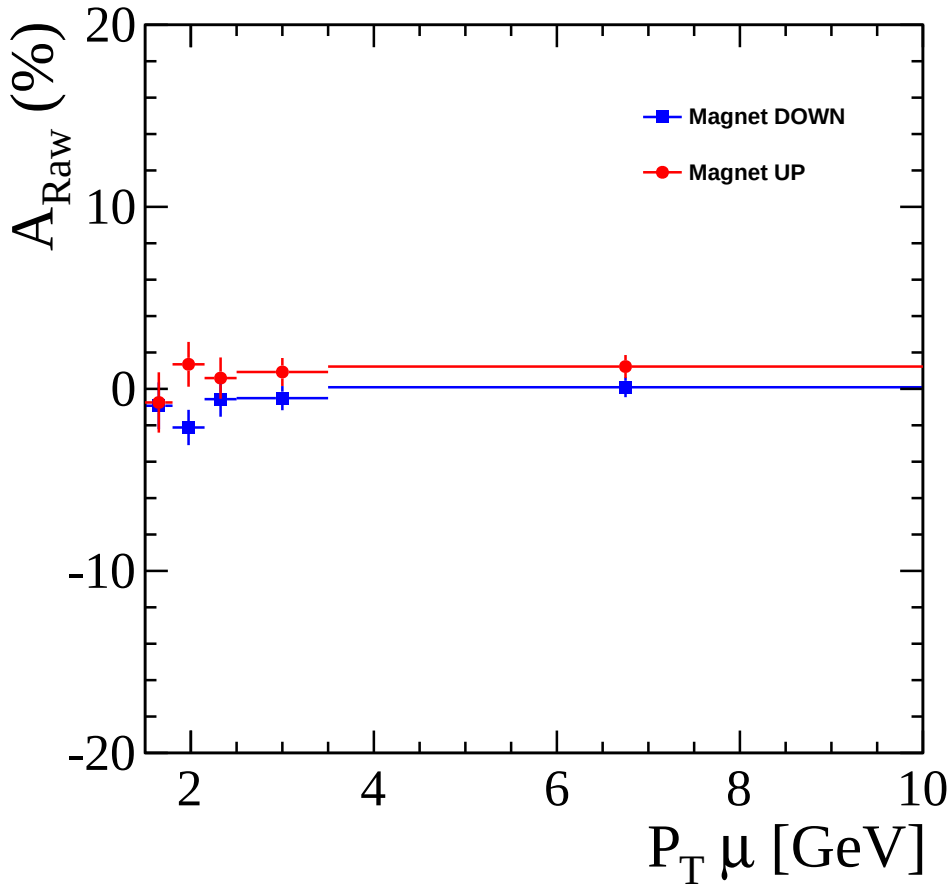

Figure 44: The raw B_s^0 signal asymmetry, $A_{\rm Raw} = \frac{n(D_s^-\mu^+) - n(D_s^+\mu^-)}{n(D_s^-\mu^+) + n(D_s^+\mu^-)}$ is shown as a function of μ $p_{\rm T}$ for $\phi\pi$ events that are triggered by a logical OR of Muon Topological lines and Incl Phi lines for magnet up and down data separately. This plot is generated after reprocessing the data with the L0 correction discussed in the text.

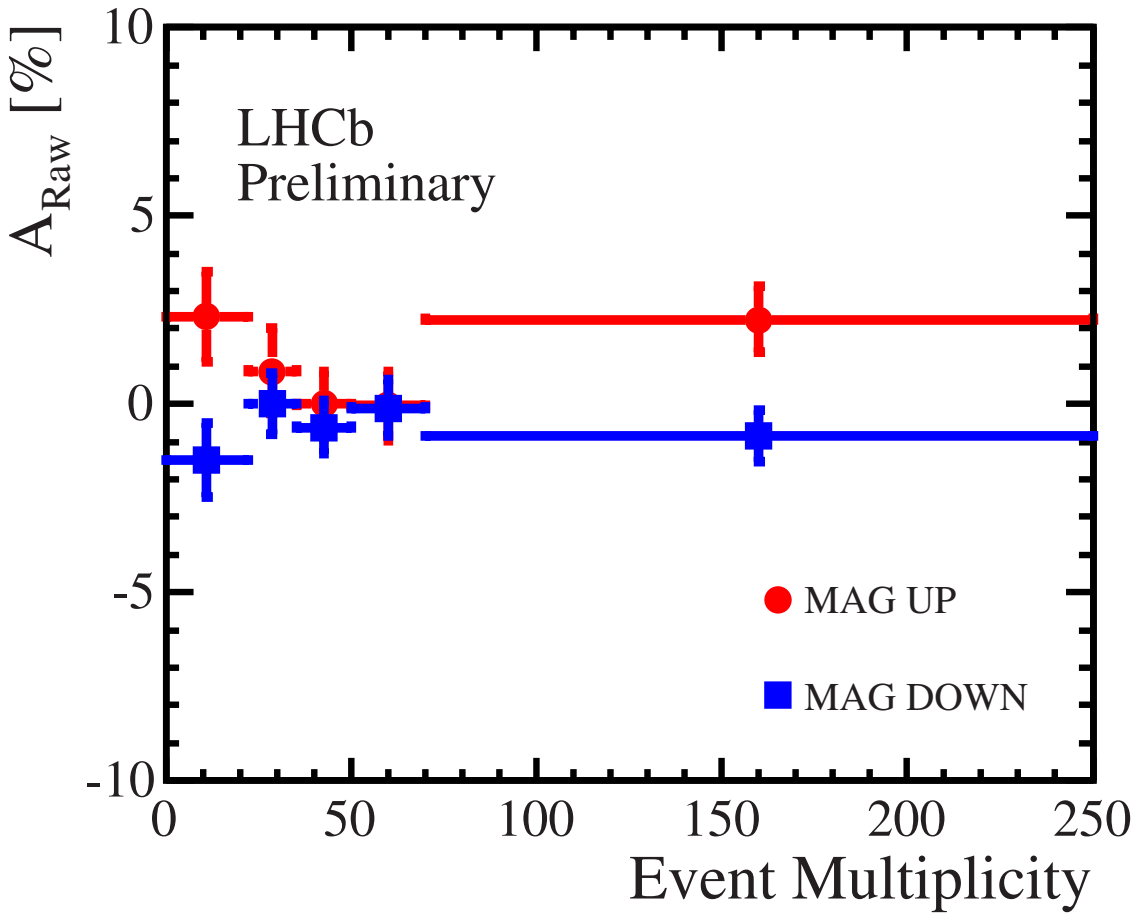

Figure 45: The raw B_s^0 signal asymmetry, $A_{\rm Raw} = \frac{n(D_s^-\mu^+)-n(D_s^+\mu^-)}{n(D_s^-\mu^+)+n(D_s^+\mu^-)}$ is shown as a function of event multiplicity for magnet up and down data separately.

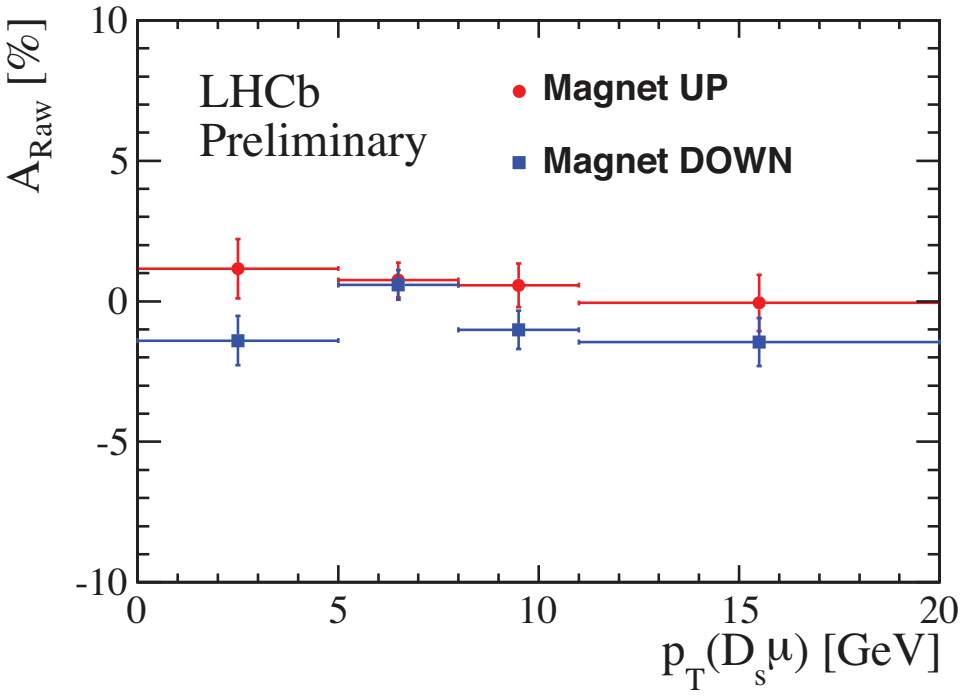

Figure 46: The raw B_s^0 signal asymmetry, $A_{\rm Raw} = \frac{n(D_s^- \mu^+) - n(D_s^+ \mu^-)}{n(D_s^- \mu^+) + n(D_s^+ \mu^-)}$ is shown as a function of B_s^0 $p_{\rm T}$ for $\phi\pi$ events that are triggered by a logical OR of Muon Topological lines and Incl Phi lines for magnet up and down data separately.

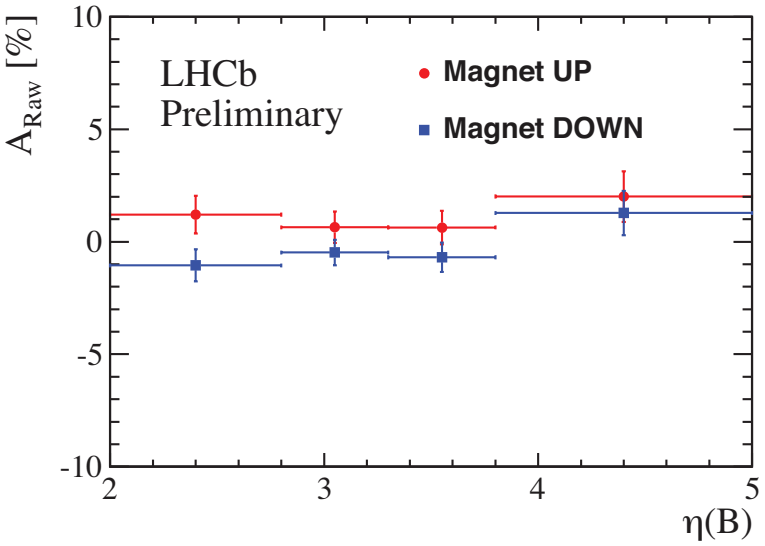

Figure 47: The raw B_s^0 signal asymmetry, $A_{\rm Raw} = \frac{n(D_s^- \mu^+) - n(D_s^+ \mu^-)}{n(D_s^- \mu^+) + n(D_s^+ \mu^-)}$ is shown as a function of B_s^0 pseudorapidity for $\phi\pi$ events that are triggered by a logical OR of Muon Topological lines and Incl Phi lines for magnet up and down data separately.

13 Discussion

The predictions in the Standard Model for semileptonic asymmetries in $\overline{B}^0_s$ and $\overline{B}^0$ decays are $a^s_{\rm sl} = (1.9 \pm 0.3) \times 10^{-5}$, and $a^d_{\rm sl} = (-4.1 \pm 0.6) \times 10^{-4}$ [4]. Our measurement is consistent with the SM prediction.

The D0 collaboration has measured an asymmetry in dimuon decays in 1.96 TeV $p\overline{p}$ collisions of $A^b_{\rm sl} = (-0.787 \pm 0.172 \pm 0.093)\%$ [5]. They consider the measured asymmetry to be related to the semileptonic asymmetries in $\overline{B}^0$ and $\overline{B}^0_s$ decays as $A^b_{\rm sl} = (0.594 \pm 0.022) a^d_{\rm sl} + (0.406 \pm 0.022) a^s_{\rm sl}$, based on the production and lifetime ratios. D0 has also recently measured the individual values of $a^d_{\rm sl} = (0.68 \pm 0.45 \pm 0.14)\%$ [24], and $a^s_{\rm sl} = (-1.12 \pm 0.74 \pm 0.17)\%$ [25]. We show in Fig. 48 our measurement, the D0 results quoted above and the most recent average from b-factories [6], namely $a^d_{\rm sl} = (0.02 \pm 0.31)\%$.

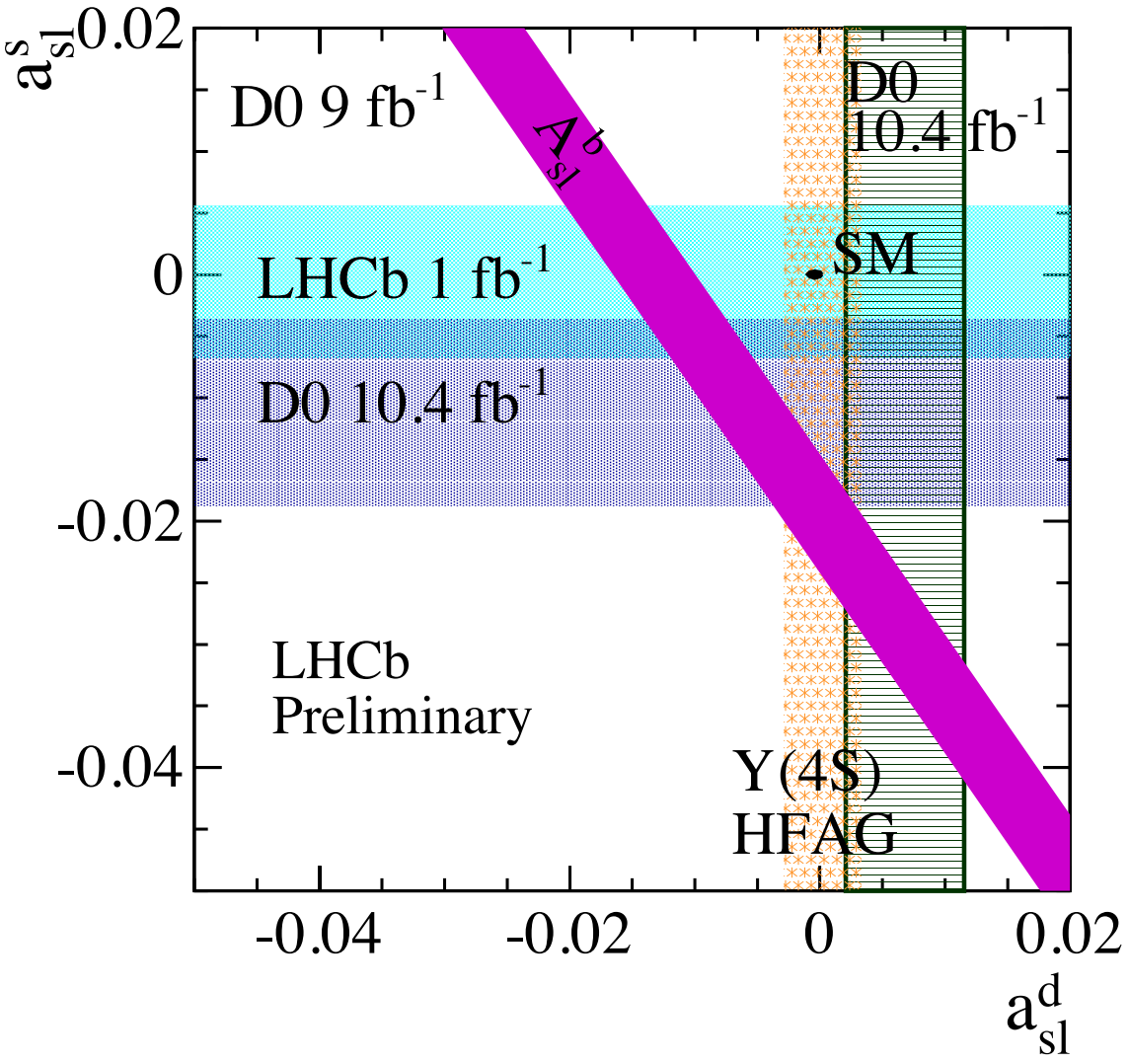

Figure 48: Measurements of semileptonic decay asymmetries. The bands correspond to the central values ± 1 standard deviation, defined as the sum in quadrature of the statistical and systematic errors.

References

[1] U. Nierste, *Three lectures on meson mixing and CKM phenomenology*, arXiv:0904.1869.

[2] A. Lenz and U. Nierste, *Theoretical update of $B_s^0 - \overline{B}_s^0$ mixing*, JHEP **0706** (2007) 072, arXiv:hep-ph/0612167.

[3] C. Bobeth and U. Haisch, *New physics in Γ_{12}^s: $(\bar{s}b)$ $(\bar{\tau}\tau)$ operators*, arXiv:1109.1826.

[4] A. Lenz, *Theoretical update of B-mixing and lifetimes*, arXiv:1205.1444.

[5] D0 collaboration, V. M. Abazov *et al.*, *Measurement of the anomalous like-sign dimuon charge asymmetry with 9 fb^{-1} of $p\overline{p}$ collisions*, Phys. Rev. **D84** (2011) 052007, arXiv:1106.6308; D0 collaboration, V. M. Abazov *et al.*, *Evidence for an anomalous like-sign dimuon charge asymmetry*, Phys. Rev. **D82** (2010) 032001, arXiv:1005.2757; D0 collaboration, V. M. Abazov *et al.*, *Evidence for an anomalous like-sign dimuon charge asymmetry*, Phys. Rev. Lett. **105** (2010) 081801, arXiv:1007.0395.

[6] Heavy Flavor Averaging Group, D. Asner *et al.*, *Averages of b-hadron, c-hadron, and τ-lepton properties*, arXiv:1010.1589, online updates available at http://www.slac.stanford.edu/xorg/hfag/ ; BABAR collaboration, B. Aubert *et al.*, *Search for T, CP and CPT violation in $B^0 - \overline{B}^0$ mixing with inclusive dilepton events*, Phys. Rev. Lett. **96** (2006) 251802, arXiv:hep-ex/0603053; BABAR collaboration, B. Aubert *et al.*, *A measurement of CP-violation parameters in $B^0 - \overline{B}^0$ mixing using partially reconstructed $D^{*-}\ell^+\nu_\ell$ events at BaBar*, arXiv:hep-ex/0607091, submitted to ICHEP 2006; Belle collaboration, E. Nakano *et al.*, *Charge asymmetry of same-sign dileptons in $B^0 - \overline{B}^0$ mixing*, Phys. Rev. **D73** (2006) 112002, arXiv:hep-ex/0505017.

[7] LHCb collaboration, A. Carbone *et al.*, *Measurement of direct CP violation in charmless charged two-body B decays at LHCb using 2010 data*, LHCb-ANA-2012-001.

[8] E. Norrbin and R. Vogt, *Bottom production asymmetries at the LHC*, arXiv:hep-ph/0003056, in proceedings of the CERN 1999 Workshop on SM physics (and more) at the LHC.

[9] LHCb collaboration, R. Aaij *et al.*, *Charmless charged two-body B decays at LHCb with 2011 data*, LHCb-CONF-2011-042.

[10] LHCb collaboration, V. Gligorov, C. Thomas, and M. Williams, *The HLT inclusive B trigger*, LHCb-PUB-2011-016. Public LHCb Note.

[11] LHCb collaboration, M. Artuso *et al.*, *Measurement of b-hadron production fractions in 7 TeV centre-of-mass energy pp collisions*, LHCb-ANA-2011-065.

[12] LHCb collaboration, C. Adrover *et al.*, *Search for the rare decays $B_s^0 \to \mu^+\mu^-$ and $B^0 \to \mu^+\mu^-$ with 1.02 fb^{-1}*, LHCb-ANA-2011-023.

[13] LHCb Collaboration, R. Aaij *et al.*, *Measurement of the Ds+ - Ds- production asymmetry in 7 TeV pp collisions*, Phys. Lett. **B713** (2012) 186, arXiv:1205.0897.

[14] LHCb collaboration, M. Artuso, A. Borgia, S. Stone, Z. Xing, and L. Zhang, *Measurement of the $D_s^+ - D_s^-$ Production Asymmetry* , LHCb-ANA-2012-011.

[15] LHCb collaboration, A. Alves Jr. *et al.*, *The LHCb detector at the LHC*, JINST **3** (2008) S08005.

[16] LHCb Collaboration, R. Aaij *et al.*, *Measurement of the D+/- production asymmetry in 7 TeV pp collisions*, Phys. Lett. **B718** (2013) 902, arXiv:1210.4112.

[17] Belle Collaboration, M. Staric *et al.*, *Search for CP Violation in $D^\pm$ Meson Decays to $\phi\pi^\pm$*, Phys. Rev. Lett. **108** (2012) 071801, arXiv:1110.0694.

[18] LHCb Collaboration, R. Aaij *et al.*, *Measurements of the branching fractions and CP asymmetries of B+ to J/psi pi+ and B+ to psi(2S) pi+ decays*, Phys. Rev. **D85** (2012) 091105, arXiv:1203.3592.

[19] LHCb Collaboration, R. Aaij *et al.*, *Measurement of b-hadron production fractions in* 7 TeVpp *collisions*, Phys. Rev. **D85** (2012) 032008, arXiv:1111.2357.

[20] LHCb collaboration, R. Aaij *et al.*, *First observation of CP violation in the decays of bottom strange mesons*, arXiv:1304.6173.

[21] CMS collaboration, S. Chatrchyan *et al.*, *Measurement of the Λ_b cross-section and the $\overline{\Lambda}_b$ to Λ_b ratio with $\Lambda_b \to J/\psi\Lambda$ decays in pp collisions at $\sqrt{s} = 7$ TeV*, arXiv:1205.0594.

[22] LHCb collaboration, R. Aaij *et al.*, *Measurements of the branching fractions and CP asymmetries of $B^+ \to J/\psi\pi^+$ and $B^+ \to \psi(2S)\pi^+$ decays*, Phys. Rev. **D85** (2012) 091105, arXiv:1203.3592.

[23] Particle Data Group, K. Nakamura *et al.*, *Review of particle physics*, J. Phys. **G37** (2010) 075021.

[24] D0 Collaboration, V. M. Abazov *et al.*, *Measurement of the semileptonic charge asymmetry in B^0 meson mixing with the D0 detector*, Phys. Rev. **D86** (2012) 072009, arXiv:1208.5813.

[25] D0 Collaboration, V. Abazov *et al.*, *Measurement of the semileptonic charge asymmetry using $B_s^0 \to D_s\mu X$ decays*, Phys. Rev. Lett. **110** (2013) 011801, arXiv:1207.1769.

Appendix A: Changes with respect to LHCb-ANA-2012-054

This appendix has the purpose of summarizing the changes that occurred with respect to the previous iteration of this study, that lead to the result

$$a^s_{sl} = (-0.24 \pm 0.54 \pm 0.33)\%. \tag{37}$$

The new result is:

$$a^s_{sl} = (-0.06 \pm 0.50 \pm 0.36)\%. \tag{38}$$

While these results are very consistent, the shift in central value is due to a few changes that improve the treatment of a few small effects. Here is a small list of the changes introduced:

- In deriving the raw yields from in the various kinematic bins, we adjust the bin size to eliminate bins that had no statistics, and we project the yields of the positive and negative charges in the variable $|q|p_x$ or we apply the equivalent reflection for $pp_t\phi$binnining scheme, to have the same profile of the track distribution on the various sensing planes. This is motivated by the goal of eliminating bins where one charge species had a very small yield and the other a very large one. The fitting procedure is also better constrained by selecting an improved initial set of trial parameters derived from the fits in the two dimensional parameter space.

- The muon correction is developed with the same level of precision with the MS calibration and with the KS calibration. It is interesting to note that both calibration schemes now give very consistent results. Note that the addition of the MS calibration sample reduces the statistical uncertainty in the efficiency ratios (now 0.08). because of its higher statistics.

- In the previous analysis we processed separately two HLT2 trigger schemes (ϕ candidate satisfying the inclusive ϕ HLT2 trigger algorithm, and muon selected events, where the signal muon satisfies one of the muon topological HLT2 trigger algorithms and the ϕ is not selected by inclusive *phi* HLT2 trigger algorithm. The study of these two statistically independent sample demonstrated that within error we could not identify any HLT2 related charge asymmetry, a conclusion corroborated by the HLT2 studies reported in section 7. We now process candidate where either the muon satisfies the HLT2 trigger selection or the candidate ϕ satisfies the inclusive ϕ HLT2 trigger selection.

- The central value of $A_{\rm meas}$ in the summer analysis is only corrected for muon-dependent asymmetries. The value quoted in the conference note is determined from the pp_xp_ybinning scheme with all the corrections derived from the KS calibration sample. With the nomenclature adopted in the current note, this is A^c_μ and was determined as $A^c_\mu = -0.12 \pm 0.27$ to be compared with $A^c_\mu = 0.11 \pm 0.27$ for the same

condition. The average between the three different determinations of A_μ^c reported in LHCb-ANA-2012-054 summarized in Table 24, p. 58, gives $A_\mu^c = -0.05 \pm 0.27$.

- We now derive $A_{\rm meas}$ from A_μ^c by correcting also for tracking induced asymmetries, $A_{track} = 0.02 \pm 0.13$, (this is discussed in Section 8), and all the backgrounds sources, prompt charm, D_s^+-false μ pairs, b-hadron background, $A_{bkg} = 0.04 \pm 0.04$)) (details are given in Section 9). The value of A_{bkg} has changed slightly from 0.04 ± 0.04 to 0.05 ± 0.06 because the values of the production asymmetries used have been updated to the most recent experimental results.

- We now derive the final results by an arithmetic average of the 2 binning schemes and 2 calibration schemes. Each of them is very consistent with the average and very small.

- Some of the systematic errors are evaluated more conservatively. The dominant one is the uncertainty in the momentum dependence of the tracking efficiency ratio, dominated by the statistical uncertainty in the calibration sample used.